DEEP LEVEL CHARACTERIZATION OF SEEDED PHYSICAL VAPOR TRANSPORT ZINC SELENIDE

By

BRIAN GERARD MARKEY

Bachelor of Science

Southwest Missouri State University

Springfield, Missouri

1988

Submitted to the Faculty of the
Graduate College of the
Oklahoma State University
in partial fulfillment of
the requirements for
the Degree of
DOCTOR OF PHILOSOPHY
July, 1993

DEEP LEVEL CHARACTERIZATION OF SEEDED
PHYSICAL VAPOR TRANSPORT
ZINC SELENIDE

Thesis Approved:

Thesis Adviser

Dean of the Graduate College

ACKNOWLEDGMENTS

I would first like to thank my advisor, Dr. Steve McKeever. His patience and understanding is more appreciated than I think he realizes. When I felt that I was at a dead end he could always find a new direction, and provide me with the encouragement and motivation to continue. Through our many conversations about both the experimental and theoretical aspects of our work he has shared with me a wealth of experience and insight for which I will always be thankful.

I would also like to express my thanks to the other faculty members who have been kind enough to serve on my committee; Dr. Joel Martin, Dr. Bruce Ackerson, Dr. Jim Wicksted and Dr. Edward Knobbe.

An additional thanks is due Dr. Martin for providing me with the means for evaporating gold electrodes onto the samples used in this project. I am also grateful to Dr. Martin for the many supplies and various equipment he has allowed me to beg borrow and otherwise acquire during the last few years.

When I began working for Dr. McKeever I knew little about the experimental and theoretical problems which lie ahead. I did have, however, the good fortune of spending many months working side by side with Tony Lewandowski. Tony taught me a great deal about experimental procedures and data analysis. We have had many lengthy discussions through which Tony has shared with me his unique insight into the theoretical aspects of this project. Tony also proved to be an invaluable source of information and support while I was constructing my first experimental apparatus. I would like to express my thanks to Tony for helping to get started in the right direction.

I would like to thank my father, William, and my mother, Florence, for the advice, support, encouragement and love they have given me over the years. They have always been by my side to share in my excitement and they have been there to

give me encouragement when I failed; thanks mom and dad! I also thank my wife's parents, Jim and Joyce Williams, for the support and encouragement they have given me throughout my college career. Joyce (mom) has a very bright outlook on life and no matter how bad things get she will show me the bright side (even if I don't want to see it!) and cheer me up. They have all been very understanding of the many demands on my time which prevents my wife, children and me from visiting home as often as we would like.

I would like, most of all, to thank my wife Kim. Kim has patiently endured life with a college student through eight years of marriage and has given me two beautiful children along the way. She has often had to carry more than her fair share of the workload and for this I am grateful. The love and support from my wife and children has been a great source of strength and encouragement.

The financial support which allowed the completion of this work is greatly appreciated. This support included a three year fellowship from the Areas of National Need program under the U.S. Department of Education and a grant from the Defense Advanced Research Projects Agency. I would also like to thank the department of physics for the many tuition waivers and assistantships which I received.

TABLE OF CONTENTS

Chapter Page

LIST OF TABLES

LIST OF FIGURES

CHAPTER I

INTRODUCTION

ZnSe: Search for blue emitter

Since the first observations of electroluminescence from zinc selenide (ZnSe) in 1963 by Lozykowski[1] and independently by Aven and Cusano[2], researchers have seen the potential for the use of ZnSe as a blue emitter. Over the last three decades much experimental and theoretical effort has been directed toward developing blue LED's and laser diodes based on ZnSe. Although there are numerous reports of electroluminescence from ZnSe [1–10] most were also found to emit red, green and sometimes yellow. A few of these papers[8–10], however, report pure blue emission but they were plagued by problems associated with lithium doping. These problems will be discussed below.

Research on ZnSe was still in the early stages when, in the early 60's, the first solid state laser diodes were developed. These diode lasers were red emitters based on GaAs. GaAs laser diodes have found numerous applications in devices such as laser printers, video disc players and compact disc players (including CD ROMs).

For many years researchers have realized that if the red LED's and lasers, currently used in devices such as CD ROMs, are replaced with blue, then an order of magnitude increase in storage capacity is possible[11]. Some of the other advantages of blue emitters include

- Faster, low cost color printers by shifting the sensitivity of photoconducting materials from red to blue[12].

- Many of the large, expensive, high power consumption gas lasers which emit blue light could be replaced with smaller, inexpensive laser diodes.
- Blue lasers are more efficient than red lasers for underwater applications, such as communications and mapping, since red light is more highly absorbed.
- Blue LED's, combined with their existing red and green counterparts, would enable the production of flat, full color displays using low cost, low power consumption solid state devices.

Unfortunately, the development of devices based on ZnSe has been hampered by a variety of problems such as self compensation (which prevents p-type doping), twinning, high contact resistance and the lack of suitable substrate material.

It was generally believed that self compensation in ZnSe was due to native defects. Neumark[13], however, proposed that compensation was due to amphoteric defects such as lithium which act as acceptors when they occupy a zinc site (Li_{Zn}) but when incorporated interstitially (Li_i) they behave as donors. Thus, when attempts are made to make p-type ZnSe using lithium as the dopant, undesirable, compensating Li_i donors are incorporated in addition to the Li_{Zn} acceptors. Neumark argues that as more lithium is incorporated into a sample the compensation effect catches up to the doping and saturation is reached (i.e. incorporating more Lithium does not change the free hole concentration). Her calculations lead to the conclusion that the maximum attainable free hole concentration decreases as the exponential of $1/2E_g$ where E_g is the band-gap. Thus, for wide band-gap semiconductors such as ZnSe, high p-type doping levels can not be achieved with lithium. MBE growth of ZnSe:Li by Haase *et al.*[9] at 3M showed that the free carrier concentration not only saturated, as Neumark has shown, but in fact, decreased as more lithium was incorporated after saturation. The free carrier concentration they obtained, $8 \cdot 10^{16} cm^{-3}$, is the highest to date for p-type ZnSe.

Through the continuing efforts at 3M, Cheng *et al.*[14] were able to grow high quality, undoped MBE films at temperatures as low as 150℃. Finally, in June of 1990, 3M reported their success in fabricating the first laser diode based on

ZnSe. The active region of this device was a $Cd_{0.2}Zn_{0.8}Se$ quantum well sandwiched between an n–type (Cl doped) and a p–type (N doped) layer of ZnSe. One month later a collaborative effort between Brown and Purdue universities also produced a working laser diode based on ZnSe[15]. In this case the active region was a CdZnSe multiple quantum well. In both of these cases, however, device lifetime was limited to a few hours or days of heavy operation. It is believed that two of the major causes for device failure are: (1) high voltage drops across electrodes which cause heating and (2) lattice strain at the GaAs/ZnSe interface.

For the growth of ZnSe devices, GaAs has been the substrate material of choice due to its low cost, availability, well characterized surface preparation methods and its close lattice match (0.28%) to ZnSe at room temperature. There are, however, several problems associated with performing heteroepitaxial growth of ZnSe on GaAs. They may be summarized as follows:

- Although the two lattices are closely matched at room temperature, they have different coefficients of thermal expansion (7.0×10^{-6} $^{\circ}C^{-1}$ for ZnSe and 5.8×10^{-6} $^{\circ}C^{-1}$ for GaAs) which may cause severe lattice strain during post–growth cooling as well as during device operation.

- Band–gap offset between ZnSe and GaAs creates potential barriers at the interface which inhibit the flow of charge through the device. In order to overcome these barriers one is forced to use higher operating voltages than would otherwise be required.

- It has been shown that the highly defective structure Ga_2Se_3, forms at the ZnSe/GaAs interface. Creation of this defect structure results in numerous vacancies which may act as traps or recombination centers thus reducing the ability of the device to luminesce at short wavelengths.

In order to overcome many of these problems it is necessary to grow ZnSe on a ZnSe substrate (i.e. homoepitaxy). Unfortunately, large area, high quality ZnSe material suitable for use as substrate is not currently available. Most researchers have chosen to grow very complicated buffer layer structures in an attempt to

minimize effects such as lattice mismatch. Growth of these complicated structures, however, presents a whole new array of problems. Many researchers feel that homoepitaxy is the most appropriate solution to the problems associated with ZnSe growth. Much of the characterization work presented in this thesis was done in cooperation with Eagle Picher* in support of their efforts to develop a new growth technique known as seeded physical vapor transport (SPVT). To date the SPVT technique appears to be the most promising technique for the production of substrate quality ZnSe. Analysis has shown[16] that samples grown by SPVT exhibit greater crystallinity, a smaller concentration of dislocations, and a less complex deep level structure than their melt grown counterparts.

One of the highest quality LED's which has been produced to date was reported by Ohkawa *et al.*[17]. In these devices Ohkawa and his collaborators grew chlorine doped MBE layers of n–type ZnSe on an n–type SPVT ZnSe substrate. A nitrogen doped p–type layer was then grown on the chlorine doped layer. This was the first report of p–type ZnSe homoepitaxial layers. These diodes were found to emit strong blue light at 2.67eV. At room temperature the blue emission was more than an order of magnitude stronger than the red emission and at 77K the red emission was not present. Although these devices worked quite well, the mobility and free carrier concentration were limited due to impurity scattering and compensation.

Crystal Structure and Energy Bands

The crystal structure for ZnSe is the zinc–blende structure shown in Fig. 1. This structure is very similar to the diamond structure in that it contains two interpenetrating fcc (face centered cubic) lattices, one being offset from the other by one–quarter of a body diagonal. In the zinc–blende structure each of these two lattices is composed of a different element (e.g. zinc and selenium). The unit cell is a cube which contains a total of eight atoms in the following configuration: four zinc atoms at $000, 0\frac{a}{2}\frac{a}{2}, \frac{a}{2}0\frac{a}{2}$ and $\frac{a}{2}\frac{a}{2}0$; and 4 selenium atoms at $\frac{a}{4}\frac{a}{4}\frac{a}{4}, \frac{a}{4}\frac{3a}{4}\frac{3a}{4}, \frac{3a}{4}\frac{a}{4}\frac{3a}{4}$

*Eagle Picher Research Labs, Miami, OK

and $\frac{3a}{4}\frac{3a}{4}\frac{a}{4}$. Each atom is tetrahedrally bonded to four nearest neighbor atoms of the opposite type at a distance of $\frac{\sqrt{3}a}{4}$ where a is the lattice constant which has a value of 5.668Å(pg. 80 of Cohen and Chelikowski[18]).

The bond formed in zinc selenide is neither purely ionic or purely covalent but rather it is a mixed bond being approximately 63 percent ionic in nature[18]. A contour plot of the valence charge density is shown in Fig. 2(a), note that the maximum charge density does not lie midway between the atoms (covalent bonding) nor does it coincide with one of the atoms (ionic bonding). For comparative purposes charge density plots for a strongly covalent system (Si) and a strongly ionic system (NaCl) are also shown. Note the relative locations of the charge density maximum in each of these other systems.

The calculated energy band structure for ZnSe is shown in Fig. 3. This figure shows several valence and conduction bands but of particular interest is the valence band maximum (Γ_8^v) and the conduction band minimum (Γ_6^c) which both occur at $\mathbf{k}$=0 (i.e. the gamma point). Thus, ZnSe is a direct band–gap semiconductor. According to this calculation the direct gap has a width of 2.76eV. Experimental observations usually give values near 2.82eV at 0K and 2.713eV at 300K[20]. We also notice from this figure that the greater curvature of the conduction band indicates that the electron effective mass is smaller than the hole effective mass. The effective mass ratio, m^*/m, for electrons and holes is 0.17 and 0.65, respectively.

Thesis Project

It is the aim of this thesis to arrive a more complete understanding of the many materials problems associated with zinc selenide and the development of devices based on this material. This is the first extensive study which has been undertaken to study the deep level defect structure of SPVT ZnSe.

The specific goals of this thesis are to develop, test and implement new theoretical descriptions of some of the methods used in this study as well as to identify and model the trapping processes involving deep level defects and impurities in

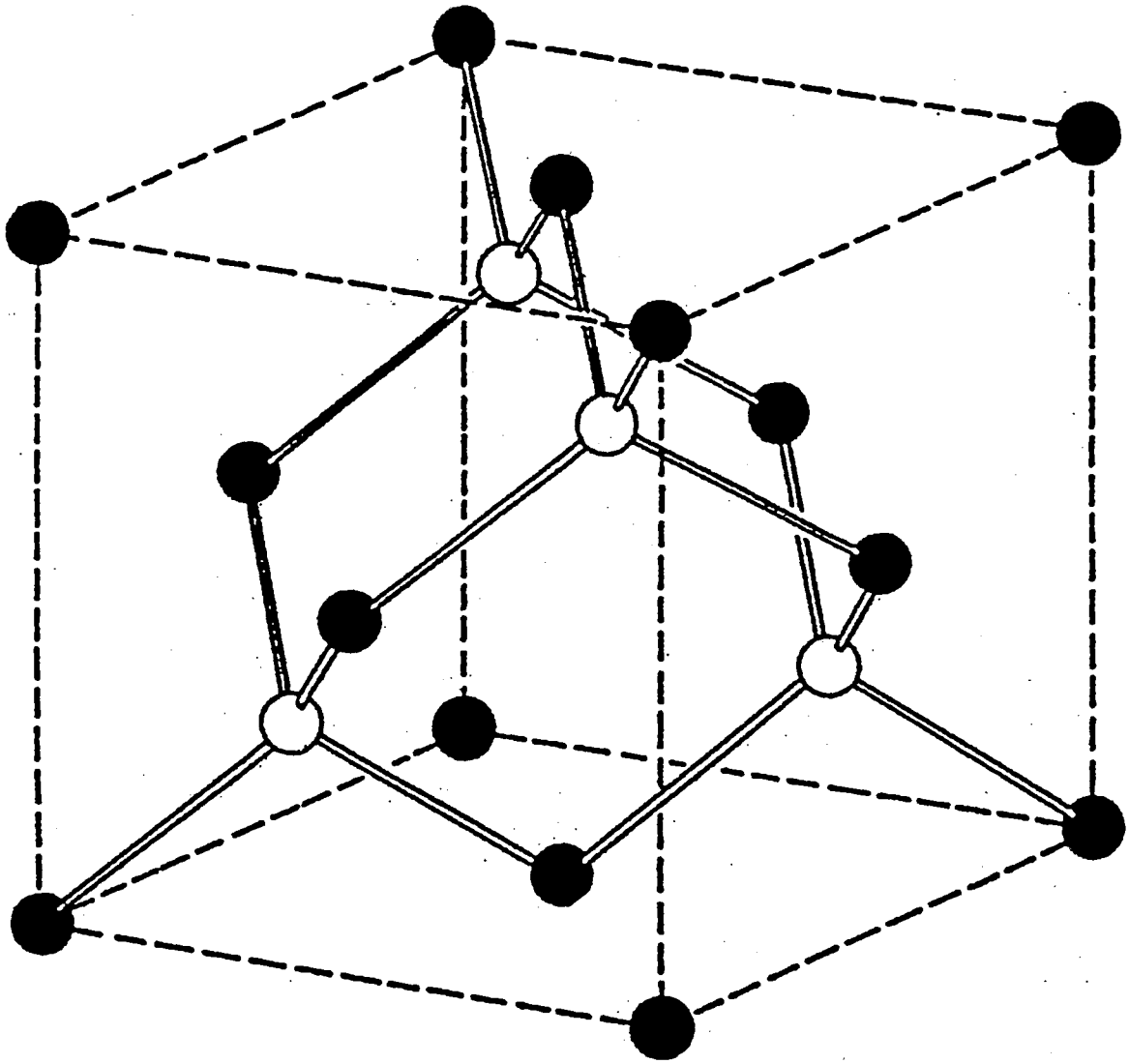

Figure 1. Crystal structure of cubic zinc selenide. Solid circles represent zinc atoms and open circles represent selenium atoms (Kittel[17]).

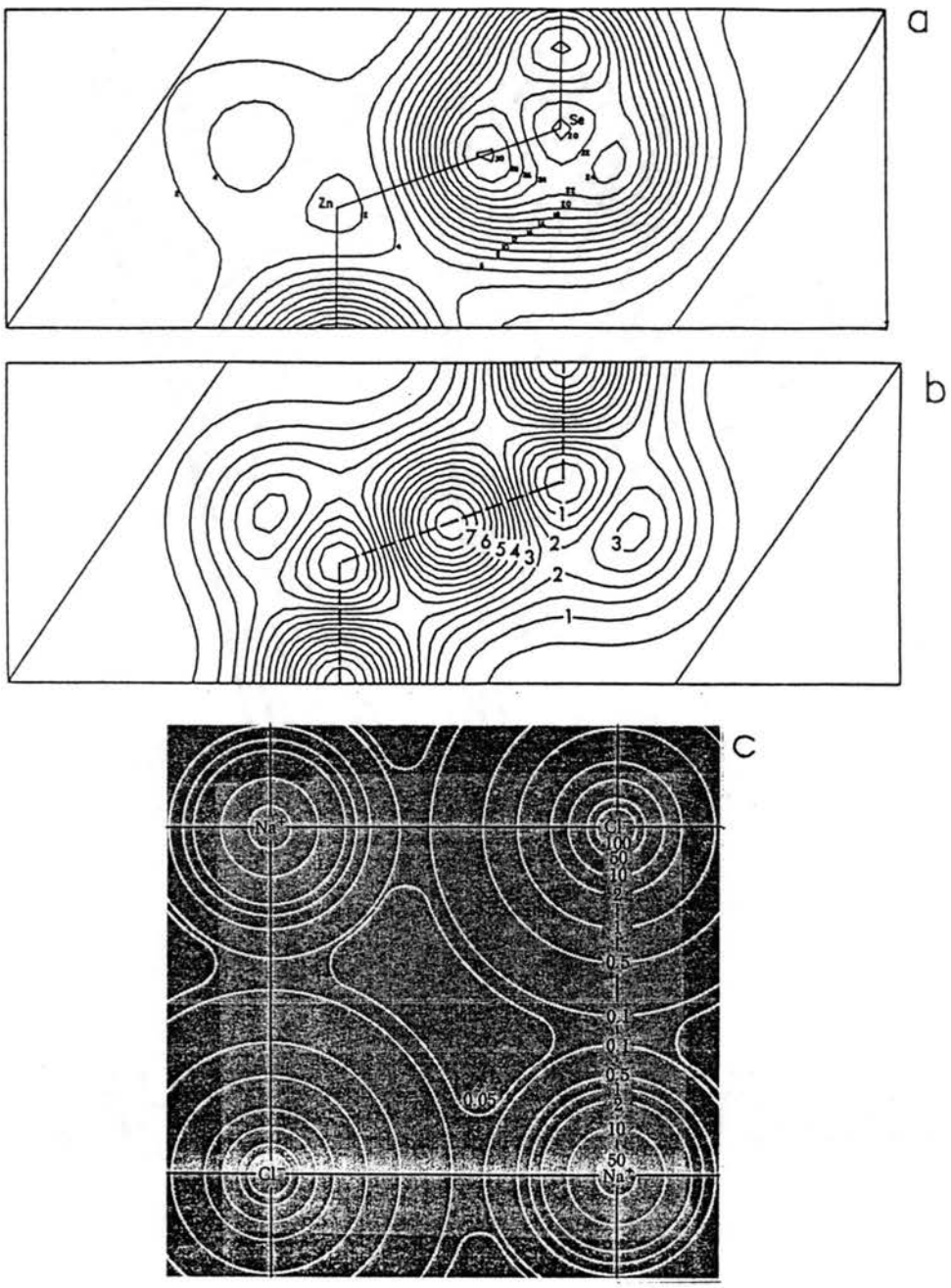

Figure 2. The above contour plots show the valence charge density in units of electrons per unit cell volume for (a) ZnSe, (b) Si and (c) NaCl. Notice the differences in the location of the charge maximum in highly covalent crystals (Si), highly ionic crystals (NaCl) and crystals which exhibit mixed bonding (ZnSe) ((a) and (b) from Cohen and Chilakowski[18], (c) from Kittel[19]).

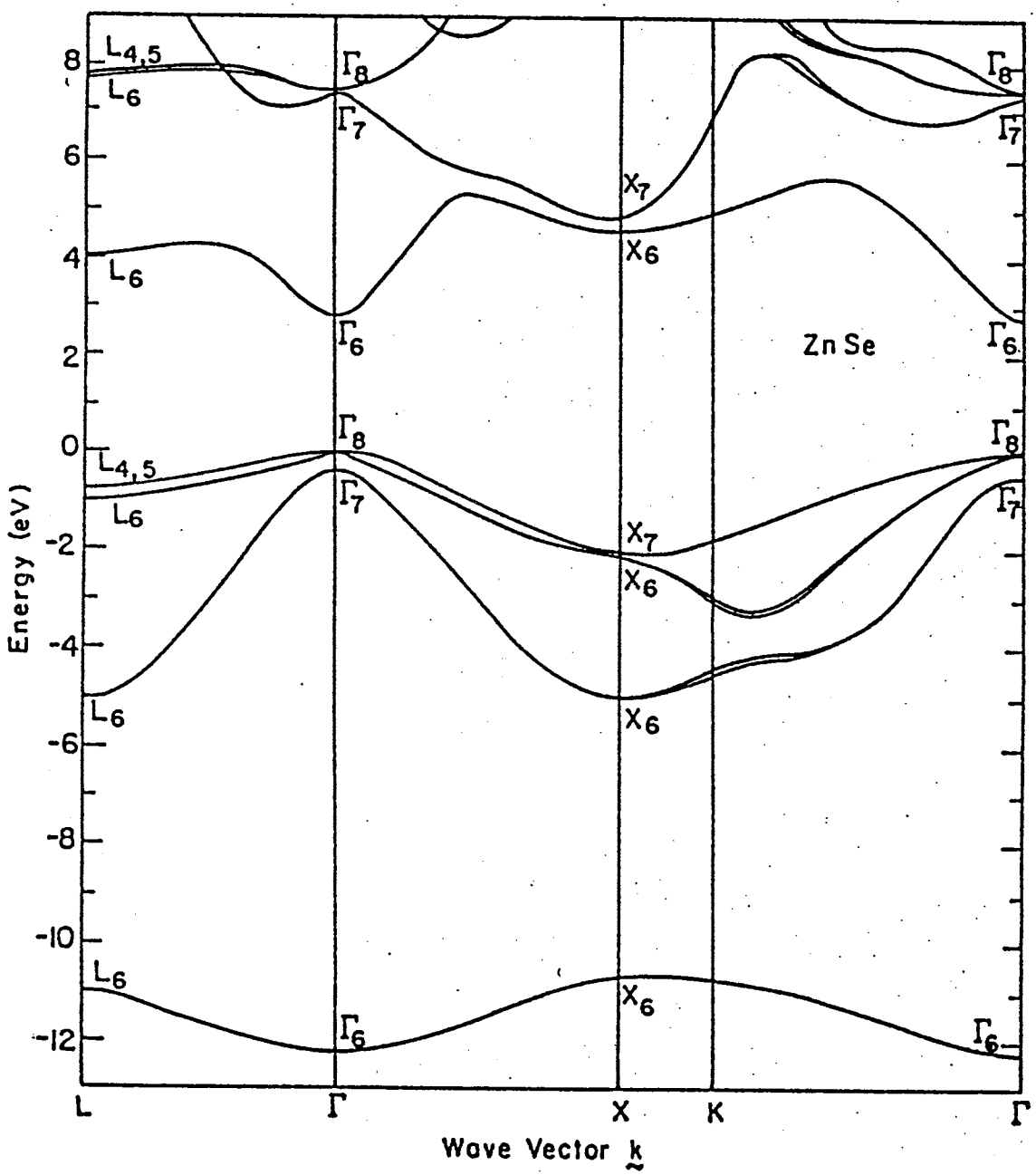

Figure 3. Calculated band structure for ZnSe. The energy at the top of the valence band (Γ_8^v) is assumed to be zero.

both melt grown(MG) and seeded physical vapor transport grown zinc selenide. The primary purpose for characterization of melt grown samples is to form a basis for comparison. By comparing many of the finding for SPVT samples to those finding for MG samples, the superior quality of the SPVT samples becomes more apparent.

The samples studied included as–grown, semi–insulating MG and SPVT samples, in which the resistivity was often too high to be measured; and SPVT samples which had been treated in molten zinc in order to reduce their resistivity. This method will be elaborated in chapter V. No low resistivity MG samples were available.

In chapter III the experimental procedures employed in the study of high resistivity samples are presented. Also presented in chapter III are the results obtained from these experiments. The methods used to characterize the high resistivity samples include thermally stimulated current (TSC), thermoluminescence (TL), photoconductivity (PC) and photoluminescence (PL). For reasons described at the beginning of chapter III, not all of the methods employed are appropriate for low resistivity samples.

The theoretical description of TSC and TL was originally developed in 1945 and remained virtually unchanged for 45 years. Recently, however, significant developments have been made[21–23]. Detailed developments of both theories are presented in chapter II. Chapter II also includes computer modeling of TSC and TL for the purpose of testing both the new and old theoretical descriptions.

Low resistivity samples were fabricated into Schottky diodes and analyzed by the method of deep level transient spectroscopy (DLTS). The development of the DLTS method is presented in chapter IV and the results of experiment are given in chapter V.

Finally, in chapter VI, the results of all experiments are summarized and the connection between various experimental results is made. By comparing results for different samples and for different experiments a better understanding of the

deep level structure is gained and a model is presented which describes the major features of, and differences between, MG and SPVT zinc selenide.

CHAPTER II

THEORY OF TSC AND TL

Introduction

When a semiconductor or insulator is heated, following band-gap excitation at low temperature, one may measure transient light emission (thermoluminescence or TL) and transient enhancement of electrical conductivity* (thermally stimulated current or TSC). The characteristics of the resulting TL and TSC are dictated by the properties of deep levels within the band-gap.

Before discussing the theoretical development of TSC and TL one should have a qualitative understanding of the processes involved. In the following discussion, reference is made to the model shown in Fig. 4. The transition numbers used below are in reference to this figure.

In a TSC or TL experiment, the sample is cooled to low temperature and is illuminated with a light source which excites carriers across the band-gap. Some of these carriers become trapped (transitions 1 and 3) where they will remain until a sufficient amount of thermal energy is applied through heating to excite the trapped carriers to their respective delocalized band (transitions 2 and 4). This heating is normally performed on a linear time scale at a heating rate β (i.e. $T = T_0 + \beta t$). When a sufficient amount of thermal energy is applied, the trapped electrons (or holes) are thermally excited to the delocalized band, transition 2 (4), where they contribute to the electrical current thus giving rise to thermally stimulated current transients. Some of the detrapped electrons (holes) may recombine with trapped holes (electrons), transition 5 (6), and lose energy in the form of radiation (i.e.

*Although thermally stimulated *current* and *conductivity* are often used synonymously, what is actually *measured* is current, not conductivity.

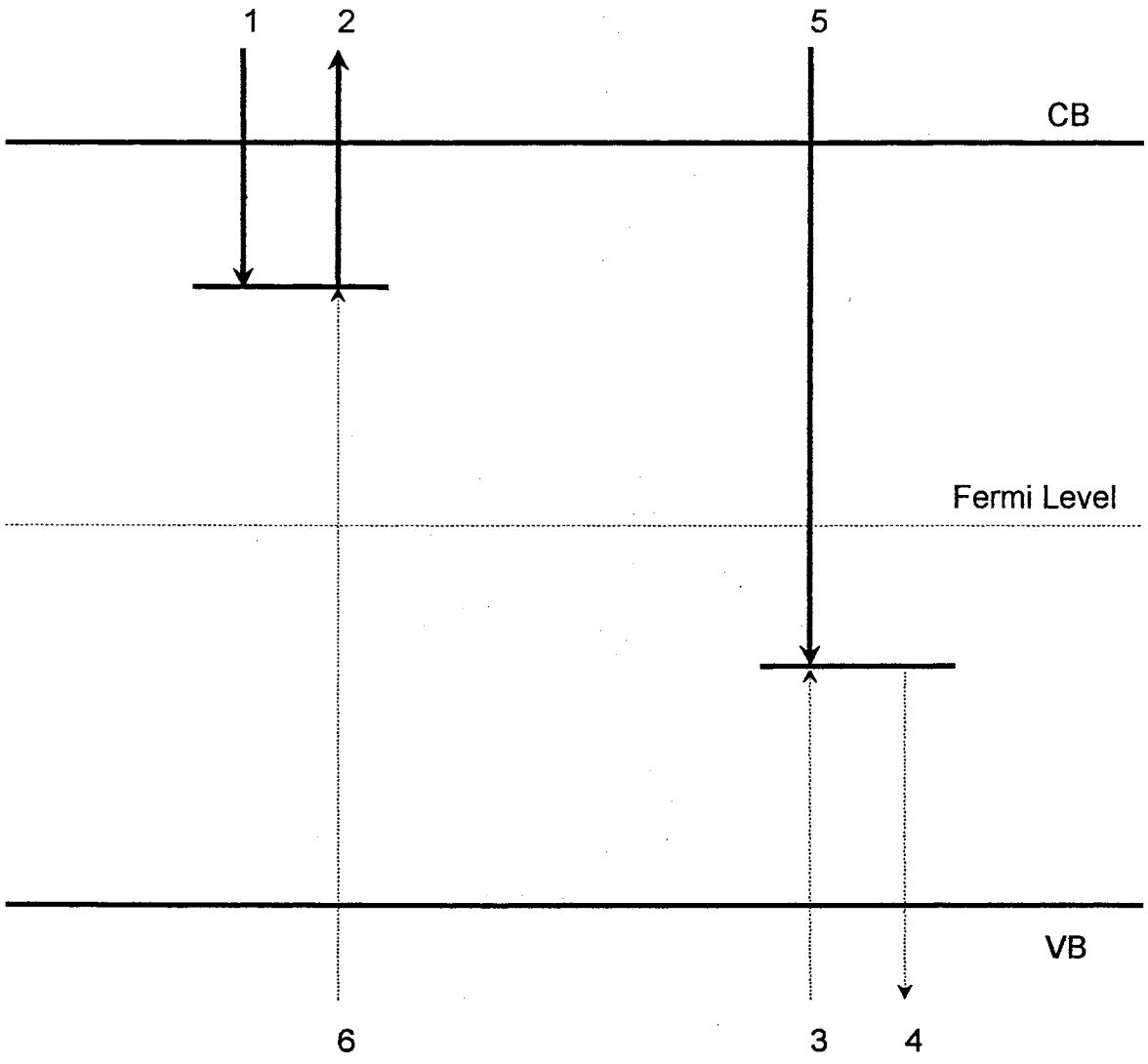

Figure 4. Energy band model of single level system used to describe TSC and TL. Solid vertical lines represent electron transitions and dashed lines represent hole transitions.

thermoluminescence). Since the concentrations of the various defect levels are usually small (for example: $\sim 10^{12}$ to $10^{16} cm^{-3}$) compared to carrier concentrations of low resistivity semiconductors (10^{18} to $10^{22} cm^{-3}$), the associated TSC signals are very weak; often on the order of a few pico-amps at fields strengths of a few volts per mm. Since the background currents in low resistivity semiconductors (at similar fields) are many orders of magnitude larger, it is not possible to measure TSC for these samples. Similarly, TL is not measured in low resistivity samples since the high carrier concentration causes a rapid depletion of recombination centers. Although not useful for low resistivity samples, TSC and TL are very sensitive techniques capable of detecting very low defect concentrations. Townsend and Kelly[24] have shown that TL is sensitive enough to detect as few as 10^9 defects in a given sample.

Now that the basic model for the system under study has been introduced, some discussion regarding terminology is in order. The terms donor, electron trap, acceptor, hole trap and recombination center are often misused in the literature. The most common error is calling a donor an electron trap or vice–versa (similarly for acceptors and hole traps). Donors, electron traps and electron recombination centers will be discussed below but keep in mind that the same arguments also apply to acceptors, hole traps and hole recombination centers.

A donor is an impurity which gives rise to an energy level within the band–gap and is neutral at zero Kelvin. As the temperature increases the donor becomes ionized thus 'donating' an electron to the conduction band. As the temperature is again lowered the ionized donor reclaims an electron from the conduction band and returns to its neutral state. Although, at lower temperatures, the donor captures an electron, it is not considered a trap since it is simply reclaiming what it donated earlier. An electron trap, on the other hand, does not have excess electrons to donate to the conduction band at high temperatures. Traps do, however, capture electrons from the conduction band at lower temperatures possibly removing the electrons which were thermally excited from shallow donors (i.e. compensation).

An electron recombination center is often referred to as a hole trap. This defect level contains trapped holes which act as recombination sites for electrons in the conduction band. At higher temperatures there may be sufficient thermal energy to excite these holes to the valence band. The excitation of carriers out of a defect is indicative of trap like behavior. This may be summarized as follows: if the probability of recombination is much greater than the probability of thermal excitation the center is a recombination center. If , however, the probability of excitation is greater then the center is a trap. From this argument, it can be seen that a given defect may act as a trap at high temperatures and as a recombination center at low temperatures.

Development of Theory

In order to describe the kinetics of TSC and TL, various transitions shown in Fig. 4 must be described. Keep in mind we are only considering electron detrapping and recombination with trapped holes (i.e. transitions 1,2 and 5). In considering the capture of electrons (transition 1) by traps of concentration N and cross sections S, it is easier to imagine the traps traveling through a sample in which the free electrons are stationary. Assume that the concentration of previously filled traps is n and that the traps are moving at a velocity v_e where v_e is the thermal velocity of electrons in the conduction band. As the $(N-n)$ empty traps travel through the sample they sweep out a fractional volume per unit time of $(N-n)Sv_e$. Therefore, the rate of electron capture is $n_c(N-n)Sv_e$ where n_c is the free electron concentration.

The thermal excitation of an electron from a trap of depth E below the conduction band (transition 2) is characterized by the attempt to escape frequency s and the probability of thermal excitation $\exp(-E/kT)$ where k is Boltzmann's constant. The product of these two terms gives the probability per unit time of an electron being thermally excited to the conduction band. The rate of excitation is thus given as $ns\exp(-E/kT)$.

The expressions for the rates of trapping and detrapping may be combined to give the time rate of change of trapped electrons, namely

$$\frac{dn}{dt} = n_c(N-n)Sv_e - ns\exp\left(-\frac{E}{kT}\right). \tag{1}$$

The quantity s, referred to as the frequency factor, or attempt frequency, may be written as

$$s = N_c S v_e \tag{2}$$

Where N_c is the effective density of states in the conduction band. N_c and v_e are given by:

$$N_c(T) = 2\left(\frac{kTm^*}{2\pi\hbar^2}\right)^{3/2} \tag{3}$$

and

$$v_e(T) = \sqrt{\frac{3kT}{m^*}} \tag{4}$$

Where m^* is the electron effective mass in the conduction band.

It is usually assumed that the frequency factor s (Eqn. (2)) follows a power law temperature dependence[25], that is,

$$s(T) = BT^{2-b} \tag{5}$$

where B and b are constants and $0 \leq b \leq 4$. By combining equations (2), (3) and (4) it is found that the capture cross section also follows a power law temperature dependence defined as

$$S(T) = \frac{B\left(2\pi\hbar^2\right)^{3/2}}{2\sqrt{3}m^*k^2}T^{-b} = CT^{-b} \tag{6}$$

where C is a parameter dependent upon the effective mass.

There are two paths through which charge may be added to or removed from the conduction band: (1) The trap level is capable of both adding and removing charge. Any charge added to (removed from) the trap level is removed from (added to) the conduction band; (2) The recombination path removes charge from the

conduction band through the recombination of an electron and a trapped hole. The rate of this recombination is n_c/τ where τ is the recombination lifetime.

The rate equations describing the rate of change of free and trapped charge may be written as:

$$\frac{dn}{dt} = n_c(N-n)Sv_e - nN_cSv_e \exp\left(-\frac{E}{kT}\right) \tag{7}$$

and

$$\frac{dn_c}{dt} = -\frac{dn}{dt} - \frac{n_c}{\tau} \tag{8}$$

where the temperature dependencies of S, v_e and N_c are implicit.

The solution of equations (7) and (8) usually proceeds from two fundamental assumptions which were first introduced by Randall and Wilkins[26] in 1945. The assumptions are: (1) the rate of retrapping of charge that has been released from a trap is negligible compared to the rate of recombination (i.e. first-order kinetics), and (2) the system is close to equilibrium. That is, the rate of change of free electrons is small compared to the detrapping and recombination rates (i.e. Quasi-Equilibrium or QE). These assumptions may be expressed as

$$\frac{n_c}{\tau} \gg n_c(N-n)Sv_e \tag{9}$$

and

$$\left|\frac{dn_c}{dt}\right| \ll \left|\frac{dn}{dt}\right| \tag{10}$$

respectively.

Applying these approximations to equations (7) and (8) leads to

$$\frac{dn}{dt} \approx -ns \exp\left(-\frac{E}{kT}\right) \tag{11}$$

and

$$\frac{dn}{dt} \approx -\frac{n_c}{\tau} \tag{12}$$

Integration of equation (11), using the relationship $T = T_0 + \beta t$, results in

$$n = n_0 \exp\left\{ - \int_{T_0}^{T} \frac{s(\Theta)}{\beta} \exp\left(-\frac{E}{k\Theta}\right) d\Theta \right\} \tag{13}$$

Where n_0 is the initial trapped electron concentration and Θ is temperature.

Substituting equations (12) and (13) into equation (11) leads to

$$n_c = n_0 \tau s(T) \exp\left(-\frac{E}{kT}\right) \exp\left\{ - \int_{T_0}^{T} \frac{s(\Theta)}{\beta} \exp\left(-\frac{E}{k\Theta}\right) d\Theta \right\} \tag{14}$$

Substitution of equation (5) for s in the above equation results in an integrand which is a product of a power law and an exponential. An approximate closed form expression for this type of integral was obtained by Keating[27]. Applying his approximation to equation (14) leads to the following closed form expression for the free carrier concentration:

$$\begin{aligned} n_c(T) &= n_0 \tau B T^{2-b} \exp\left(-\frac{E}{kT}\right) \\ &\quad \times \exp\left\{ \frac{-BkT^{4-b}}{\beta E} \left(1 + \frac{(b-4)kT}{E}\right) \exp\left(-\frac{E}{kT}\right) \right\} \\ &= n_0 \tau F(T) \end{aligned} \tag{15}$$

Using the above expression, it is now possible to describe TSC and TL in terms of the parameters B (or C), E, b, n_0 and β. In general, one might expect both radiative (characterized by τ_r) and non-radiative (τ_{nr}) recombination pathways in which case TL is given by

$$TL = \frac{n_c}{\tau_r} \tag{16}$$

where τ, τ_r and τ_{nr} are related through the expression.

$$\frac{1}{\tau} = \frac{1}{\tau_r} + \frac{1}{\tau_{nr}}. \tag{17}$$

From the free carrier concentration the TSC is evaluated according to

$$TSC(T) = Ae\mu\mathcal{E}n_c \tag{18}$$

where A is the electrode area, e is the electron charge, μ is the electron mobility and $\mathcal{E}$ is the applied electric field.

Substituting equation (15) into equations (18) and (16) we have

$$TSC(T) = C'\mu n_0 \tau F(T) \tag{19}$$

and

$$TL(T) = n_0 \frac{\tau}{\tau_r} F(T) \tag{20}$$

where the constants A, e and $\mathcal{E}$ have been absorbed into the constant C'. Equations (19) and (20) are often used as fitting equations when analyzing TSC and TL. It is usually assumed that both $\mu\tau$ and τ/τ_r are constants and the fitting parameters become n_0 (or C'), b, B, and E.

From the above equations we see that TSC and TL have very similar characteristics and, depending on the temperature dependencies of μ, τ and τ_r they may have close or identical peak positions. The factors influencing relative peak positions will be examined in the following section.

TSC and TL correlations

In order to examine the TL process more fully, a more complete expression for the rate of capture of electrons by recombination centers must be obtained. Let m represent the concentration of holes trapped at the recombination center. Through an argument similar to that used earlier to derive the capture rate for a trap, the following expression is derived to describe the rate of recombination

$$\begin{aligned} \frac{dm}{dT} &= -\frac{1}{\beta} R v_e m n_c \\ &= -\frac{A_r}{\beta} m n_c \end{aligned} \tag{21}$$

where R is the recombination cross section, A_r is the transition probability for recombination ($\mathrm{cm^3 s^{-1}}$) and the TL intensity is given by $-dm/dt$ ($-\beta \times dm/dT$).

In a first attempt to understand the correlation between the peak maxima of TSC and TL, Chen[28] assumed that A_r was constant so that integration of

equation (21) gives

$$m = m_0 \exp\left(-\frac{A_r}{\beta}\int_{T_0}^{T} n_c d\Theta\right) \tag{22}$$

where m_0 is the concentration of trapped holes at the beginning of the experiment (i.e. when $T = T_0$). Substitution of equation (22) into equation (21) leads to the following expression for TL

$$TL(T) = n_c A_r m_0 \exp\left(-\frac{A_r}{\beta}\int_{T_0}^{T} n_c d\Theta\right) \tag{23}$$

Equating the temperature derivative of the above equation to zero results in the following expression which is true at the maximum of the TL curve

$$\left.\frac{dn_c}{dT}\right|_{T_m} = \frac{A_r}{\beta} n_{c_m}^2 \tag{24}$$

where T_m is the temperature of the TL maximum and n_{c_m} is the free carrier concentration at T_m. Each quantity of the right hand side of equation (24) is always positive, thus, the left hand side must also be positive. This indicates that at the peak of the TL, the TSC (actually n_c) will always be increasing. In other words, the peak of the TL curve will appear at a lower temperature than the peak of the TSC curve.

A troubling point in the above analysis is that Chen has completely ignored the temperature dependence of A_r. The transition probability A_r may be weakly dependent upon temperature, thus varying very little over the temperature range of a single TL peak. In order to analyze TSC and TL correlations correctly, however, the effects of temperature dependence must be examined. A_r is the product of the two temperature dependent quantities R and v_e. If R is assumed to have a temperature dependence of T^{-d}, similar to the capture cross section (equation (6)), then A_r may be written as

$$A_r(T) = A_{r_0} T^{1/2-d} \tag{25}$$

where A_{r_0} and d are constants and $0 \leq d \leq 4$. By once again taking the temperature derivative of equation (23), this time accounting for the temperature

dependence of A_r, the following relationship is obtained

$$\left.\frac{dn_c}{dT}\right|_{T_m} = \frac{A_{r_m}}{\beta} n_{c_m}^2 - \frac{1/2 - d}{T_m} n_{c_m} \tag{26}$$

where A_{r_m} is the transition probability evaluated at T_m. If the case is considered in which the peak of n_c occurs at a lower temperature than the TL peak, then the left side of equation (26) is negative which leads to

$$A_{r_m} n_{c_m} < (1/2 - d)\beta. \tag{27}$$

Since the term on the left is always positive, the term on the right must be positive as well. This leads to the requirement that $d < 1/2$[29]. This is a necessary but not a sufficient condition to satisfy the inequality. If, on the other hand, the inequality is reversed (TL peak occurs at lower temperature), then there is no additional restriction on the allowed values for d.

By examining equations (16) and (21) it is seen that the radiative recombination lifetime τ_r may be expressed as

$$\begin{aligned} \tau_r &= \frac{1}{A_{r_m} m} \\ &= \frac{1}{R v_e m} \end{aligned} \tag{28}$$

As argued above, if A_r is constant then the TL peak should occur at a lower temperature than the peak of n_c. Since TL is defined as the recombination rate n_c/τ_r, the shift in peak maxima is due to the temperature dependence of τ_r or more directly, the temperature dependence of m. Initially, as n_c increases, the rate of recombination increases. At higher temperatures, although n_c may still be increasing, the rate of recombination decreases due to the depletion of available recombination centers m. From this argument it is difficult to justify the often made assumption that the recombination lifetime is a constant; this can only be true if m is a constant. Obviously if TL is being measured, m is not constant. In order to reconcile this contradiction, the idea of thermally disconnected traps was introduced[30]. A thermally disconnected trap is simply a trap which is deeper that the

trap which is involved in the TL process and is thus thermally stable throughout the temperature range of the TL peak. If the concentration of thermally disconnected traps H is sufficiently large ($H \gg N$), then charge neutrality demands that the concentration of full recombination centers m must also be large. In this case, the change in the concentration of trapped holes during a measurement is negligible compared to the total concentration and the recombination lifetime is nearly constant. It has been shown[31,32] that a large concentration of thermally disconnected traps is necessary in order for the TL and n_c peaks to coincide.

The Randall Wilkins expression (equation (14)) was originally derived to describe TL. A consequence of the findings reported above is that TSC data cannot be properly described by the Randall Wilkins expression unless the concentration of thermally disconnected traps is large. As pointed out by McKeever[33], however, this is not a serious problem in most real systems. McKeever argues that there are usually many trap levels which are deeper than the levels which initiate the observed TL and TSC.

Other Models

In the development of first–order kinetics Randall and Wilkins[26] assumed that an electron, once released from a trap, has a negligible probability of recapture. Within a few years after this theory was introduced, Garlick and Gibson[34] considered the case in which the transition probabilities for trapping (A_t) and recombination (A_r) are equal. Thus, detrapped electrons recombine at a rate $A_r n_c m$ and are retrapped at a rate $A_t n_c (N-n)$. In the absence of thermally disconnected traps, charge neutrality demands that $m = n$. The probability that a detrapped electron will undergo recombination, rather than recapture, is expressed as

$$\alpha = \frac{A_r n_c m}{A_t n_c (N-n) + A_r n_c m} \tag{29}$$

Substitution of $m = n$ and $A_r = A_t$ leads to

$$\alpha = \frac{n}{N} \tag{30}$$

Consider an infinitesimal interval of time δt; the concentration of electrons which are detrapped is equal to $\frac{dn}{dt}\delta t$. Only a fraction α of these electrons are actually lost through recombination; the remaining electrons are retrapped. Thus, the actual concentration of electrons which are 'lost' during the interval δt is $\alpha\frac{dn}{dt}\delta t$. Therefore, the inclusion of retrapping reduces the rate of change of trapped electrons by the factor α. The modified rate equation, as presented by Garlick and Gibson, is

$$\frac{dn}{dt} = -n^2 \frac{s}{N} \exp\left(-\frac{E}{kT}\right). \tag{31}$$

Compare to equation(11). Solving the above equation subject to the QE approximation, yields

$$n_c = n_0^2 \tau \frac{S}{N} \exp\left(-\frac{E}{kT}\right) \left[1 + \frac{n_0}{\beta N} \int_{T_0}^{T} s(\Theta) \exp\left(-\frac{E}{k\Theta}\right) d\Theta\right]^{-2} \tag{32}$$

For kinetics, which are neither first or second order, Partridge and May[35] introduced a purely empirical relationship in which the kinetic order is defined by a parameter l. In this 'general–order' case it is difficult to attach a physical meaning to the parameter l. The time rate of change of trapped electrons is given by

$$\frac{dn}{dt} = s' n^l \exp\left(-\frac{E}{kT}\right) \tag{33}$$

where s' is a constant ($\mathrm{s}^{-1}\mathrm{cm}^3(l-1)$).

Chen[36] solved the general–order equation subject to the QE approximation. The resulting equation is

$$n_c = s' n_0^l \tau \exp\left(-\frac{E}{kT}\right) \left\{\frac{(l-1)s' n_0^{l-1}}{\beta} \int_{T_0}^{T} \exp\left(-\frac{E}{k\Theta}\right) d\Theta + 1\right\}^{\frac{-l}{l-1}} \tag{34}$$

Although a great deal of work has been done on second-order and general-order kinetics, nearly all well studied systems are dominated by first-order kinetics.

Generalized Description of TSC and TL

In the previous section first-, second- and general-order kinetics were examined. Each of these models proceeds from the assumption of quasi-equilibrium.

Lewandowski and McKeever[21], however, have forgone the assumption of quasi-equilibrium and the assignment of a specific kinetic order in favor of a generalized description in which quasi-equilibrium and kinetic order are described by the functions $q(T)$ and $P(T)$, respectively.

The $q(T)$ function is defined in the following manner:

$$q(T)\frac{n_c}{\tau} \equiv \frac{dn_c}{dt} \tag{35}$$

combining with equation (8), we can write

$$Q(T)\frac{n_c}{\tau} = -\frac{dn}{dt} \tag{36}$$

where $Q(T) \equiv q(T)+1$. The kinetic order function, $P(T)$, is defined by the relation

$$P(T) \equiv \tau(N-n)Sv_e \tag{37}$$

Notice the similarity between the two above equations and equations (12) and (9) respectively.

Combining the definition of $Q(T)$ with equation 7 leads to

$$n_c = \frac{nN_cSv_e}{\frac{Q}{\tau}+(N-n)Sv_e}\exp\left(-\frac{E}{kT}\right) \tag{38}$$

Substituting equations (28) and (37) into equation (38) leads to

$$n_c = \frac{SN_c}{R(Q+P)}\frac{n}{n+H}\exp\left(-\frac{E}{kT}\right) \tag{39}$$

where charge neutrality has allowed the substitution $n+H=m$.

If equation (39) is substituted back into equation (36) and combined with the definition of $P(T)$, equation (37), the following differential equation in n is obtained

$$\frac{1}{n}\frac{dn}{dT} = -\frac{QN_cSv_e}{\beta(Q+P)}\exp\left(-\frac{E}{kT}\right) \tag{40}$$

where $\frac{1}{\beta}dT$ has been substituted for dt.

Integration of the above equation leads to a result similar in form to equation (13); namely

$$n = n_0 \exp\left\{-\frac{1}{\beta}\int_{T_0}^{T} \frac{Q(\Theta)}{Q(\Theta)+P(\Theta)} s(\Theta) \exp\left(-\frac{E}{k\Theta}\right) d\Theta\right\} \tag{41}$$

In order to obtain an expression for $n_c(T)$, the above equation must be substituted into equation (39). Since n appears twice in equation (39), the substitution leads to a very long, complicated expression. In order to simplify this expression, Lewandowski and McKeever[21] employed the expansion

$$\frac{n}{n+H} = \sum_{i=1}^{\infty}(-1)^{i+1}\left(\frac{n}{H}\right)^i \tag{42}$$

which is valid for $H > n$. With this expansion, substitution of equation (41) into equation (39) yields

$$n_c = \frac{SN_c}{R(Q+P)} \exp\left(-\frac{E}{kT}\right) \sum_{i=1}^{\infty}(-1)^{i+1}\left(\frac{n_0}{H}\right)^i \exp\left(-i\, g(T)\right) \tag{43}$$

where

$$g(T) = \frac{1}{\beta}\int_{T_0}^{T} \frac{Q(\Theta)}{Q(\Theta)+P(\Theta)} s(\Theta) \exp\left(-\frac{E}{k\Theta}\right) d\Theta \tag{44}$$

It was further argued that if $H \gg n_0$, the series expansion (Eqn. (42)) may be approximated by the first term. In this case the generalized expression for TSC becomes

$$TSC(T) = Ae\mu\mathcal{E}\frac{S(T)N_c(T)n_0}{R(T)H\left(Q(T)+P(T)\right)} \exp\left(-\frac{E}{kT}\right) \exp\left(-g(T)\right) \tag{45}$$

where, for clarity, all temperature dependencies are explicitly indicated.

It is possible to derive the generalized expression for TL without employing the expansion shown in equation (42). Begin by multiplying the numerator and denominator of equation (39) by the thermal velocity v_e. Replace SN_cv_e, in the numerator, with the frequency factor s and replace $v_eR(n+H)$, in the denominator, with τ_r^{-1}. Using the relation $TL = n_c/\tau_r$, we have

$$TL(T) = \frac{n_0 s(T)}{Q(T)+P(T)} \exp\left(-\frac{E}{kT}\right) \exp\left(-g(T)\right) \tag{46}$$

where, once again, all temperature dependencies are explicitly indicated.

Before examining specific cases such as first– or second–order kinetics, it is necessary to better understand the nature of the Q and P functions.

By solving equation (38) for Q we can write

$$Q = \frac{1}{n_c/\tau}\left(nN_cSv_e \exp\left(-\frac{E}{kT}\right) - (N-n)Sv_en_c\right). \tag{47}$$

By identifying the following terms:

$$\begin{aligned} \mathsf{R}_{ex}(T) &\equiv \text{rate of excitation} \\ &= nN_cSv_e \exp\left(-\frac{E}{kT}\right), \end{aligned} \tag{48}$$

$$\begin{aligned} \mathsf{R}_{recomb}(T) &\equiv \text{rate of recombination} \\ &= \frac{n_c}{\tau} = n_cRv_e(n+H) \end{aligned} \tag{49}$$

$$\begin{aligned} \mathsf{R}_{recap}(T) &\equiv \text{rate of recapture} \\ &= n_cSv_e(N-n), \end{aligned} \tag{50}$$

Q may be written as

$$Q(T) = \frac{R_{ex}(T) - R_{recap}(T)}{R_{recomb}(T)}. \tag{51}$$

By substituting $(Rv_e(n+H))^{-1}$ for τ in equation (37), we obtain

$$P(T) = \frac{S(N-n)}{R(n+H)} \tag{52}$$

which may be expressed as

$$P(T) = \frac{R_{recap}(T)}{R_{recomb}(T)}. \tag{53}$$

Consider now the case of first–order kinetics (slow retrapping), in which recombination dominates over recapture; equation (53) reveals that $P \ll 1$. For second–order

kinetics (fast retrapping), on the other hand, recapture dominates over recombination, thus, $P \gg 1$. For cases in which the rate of retrapping is equal to the rate of recombination (the 'retrapping' case), equation (53) indicates that $P = 1$. By comparing equation (36) to equation (12), it can be seen that the assumption of QE demands that $Q(T) \approx 1$. It is instructive to consider, separately, the physical implications of each of the three cases of kinetic order presented above[22]. In each case the assumption of QE is also imposed.

We first consider the case of QE and second–order kinetics ($Q(T) = 1$ and $P(T) \gg 1$). By combining equations (51) and (53), it can be shown that the condition $P \gg 1$ implies that $\mathrm{R}_{ex}(T) \approx \mathrm{R}_{recap}(T)$ for all T which, from equation (51), further implies that $Q(T) = 0$. This is in contradiction with the initial assumption that $Q(T) = 1$. Additionally, if $\mathrm{R}_{ex}(T) \approx \mathrm{R}_{recap}(T)$ for all T, the trap in question would never empty. One concludes from this argument that it *is not possible* to obtain TL or TSC under the conditions of second–order kinetics *and* quasi–equilibrium.

The conditions for the retrapping case are $P(T) = 1$ and $Q(T) = 1$. For $P = 1$, equation (53) implies that $\mathrm{R}_{recap}(T) = \mathrm{R}_{recomb}(T)$. From the definitions of R_{recap} and R_{recomb} this condition may be expressed as $S(T)(N-n(T)) = R(T)(n(T)+H)$. Although this condition does not create a contradiction or violate any physical principles, is seems highly unlikely that this equality would be true for all T. Thus it is unlikely that the retrapping case will be realized in any physical system.

Finally, the case of first–order kinetics is considered ($Q(T) = 1$ and $P(T) \ll 1$). From equation (53) it follows that $\mathrm{R}_{recomb} \gg \mathrm{R}_{recap}$. By combining equations (51) and (53) we find the additional condition that $\mathrm{R}_{ex} \gg \mathrm{R}_{recap}$. These conditions give rise to no contradictions and they are much less restrictive than the *equalities* found in the retrapping case. It can be concluded by these arguments that all or most real systems near quasi–equilibrium should be described first–order kinetics.

Based on the above conclusions, the remainder of this derivation will be performed under the assumption of first–order kinetics. Quasi–equilibrium, however, will continue to be described by the $Q(T)$ function.

Substitution of equation (44) and the condition $P(T) \ll 0$ into equations (45) and (46) yields

$$TSC(T) = Ae\mu\mathcal{E}\frac{S(T)N_c(T)n_0}{R(T)H\,Q(T)}\exp\left(-\frac{E}{kT}\right)\exp\left(-\frac{1}{\beta}\int_{T_0}^{T} s(\Theta)\exp\left(-\frac{E}{k\Theta}\right)d\Theta\right) \tag{54}$$

and

$$TL(T) = \frac{n_0 s(T)}{Q(T)}\exp\left(-\frac{E}{kT}\right)\exp\left(-\frac{1}{\beta}\int_{T_0}^{T} s(\Theta)\exp\left(-\frac{E}{k\Theta}\right)d\Theta\right). \tag{55}$$

By making appropriate substitutions involving τ and $s(T)$ and by imposing the condition $H \gg n$, equation (56) may be rewritten as

$$TSC(T) = Ae\mu\mathcal{E}n_0\frac{\tau(T)s(T)}{Q(T)}\exp\left(-\frac{E}{kT}\right)\exp\left(-\frac{1}{\beta}\int_{T_0}^{T} s(\Theta)\exp\left(-\frac{E}{k\Theta}\right)d\Theta\right) \tag{56}$$

By comparing equation (56) to equations (14) and (19) and comparing equation (55) to equations (14) and (20) it can be shown that

$$TSC_{QE}(T) = Q(T)\,TSC(T) \tag{57}$$

and

$$TL_{QE}(T) = Q(T)\,TL(T), \tag{58}$$

where $TSC_{QE}(T)$ and $TL_{QE}(T)$ are the first–order, quasi–equilibrium solutions (Eqns. (19) and (20)). The solutions to first–order kinetics obtained both with and without the QE assumption merely differ by the factor $Q(T)$, thus, if one can determine the shape of $Q(T)$, then one can correct the QE solutions and describe the TSC and TL curves more exactly.

By combining equations (19) and (20) with the definition of $q(T)$ (Eqn. (35)), the shape of $q(T)$ can be determined from experimental measurements through the following relationships

$$q(T) = \frac{\tau(T)}{\tau_r(T)}\frac{\beta}{TL(T)C\mu}\frac{d}{dT}(TSC(T)) \tag{59}$$

and

$$q(T) = \beta\tau(T)\frac{d}{dT}\ln\left(TSC(T)\right) \tag{60}$$

where the temperature dependence of μ has been ignored in the first equation. If it is further assumed that the temperature dependencies of $\tau(T)$ and $\tau_r(T)$ are the same (which is always true for a single recombination pathway) then their ratio is a constant which may be absorbed into the constant C, thus, allowing the evaluation of $q(T)$ to within a scaling constant. If, however, no TL is observed from the sample under study, equation (60) may be used to evaluate $q(T)$ from TSC data alone. Unfortunately, equation (60) demands that there be prior knowledge of the temperature dependence of τ.

Even if it is possible to experimentally determine the shape of $q(T)$, a problem still remains: it is not know how to properly scale $q(T)$ in order to evaluate $Q(T)$ (recall than $Q(T) = q(T) + 1$).

In an effort to solve the problems associated with evaluating the Q function from experimental data, Lewandowski [37] has managed to eliminate the dependence of the generalized TSC and TL expressions upon $Q(T)$ and $P(T)$. There now exists an expression which has been derived without resorting to the QE assumption. The derivation proceeds from the assumptions that: (1) there is a large concentration of thermally disconnected traps so that $n + H \gg n_c$, for all T, (2) first-order kinetics, (3) the mobility is a constant (i.e. $\mu(T) = \mu$), and (4) $H \gg n_0$. The equation which result from these assumptions are:

$$\begin{aligned} TSC(T) &= K_0^{TSC}\exp\left(\frac{-\Omega T^{3/2-d}}{\beta(3/2-d)}\right)\int_{T_0}^{T}\exp\left(\frac{\Omega\Theta^{3/2-d}}{\beta(3/2-d)}\right)\Theta^{2-b} \\ &\quad \exp\left(-\frac{E}{k\Theta}\right)\times\exp\left\{-\frac{B}{\beta}\int_{T_0}^{\Theta}\Theta'^{(2-b)}\exp\left(-\frac{E}{k\Theta'}\right)d\Theta'\right\}d\Theta \end{aligned} \tag{61}$$

and

$$\begin{aligned} TL(T) &= K_0^{TL}T^{1/2-d}\exp\left(\frac{-\Omega T^{3/2-d}}{\beta(3/2-d)}\right)\int_{T_0}^{T}\exp\left(\frac{\Omega\Theta^{3/2-d}}{\beta(3/2-d)}\right)\Theta^{2-b} \\ &\quad \times\exp\left(-\frac{E}{k\Theta}\right)\exp\left\{-\frac{B}{\beta}\int_{T_0}^{\Theta}\Theta'^{(2-b)}\exp\left(-\frac{E}{k\Theta'}\right)d\Theta'\right\}d\Theta \end{aligned} \tag{62}$$

for $d \neq 3/2$. For the case $d = 3/2$, the above equations reduce to

$$TSC(T) = K_0^{TSC} T^{-\Omega/\beta} \int_{T_0}^{T} \Theta^{\Omega/\beta} \Theta^{2-b} \exp\left(-\frac{E}{k\Theta}\right) \times \exp\left\{-\frac{B}{\beta} \int_{T_0}^{\Theta} \Theta'^{(2-b)} \exp\left(-\frac{E}{k\Theta'}\right) d\Theta'\right\} d\Theta \tag{63}$$

and

$$TL(T) = K_0^{TL} T^{-(1+\Omega/\beta)} \int_{T_0}^{T} \Theta^{\Omega/\beta} \Theta^{2-b} \exp\left(-\frac{E}{k\Theta}\right) \times \exp\left\{-\frac{B}{\beta} \int_{T_0}^{\Theta} \Theta'^{(2-b)} \exp\left(-\frac{E}{k\Theta'}\right) d\Theta'\right\} d\Theta \tag{64}$$

where the various parameters are defined through the parameterization of the recombination cross section $R(T)$, the capture cross section $S(T)$, the recombination lifetime $\tau(T)$, and the frequency factor $s(T)$. The parameterizations are as follows:

$$R(T) = DT^{-d}, \tag{65}$$

$$S(T) = CT^{-b}, \tag{66}$$

$$\frac{1}{\tau} = v_e(T) R(T) H = \Omega T^{1/2-d}, \tag{67}$$

and

$$s(T) = N_c(T) S(T) v_e(T) = BT^{2-b} \tag{68}$$

where B, C, D, Ω, b and d are constants. The constants K_0^{TSC} and K_0^{TL} are defined as:

$$K_0^{TSC} = \frac{A\mathcal{E}e\mu n_0 B}{\beta} \tag{69}$$

and

$$K_0^{TL} = \frac{\tau n_0 \Omega B}{\tau_r \beta} \tag{70}$$

where A is the electrode area, $\mathcal{E}$ is the applied electric field, and e is the electron charge.

Computer Modeling and Testing

Computer modeling was performed in order to compare the generalized solution, equations (61) through (64) to the Randall Wilkins solution, equation (15). Both the Randall Wilkins and generalized solutions were evaluated then compared to exact numerical solutions to the rate equations (7) and (8) which were obtained using a fourth order adaptive Runge–Kutta method (see appendix A).

In order to use the Runge–Kutta method, the rate equations describing the transfer of charge into and out of the trap and the conduction band (equations (7) and (8)) must be fully parameterized and written as derivatives with respect to temperature rather than time. Recall that the heating rate is linear according to $T = T_0 + \beta t$ so that we may replace dt with dT/β. Making this substitution, as well as replacing τ with equation (28), in equations (7) and (8) we have

$$\frac{dn}{dT} = \frac{1}{\beta}\left[n_c(N-n)Sv_e - nN_cSv_e \exp\left(-\frac{E}{kT}\right)\right] \tag{71}$$

and

$$\frac{dn_c}{dT} = \frac{1}{\beta}\left[-n_c(N-n)Sv_e + nN_cSv_e \exp\left(-\frac{E}{kT}\right) - n_cmRv_e\right] \tag{72}$$

The inclusion of m in equation (72) indicates the need for a third rate equation to describe the rate of change of trapped holes in the recombination center. If we make use of charge neutrality, however, the need for a third equation is eliminated. If the recombination center is sufficiently deep that there is no thermal excitation into the valence band then we know that all of the holes reside on recombination centers. We also know that the total number of trapped plus free electrons must add up to the total number of trapped plus free holes (charge neutrality). Mathematically stated

$$m = n + n_c + H. \tag{73}$$

By parameterizing the quantities R and S as in equations (65) and (66) and by parameterizing the density of states and the thermal velocity as $N_c = A_1T^{3/2}$ and

$v_e = A_2 T^{1/2}$ respectively (c.f. equations (3) and (4)), we have

$$\frac{dn}{dT} = \frac{A_2 C T^{2-b}}{\beta}\left[T^{-3/2} n_c (N-n) - A_1 n \exp\left(-\frac{E}{kT}\right)\right] \tag{74}$$

and

$$\frac{dn_c}{dT} = \frac{C A_2 T^{2-b}}{\beta}\left[A_1 n \exp\left(-\frac{E}{kT}\right) - n_c T^{-3/2}\left(N - n + \frac{D}{C} T^{b-d}(n + n_c + H)\right)\right] \tag{75}$$

From the solution of these equations the TL curve can be easily calculated from

$$TL(T) = R v_e n_c m = D A_2 T^{\frac{1}{2}-d} n_c (n + n_c + H) \tag{76}$$

By varying the parameters E, C, D, b and d in the above rate equations it is possible to generate a wide range of TSC and TL curves. In this study, nearly a hundred data sets were generated and subsequently compared to the Randall Wilkins and generalized expressions. Reported here is a sample of these data sets which emphasize the more significant trends which were observed.

After generating data using RK analysis, the resulting TSC and TL curves were fitted* to the RW expression in order to determine parameter values.

The graphs in Fig. 5 show TSC data sets generated using RK which were fitted to the RW expression equation (15). In each data set the activation energy E was 0.3eV and the temperature dependencies of R and S were both -3/2 (i.e. $a = b = 3/2$), other parameters are listed in the figure caption. The results of fitting to TSC (actually n_c) yielded a range of activation energies from 0.291eV to 0.318eV. The 'poorest' fits (largest value for χ^2) † were obtained for data sets (a), (b) and (c), in which both N and H are small ($10^9 m^{-3}$ and $10^{12} m^{-3}$ respectively). When N and H were increased to more physically reasonable values ($10^{10 or 11} m^{-3}$ and $10^{12,13 or 14} m^{-3}$) as in sets (d), (e) and (f), the fits were markedly improved. For set (f), the values of N and H are large but the condition $H \gg N$ is only weakly

*See appendix B for a detailed description of the fitting procedure used.

†See appendix B.

satisfied since $H/N = 10$. As a result, set (f) is not as good a fit as sets (d) and (e).

When fitted to Runge–Kutta TL data, a similar trend is observed (see Fig. 6). In most cases, however, the parameter values obtained from TL fitting are closer to the actual values than those obtained from TSC fitting. In the case of sets (d) and (e), the parameters obtained from TL fitting are nearly perfect.

Also shown in the graphs of Figures 5 and 6 are the Q–functions which were evaluated from the RK data. The Q–function was calculated using equation (47).

We notice, from Figures 5 and 6, that in most cases the Q–function is close to unity (i.e. the system is near QE) for temperatures below the peak maximum. Beyond the peak maximum, however, a sharp decrease in the Q–function is seen. Note that in sets (a), (b) and (c) the quality of the fit is poorest on either side of the peak maximum, this is a direct result of deviations from quasi–equilibrium which render the Randall Wilkins equation invalid. The departure from QE is not as severe in sets (d), (e) and (f), thus the validity of the Randall Wilkins equation is better in these cases.

Although the quality of fit is worse for sets (a), (b) and (c), it has been noticed, in certain instances, that these 'poor fits' actually yield more accurate parameter values. This apparent inconsistency has been addressed in some detail in appendix B. One of the points discussed is the fact that fitting often results in a local χ^2 minimum. As discussed in the appendix, this problem is dealt with by repeating the fit for several sets of initial fitting parameters.

Table I shows fitting values obtained for the data shown in figures 5 and 6. The table shows parameter values obtained for two sets of initial parameter values. The starting parameter values for fit–1 were chosen randomly and the starting values for fit–2 were simply the parameter values which were used in the Runge–Kutta program. The two sets of fitting results exhibit the widest variation in fitted parameters which were found, thus if a particular data set is considered the uncertainty in parameter values may be determined. For example, consider set (b) results for TSC. The activation energy ranges from 0.302eV to 0.318eV so

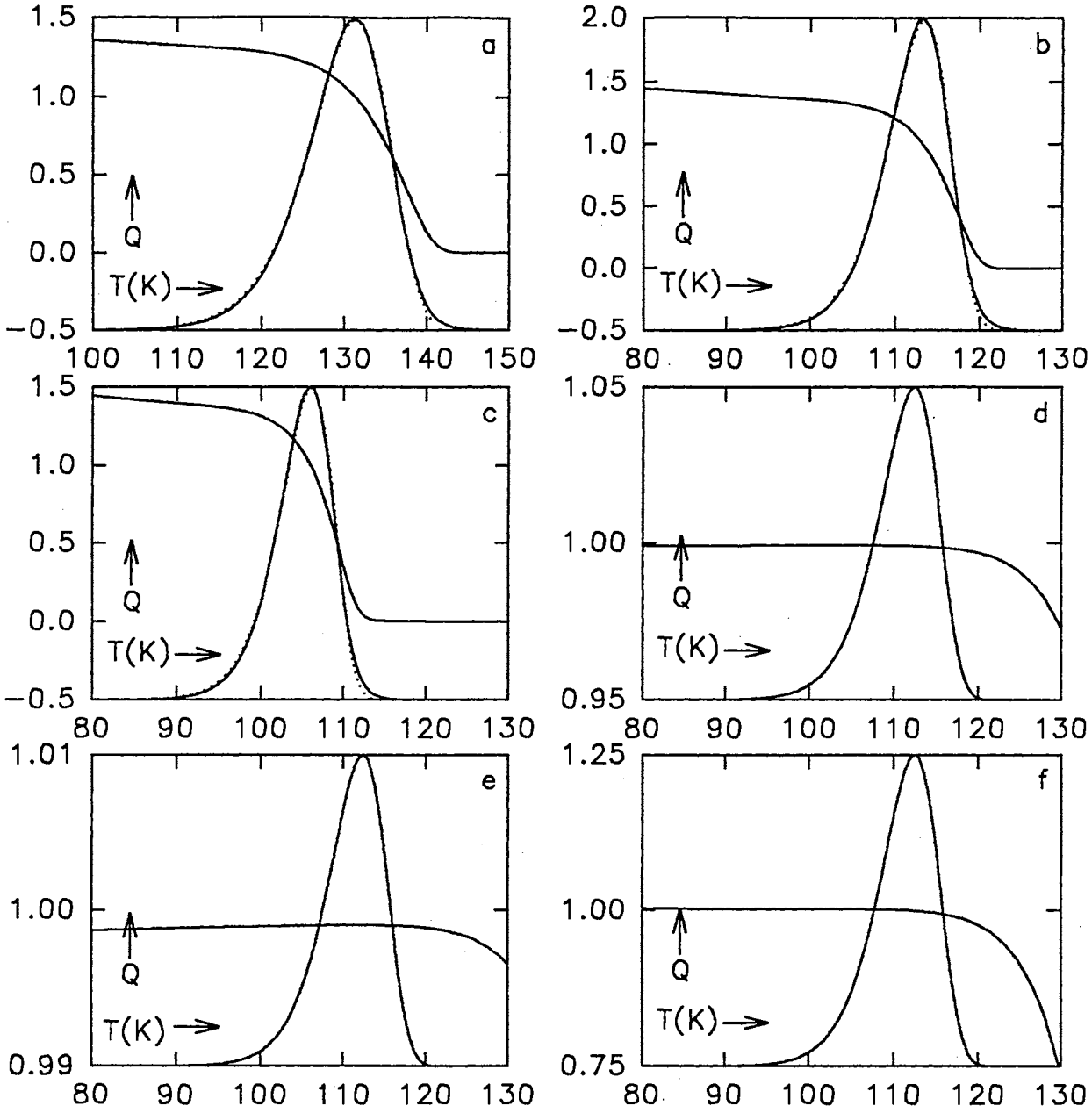

Figure 5. TSC curves generated using Runge–Kutta method. Solid line represent RK data, dotted line represent best fit to RW expression. Solid line is also used to represent Q–function. RK data is normalized, no scale is shown. Scale shown is for Q–function; Parameter values used in each data set are: E=0.3eV, b=d=3/2 and β=5K/min. Variable parameters include:(a) N=10^9, H=10^{12}, C=1.6$\cdot$ 10^{-17}, D=10^{-15}; (b) N=10^9, H=10^{12}, C=1.6$\cdot$ 10^{-15}, D=10^{-15}; (c) N=10^9, H=10^{12}, C=1.6$\cdot$ 10^{-14}, D=10^{-15}; (d) N=10^{10}, H=10^{13}, C=1.6$\cdot$ 10^{-15}, D=10^{-13}; (e) N=10^{11}, H=10^{14}, C=1.6$\cdot$ 10^{-15}, D=10^{-13} and (f) N = 10^{11}, H=10^{12}, C=1.6$\cdot$ 10^{-15}, D=10^{-13}. N and H are in units of m^{-3} and C and D are in units of $m^2K^{3/2}$ (for d=3/2). See Table I for fitted parameters.

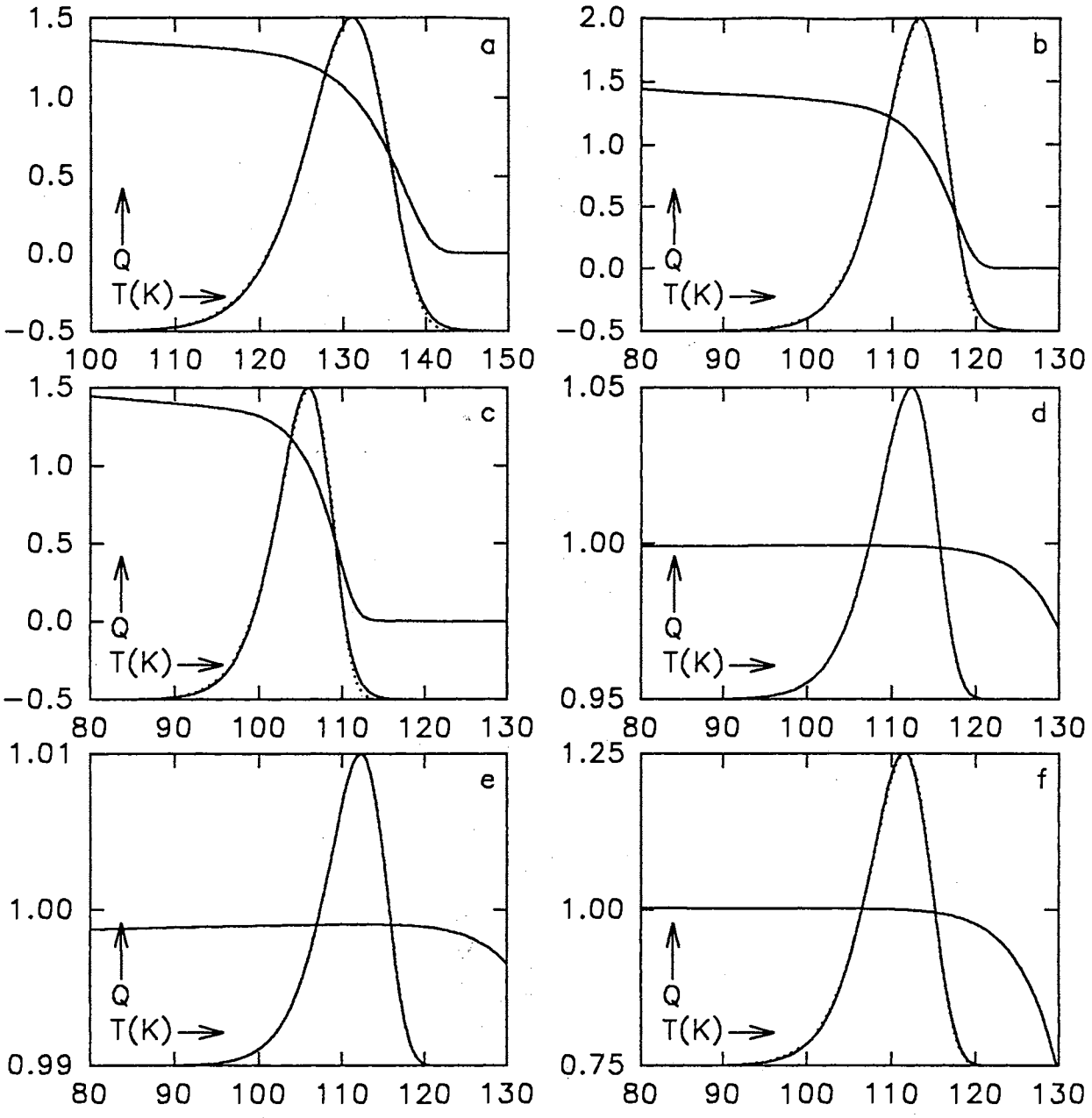

Figure 6. TL curves generated using Runge–Kutta method. Solid line represent RK data, dotted line represent best fit to RW expression. Solid line is also used to represent Q–function. RK data is normalized, no scale is shown. Scale shown is for Q–function; Parameter values used in each data set are: E=0.3eV, b=d=3/2 and β=5K/min. Variable parameters include:(a) N=10^9, H=10^{12}, C=1.6$\cdot$ 10^{-17}, D=10^{-15}; (b) N=10^9, H=10^{12}, C=1.6$\cdot$ 10^{-15}, D=10^{-15}; (c) N=10^9, H=10^{12}, C=1.6$\cdot$ 10^{-14}, D=10^{-15}; (d) N=10^{10}, H=10^{13}, C=1.6$\cdot$ 10^{-15}, D=10^{-13}; (e) N=10^{11}, H=10^{14}, C=1.6$\cdot$ 10^{-15}, D=10^{-13} and (f) N = 10^{11}, H=10^{12}, C=1.6$\cdot$ 10^{-15}, D=10^{-13}. N and H are in units of m^{-3} and C and D are in units of $m^2K^{3/2}$ (for d=3/2). See Table I for fitted parameters.

that if we had no prior knowledge of E we would write $E = 0.310 \pm 0.008$eV, thus the uncertainty is 0.016eV which represents only a 5% error.

The values given in Table I reveal that, as mentioned earlier, fitting to TL data results, in most cases, parameter values which are closer to the actual values. The primary reason for this improvement is that the Randall Wilkins equations assumes that τ is a constant. Since there is only one recombination pathway, $\tau = \tau_r$, thus $\tau/\tau_r = 1$ and TL is completely independent of the temperature dependence of τ. TSC, on the other hand, is directly proportional to τ, thus any temperature dependence in τ will directly affect the quality of the fit. As mentioned in a previous section and other reports[31,32], large concentrations of thermally disconnected traps reduce the temperature dependence of τ thus increasing the validity of the Randall Wilkins expression for TSC. In most cases, however, one expects better result when fitting to TL rather than TSC.

Although a wide range of parameter space was covered in these calculations, the extent of this range was somewhat limited by extremely long computation times. As the values of N and H were increased from 10^9 and 10^{12} to 10^{12} and 10^{14} the computation times increased from a range of 10–600sec to a range of 40–14,000sec. As attempts were made to further increase the parameters to the range of 10^{18}, computations ran for several days generating only a few of the approximately one thousand data points required for a data set. The reason for this drastic increase in computation time has not yet been explained.

In order to compare the results discussed above to the generalized expression it was necessary to numerically solve the integrals in equations (61) through (64). Since the inner integral is of the same form as the integral of equation (14), once again Keating's approximation was employed. For the outer integral it was necessary to use an adaptive Simpson's algorithm[38]. In order to save computation time when calculating the value at some temperature T_i, the integral was only evaluated from T_{i-1} to T_i and added to the previously saved value of the integral from T_0 to T_{i-1}.

Since computation times from several minutes to a few hours are common when calculating the generalized expression, it was not practical to use the generalized expression as a fitting equation. In order to perform comparisons, both the RW expression and the generalized expression were calculated using exactly the same parameter values which were used in the RK calculations. Fig. 7 shows overlay plots of TSC evaluated by each of the three methods. The RK plots are the same as those shown in Fig. 5. Notice that the RW curve for data sets (a), (b), (c) and (f) do not match the RK curves whereas for sets (d) and (e) they do match quite well (compare to fitting results of Fig. 5). The curves for the generalized solution, however, are in good agreement with every one of the RK curves except for set (f) in which the requirement $H \gg N$ is not well satisfied. It was found that the generalized solution was in excellent agreement with the RK solution for all parameter ranges tested, provided that the assumptions stated on page 28 were not violated.

Similar observations to those stated above are made for the TL curves shown in Fig. 8. For sets (a) through (e), the results are much the same as for TSC. For set (f), however, a significant improvement in the agreement between RK and the generalized solution is observed. Once again, this is attributed to the fact that TL does not depend on the temperature dependence of τ. An additional observation is made here; although the generalized solution is derived assuming that $H \gg N$, this condition does not appear to be as strict for TL as for TSC.

Having confidence in the integrity of the generalized solution, the validity of the RW expression may be investigated over a wider range of parameter space. By comparing the RW expression to the solutions of the generalized expression the lengthy computation time of RK is avoided. The testing involved calculating TSC curves using both the RW and the generalized expressions over a wide range of parameters. After normalizing each data set the χ^2 value between the two curves was calculated and a three–dimensional plots was constructed in order to easily determine ranges of 'good' and 'poor' agreement. The 3–D plots are shown in figures 9 and 10. In each of these figures we observe parameter ranges for which

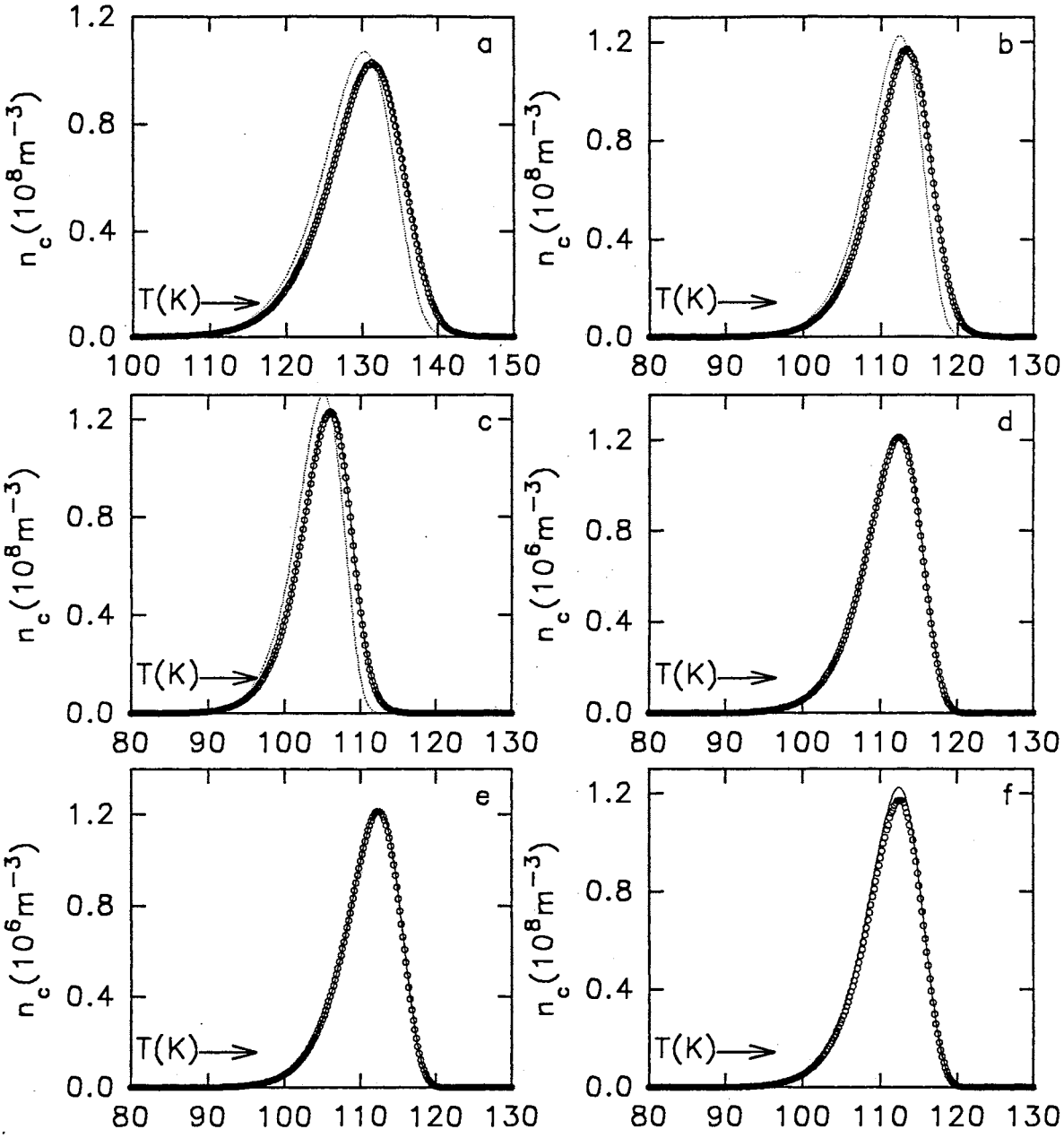

Figure 7. TSC curves generated using Runge-Kutta method. Open circles represent RK data, solid and dotted lines represent generalized and RW expressions respectively. Parameter values used in each data set are: E=0.3eV, b=d=3/2 and β=5K/min. Variable parameters include:(a) N=10^9, H=10^{12}, C=1.6$\cdot$ 10^{-17}, D=10^{-15}; (b) N=10^9, H=10^{12}, C=1.6$\cdot$ 10^{-15}, D=10^{-15}; (c) N=10^9, H=10^{12}, C=1.6$\cdot$ 10^{-14}, D=10^{-15}; (d) N=10^{10}, H=10^{13}, C=1.6$\cdot$ 10^{-15}, D=10^{-13}; (e) N=10^{11}, H=10^{14}, C=1.6$\cdot$ 10^{-15}, D=10^{-13} and (f) N = 10^{11}, H=10^{12}, C=1.6$\cdot$ 10^{-15}, D=10^{-13}. N and H are in units of m^{-3} and C and D are in units of $m^2K^{3/2}$ (for d=3/2).

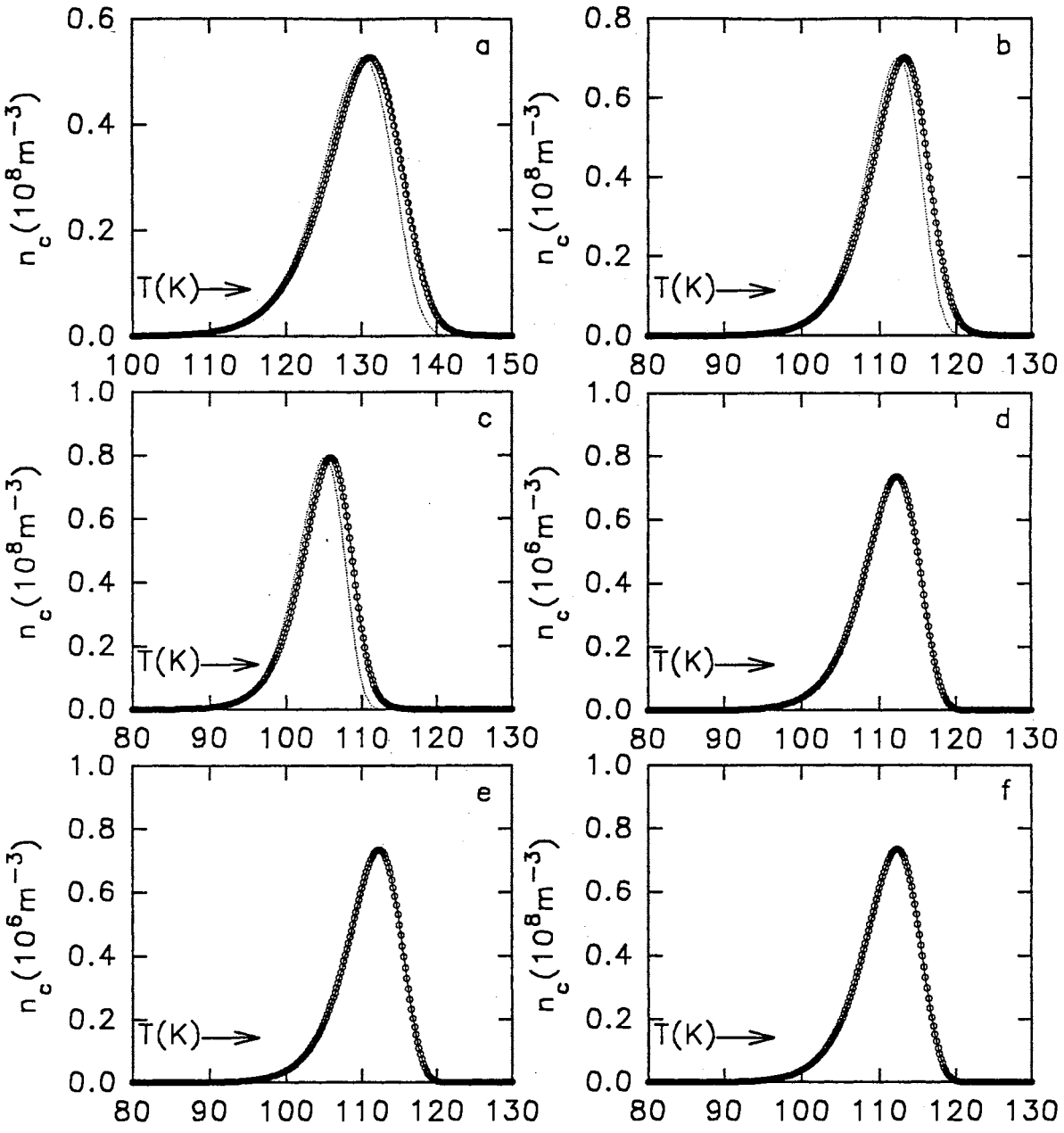

Figure 8. TL curves generated using Runge–Kutta method. Open circles represent RK data, solid and dotted lines represent generalized and RW expressions respectively. Parameter values used in each data set are: E=0.3eV, b=d=3/2 and β=5K/min. Variable parameters include:(a) N=10^9, H=10^{12}, C=1.6$\cdot$ 10^{-17}, D=10^{-15}; (b) N=10^9, H=10^{12}, C=1.6$\cdot$ 10^{-15}, D=10^{-15}; (c) N=10^9, H=10^{12}, C=1.6$\cdot$ 10^{-14}, D=10^{-15}; (d) N=10^{10}, H=10^{13}, C=1.6$\cdot$ 10^{-15}, D=10^{-13}; (e) N=10^{11}, H=10^{14}, C=1.6$\cdot$ 10^{-15}, D=10^{-13} and (f) N = 10^{11}, H=10^{12}, C=1.6$\cdot$ 10^{-15}, D=10^{-13}. N and H are in units of m^{-3} and C and D are in units of $m^2K^{3/2}$ (for d=3/2).

χ^2 is independent of parameter changes and regions in which χ^2 changes rapidly. Notice that the χ^2 value corresponding to Fig. 7(a) is indicated on the surface plot in Fig. 9. This indicator is intended to provide a reference point so that the reader might visualize the quality of fit based on the value of χ^2.

We may conclude from these calculations that the Randall Wilkins expression, while adequate over certain parameter ranges, should be questioned when used for fitting or for modeling over a wide range of parameters. The generalized expression, on the other hand, appears to accurately describe the kinetics of the system under study, over a very wide range of parameters. The best solution, of course, is one in which we are not required to make assumptions or approximations, namely Runge–Kutta. As discussed earlier, however, concerns regarding computation time often forces us to find alternative solutions. Fortunately, in this case, the generalized solution provides us with the alternative solution.

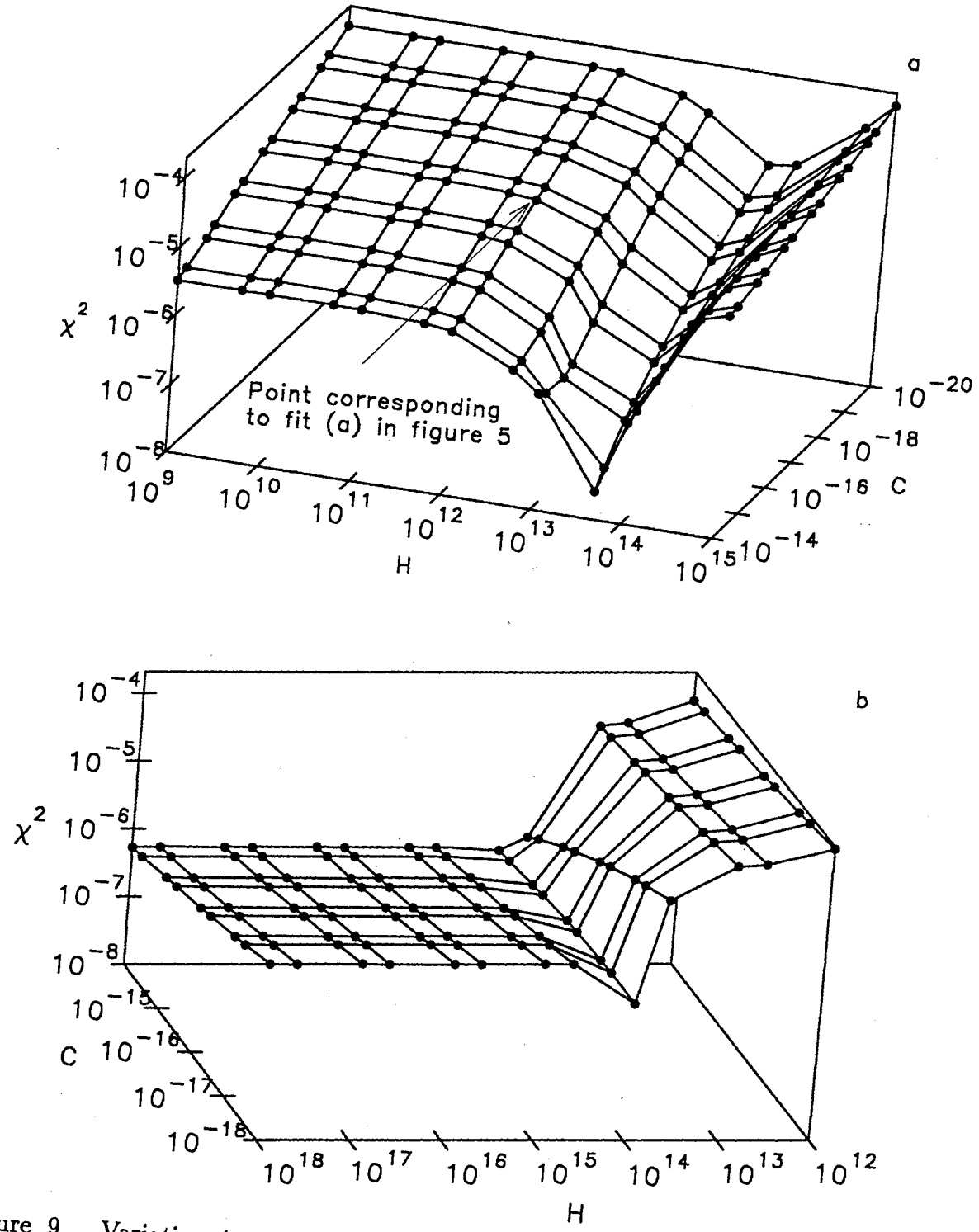

Figure 9. Variation in the χ^2 difference between the Randall Wilkins and generalized expressions as a function of C and H. Parameter values: E=0.3eV and β=5K/min. Additional parameters: (a) $b = d = 3/2, D = 10^{-15}$; (b) $b = d = 2, D = 10^{-13}$.

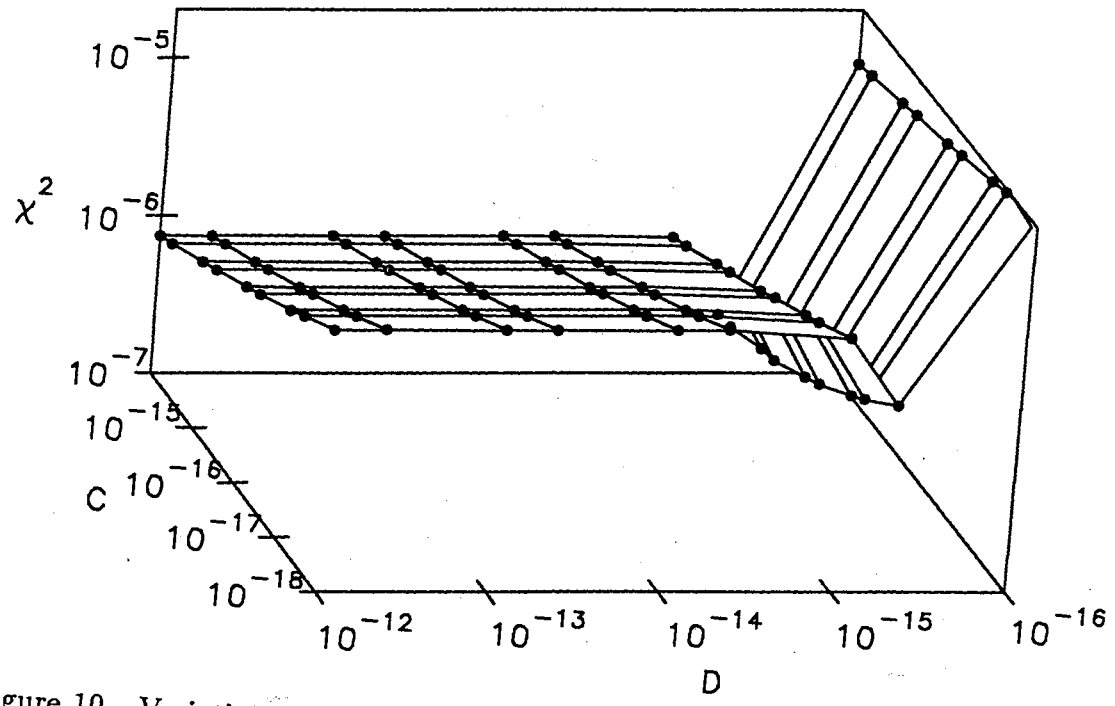

Figure 10. Variation in the χ^2 difference between the Randall Wilkins and generalized expressions as a function of C and D. Parameter values: $E = 0.3eV, b = d = 3/2, H = 10^{15} and \beta = 5\text{K/min}$.

TABLE I.

PARAMETERS OBTAINED FROM FITTING TO RUNGE–KUTTA TSC DATA

Set	Source	χ^2	C	E	b
	actual	***	$1.60{\cdot}10^{-17}$	0.300	1.50
	fit–1(TSC)	0.0155	$6.72{\cdot}10^{-15}$	0.309	2.59
(a)	fit–2(TSC)	0.0156	$6.31{\cdot}10^{-16}$	0.305	2.22
	fit–1(TL)	0.0118	$1.27{\cdot}10^{-15}$	0.302	2.42
	fit–2(TL)	0.0120	$3.21{\cdot}10^{-16}$	0.300	2.18
	actual	***	$1.60{\cdot}10^{-15}$	0.300	1.50
	fit–1(TSC)	0.0183	$1.17{\cdot}10^{-9}$	0.318	4.00
(b)	fit–2(TSC)	0.0193	$6.14{\cdot}10^{-14}$	0.302	2.31
	fit–1(TL)	0.0149	$5.89{\cdot}10^{-10}$	0.313	4.00
	fit–2(TL)	0.0156	$3.46{\cdot}10^{-14}$	0.297	2.29
	actual	***	$1.60{\cdot}10^{-14}$	0.300	1.50
	fit–1(TSC)	0.0224	$4.69{\cdot}10^{-15}$	0.291	1.52
(c)	fit–2(TSC)	0.0224	$6.92{\cdot}10^{-13}$	0.299	2.41
	fit–1(TL)	0.0181	$1.00{\cdot}10^{-9}$	0.307	3.78
	fit–2(TL)	0.0187	$4.00{\cdot}10^{-13}$	0.295	2.39
	actual	***	$1.60{\cdot}10^{-15}$	0.300	1.50
	fit–1(TSC)	$1.32{\cdot}10^{-4}$	$6.97{\cdot}10^{-17}$	0.299	0.85
(d)	fit–2(TSC)	$8.85{\cdot}10^{-5}$	$4.78{\cdot}10^{-14}$	0.310	2.00
	fit–1(TL)	$8.33{\cdot}10^{-9}$	$9.76{\cdot}10^{-16}$	0.299	1.41
	fit–2(TL)	$8.33{\cdot}10^{-9}$	$9.76{\cdot}10^{-16}$	0.299	1.41
	actual	***	$1.60{\cdot}10^{-15}$	0.300	1.50
	fit–1(TSC)	$1.32{\cdot}10^{-4}$	$6.98{\cdot}10^{-17}$	0.299	0.85
(e)	fit–2(TSC)	$8.85{\cdot}10^{-5}$	$4.78{\cdot}10^{-14}$	0.310	2.00
	fit–1(TL)	$1.23{\cdot}10^{-5}$	$4.42{\cdot}10^{-16}$	0.298	1.27
	fit–2(TL)	$1.24{\cdot}10^{-5}$	$1.40{\cdot}10^{-16}$	0.300	1.47
	actual	***	$1.60{\cdot}10^{-15}$	0.300	1.50
	fit–1(TSC)	$2.24{\cdot}10^{-5}$	$5.41{\cdot}10^{-17}$	0.302	0.74
(f)	fit–2(TSC)	$1.62{\cdot}10^{-4}$	$4.05{\cdot}10^{-14}$	0.309	1.50
	fit–1(TL)	0.0073	$5.26{\cdot}10^{-10}$	0.307	4.00
	fit–2(TL)	0.0080	$2.53{\cdot}10^{-14}$	0.291	2.25

CHAPTER III

EXPERIMENTAL RESULTS FOR HIGH RESISTIVITY SAMPLES

Sample Preparation

The experimental results discussed in this chapter were obtained for high resistivity, undoped ZnSe single crystals grown by the Bridgman and SPVT techniques. A description of these growth techniques is available elsewhere[16]. The samples were all $1/4\mu m$ polished. The average size of the polished samples was $5mm \times 5mm \times 1mm$. Some of the samples used in this study were etched in either 14 normal NaOH at 90℃ or a 3 percent bromine methanol solution at room temperature. These etchants, however, were found not to affect either the TSC or the TL results.

Samples to be used for TSC were fitted with electrodes in order to provide electrical contacts. The electrodes were fabricated by placing the sample in a vacuum chamber and evaporating gold onto the sample from a heated tungsten filament. The electrode on the rear face of the sample (the side facing the sample holder) was simply a thick gold film. The electrode on the front (illuminated) face of the sample, however, was not so simple. In order to allow for illumination the front electrode was fabricated in one of two ways: (1) a mask is used to prevent gold from covering the center of the sample face. This provides us with a window through which we can illuminate the sample; (2) a semi-transparent gold film was evaporated in order to allow illumination through the electrode. One must use care so as not to make the film so thin that it is non-conducting. This problem is easily overcome by placing a glass microscope slide beside the sample during evaporation. By measuring the resistance across the surface of the glass slide

and continuing evaporation until the glass slide begins to conduct, one ensures a conducting electrode. Additionally, one of the melt grown samples used in this work was fitted with ultrasonically soldered indium electrodes, on which the front face contained a 3mm illumination window.

Experimental Procedures and Apparatus

All TSC, TL and photoconductivity data were obtained using a continuous flow cryostat (Oxford CF–1204) using liquid nitrogen as the coolant. A detailed cross section of the cryostat is shown in Fig. 11(a). This type of cryostat is preferred to a closed system since the latter requires a compressor piston to be mounted inside the cryostat. Such a mechanism can generate much mechanical vibration which would be detrimental to the sensitive nature of TSC measurements.

Samples were mounted on a copper block at the end of a sample holder which was fitted into the cryostat. When performing electrical measurements great care was taken to ensure adequate thermal contact to the copper block while also providing electrical insulation. Since simultaneous measurements of TSC and TL were often made, precautions were taken to ensure that the insulating materials used did not themselves emit TL in the temperature range of interest. Additionally, the sample holder was designed so that the coaxial and triaxial cables, which connected to the sample, were enclosed in 3/16 inch metal tubing to provide additional shielding. This degree of shielding was found to be necessary when measuring the small currents associated with TSC. The sample holder and the details of sample mounting are shown in Fig. 11(b). The sample holder was also fitted with a pair of Watlow 40 watt DC cartridge heaters and a high precision rhodium–iron resistive temperature sensor. These elements, in conjunction with an Oxford ITC–4 temperature controller, enabled us to either maintain a constant temperature or provide a linear heating profile with a temperature accuracy of 0.1K.

After mounting a sample, the holder is inserted into the sample chamber (see Fig. 11(a)) which is then evacuated to remove moisture and other contaminants. After allowing several hours for outgassing, the pressure in the sample chamber is

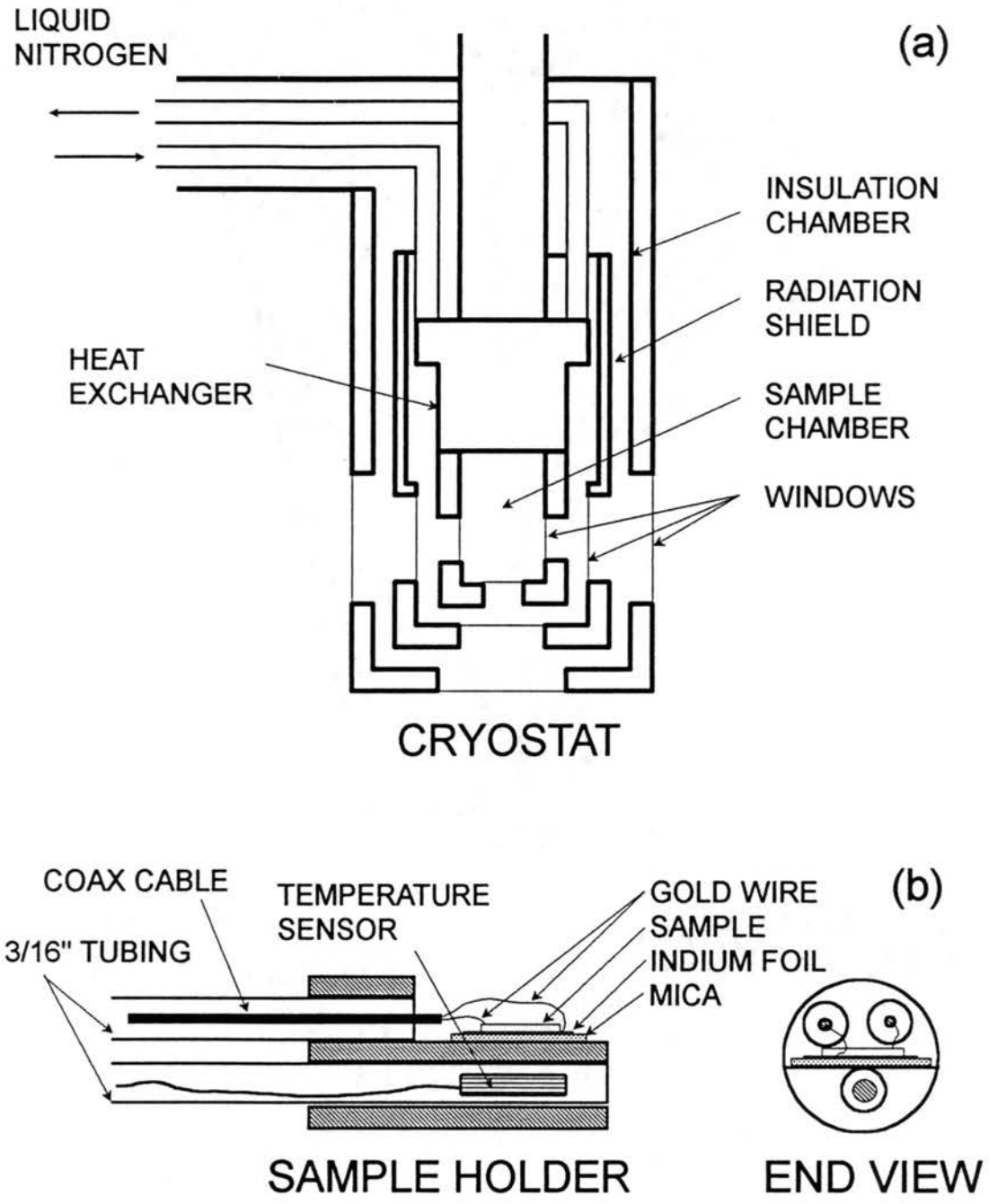

Figure 11. Figure (a) shows the cross sectional details of the Oxford CF–1204 cryostat which was used in this work. Figure (b) shows the details of the sample holder. The metal tubes which enclose the coax. and triax. cables provide both mechanical stability and shielding from electrical noise. The combination of mica and indium foil provides good thermal contact as well as electrical insulation.

raised to approximately 500 torr by introducing high purity helium gas. This gas provides the heat exchange between the sample and holder and the cooling coils surrounding the sample chamber.

Once the sample chamber has been flooded with helium gas, the TSC/TL experiment proceeds as follows: (1) the sample is cooled, in the dark, to low temperature (usually 80K); (2) an electronic shutter is opened to allow illumination with either white light or monochromatic light (depending on the nature of the experiment); (3) after closing the illumination shutter, the shutter protecting the PMT is opened and the electrometer is activated; (4) the sample is heated, in the dark, to high temperature (usually 300K) using a heating profile which is linear in time. During both the cooling and heating cycles, the same bias voltage is maintained across the sample in order to avoid measuring current transients due to polarization or depolarization of dipolar defects [39]. For various experimental considerations, the bias voltage maintained during illumination may be different from the bias during heating and cooling (see pages 55 and 65). In all cases, the sign of the bias voltage refers to the polarity of the front or illuminated face of the sample.

TSC data were measured with a Keithley 617 electrometer/programmable power supply thus allowing for a single instrument to provide the power source and measure the resulting current. Using this type of arrangement has allowed the measurement of currents as low as 0.01pA with an acceptable signal–to–noise ratio.

TL data were obtained in the following ways: first, emission from the sample was focused on the detector of an EMI model 9635QB photomultiplier tube (PMT), the output of which was connected to a discriminator in order to convert the current output of the PMT to digital pulses suitable for input to a photon counter (HP model 5334B). From this apparatus curves of TL intensity versus temperature were obtained ('standard' TL); second, the emission was focused on the entrance of a SPEX 1681 spectrometer which had been modified to produce a one inch flat field image (i.e. a spectrograph). This image was focused onto the detector of a Quantar

Technology microchannel plate PMT. Using this arrangement it was possible to obtain either TL or PL as a function of both temperature and wavelength.

For measurements using the microchannel plate PMT the excitation source was an Ar ion laser ($\lambda = 351.1$nm). For TSC and standard TL a xenon lamp was used to excite the sample before heating. This light source was used both unfiltered and in combination with a 334nm interference filter. For measurements of photoconductivity and excitation wavelength dependent TSC and TL, a tungsten lamp was used in conjunction with a SPEX 1681 spectrograph. The xenon lamp was inappropriate for these measurements due to the sharp emission lines present in the xenon spectrum.

All experimental control was performed by an IBM PC which was interfaced to the equipment via IEEE–488 or RS–232 as shown in Fig. 12. In addition to the equipment described above the computer also: (1) opened and closed electronic shutters, to provide illumination and to expose the PMT to the sample during heating; (2) provided timing signals to start, stop and read the photon counter; (3) started and stopped preprogrammed temperature sweeps which had been stored in the temperature controller; (4) record and save all data.

Results

Upon mounting a sample an I–V characterization was performed in order to determine the ohmic or non-ohmic nature of the electrodes. Effects due to contact resistance and non linearity of I–V characteristics are somewhat unimportant in TSC measurements since we are concerned only with the transient nature of the current; the absolute magnitude is of no significance in evaluating trapping parameters. We are, however, concerned with the nature of highly blocking contacts. A highly blocking contact limits our ability to measure weak TSC signals since most of the voltage drop will appear across the contact rather than across the sample under study, thus, reducing or signal by orders of magnitude. Fortunately, all of our electrodes exhibited an acceptable degree of non-linearity, as shown in Fig. 13.

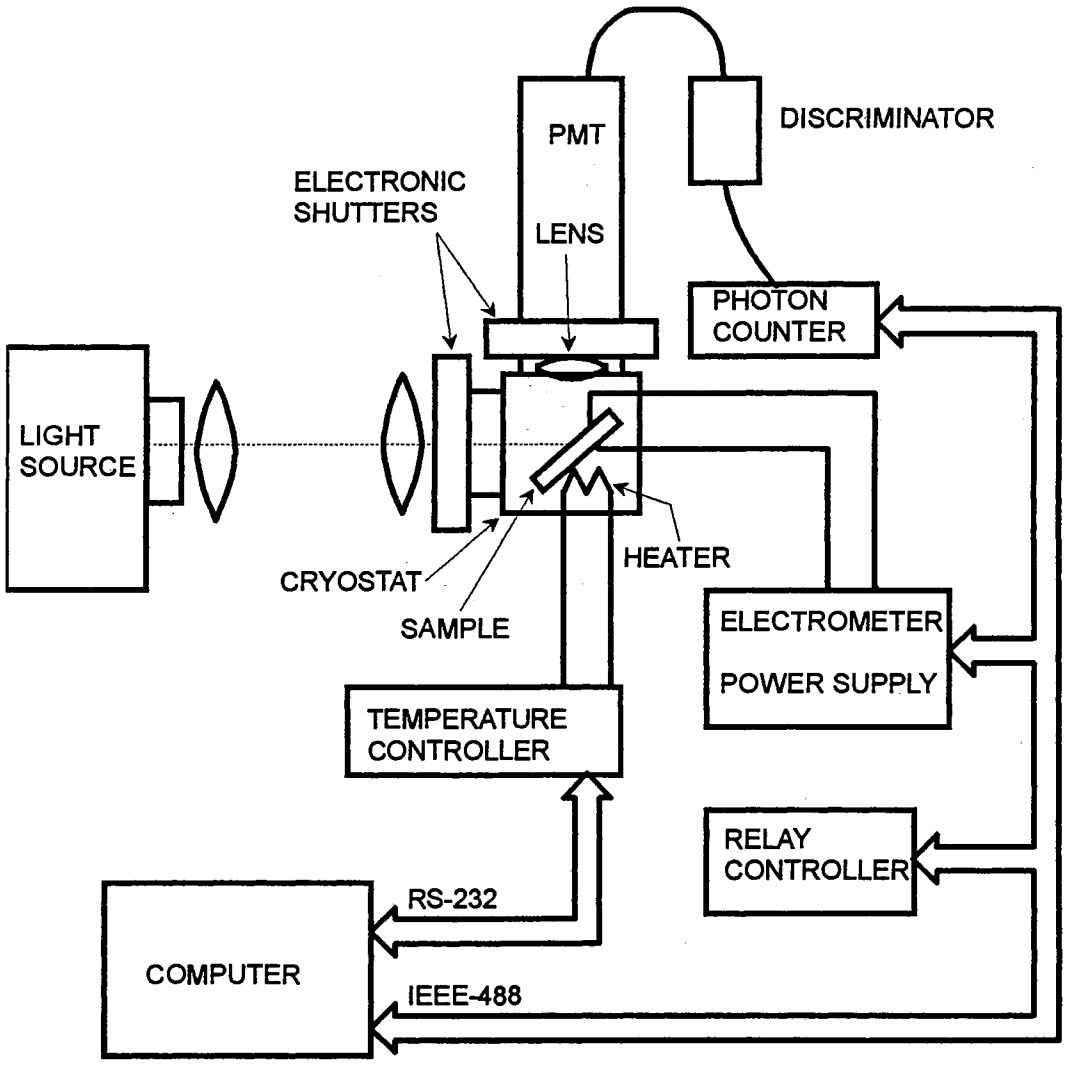

Figure 12. This figure shows the major components of the experimental apparatus used for measuring TSC and TL. Interface connections for both IEEE–488 and RS–232 are also shown.

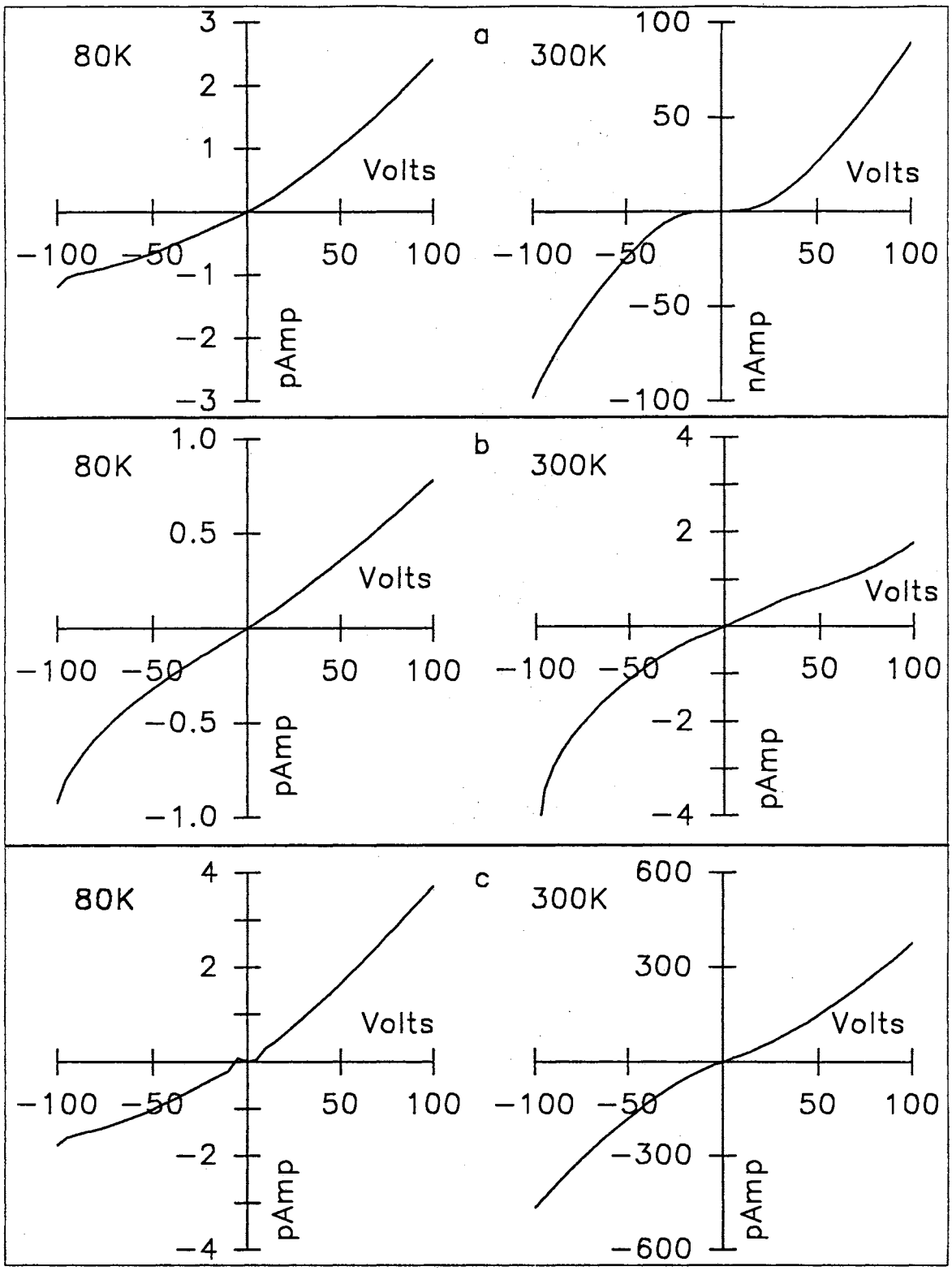

Figure 13. Electrode I–V characteristics at 80K and 300K for (a) gold on SPVT; (b) gold on MG; (c) Indium on MG.

Kinetic Order

As mentioned in chapter II, the fitting equations (Eqns. (19) and (20)) were derived on the basis of first–order kinetics, or slow retrapping (see Eqn. (9)). Before using these fitting equations, it must be determined that the observed TSC and TL are indeed first–order.

Examination of equations (19) and (20) shows that the initial trapping concentration n_0 enters into the equation only as a scaling factor. Stated more simply: varying n_0 (i.e. illumination time) does not change the shape or position of the peak. In the case of non–first–order kinetics (Eqns. (32) and (34)) we see that the dependence upon n_0 is nonlinear and varying n_0 causes the peak position and shape to change. Non–first–order peaks also exhibit a much higher degree of symmetry than first–order peaks[40]. Thus, first–order kinetics can be verified experimentally by taking TL and TSC measurements after each of several illumination times. If the peaks are first–order they should grow without shifting in temperature or changing shape. One must use a certain amount of caution in the case of overlapping peaks since small shifts may be observed if two or more overlapping, first–order peaks grow at different rates. From the data shown in Fig. 14 it is apparent that all TL and TSC peaks are first–order. It should be pointed out at this time that no TL was observed from the SPVT samples.

Curve Fitting

Having confirmed that the TSC and TL peaks are described by first–order kinetics curve fitting was performed in order to determine the trapping parameters of each peak. The data were fitted to a set of overlapping peaks defined by equations (19) and (20) as outlined in appendix B. In this manner it was possible to obtain trapping parameters (E, B and a) for the SPVT TSC peaks and the MG TL peaks. Once obtained these values were used to calculate the capture cross–section (S) and frequency factor (s) at the maximum of each peak. It was found that the TSC spectra for SPVT samples are composed of eight overlapping peaks

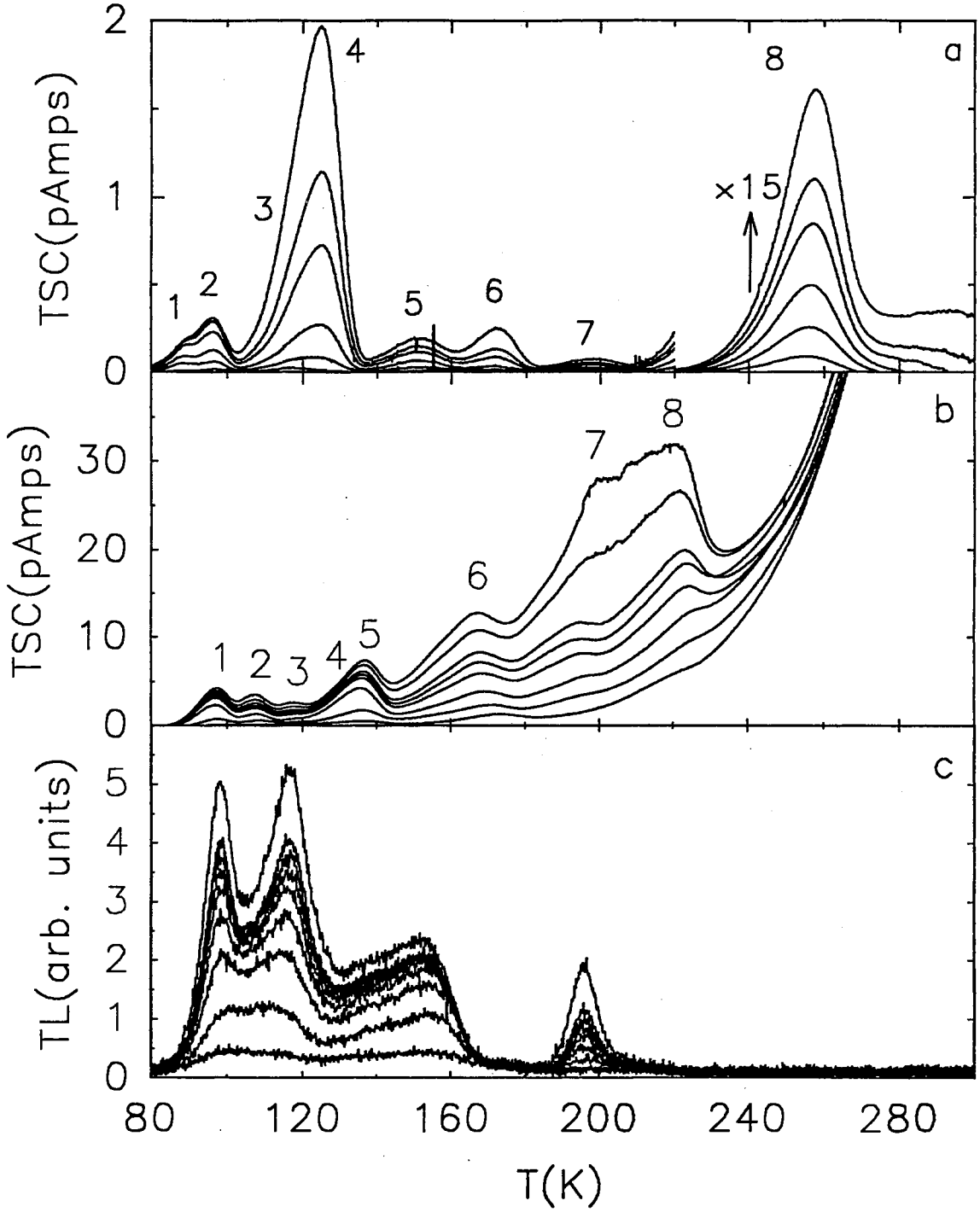

Figure 14. Variable illumination data for (a) SPVT (TSC); (b) MG (TSC); (c) MG (TL). In each case we see that the peak positions do not change with increasing illumination time. These results indicate first–order kinetics.

with activation energies (E) between 0.18 and 0.71eV, as summarized in Table II. The TL spectrum for the MG samples is composed of six peaks with activation energies between 0.14 and 0.73eV (Table III). These tables also show the values of the capture cross section S and the frequency factor s evaluated at the peak maximum T_m. The deconvoluted spectra for SPVT TSC and MG TL are shown in Fig. 15a and b, respectively.

The TL peak near 195K (MG sample), although it appears to be a single peak, proved to be very difficult to fit (see Fig. 15b). The shape of the peak appears to be too symmetrical for a first–order peak. Variable illumination experiments, however, indicate that it follows first–order behavior. Attempts were made to fit this peak to a composite of first–order peaks (Eqn. (20), to second–order peaks and by assuming a gaussian distribution of trap levels. All of these attempts have failed to yield a satisfactory fit. The fit shown in Fig. 15b is the best fit to a single peak. A possible cause for the inability to fit this TL peak to the standard equations is that the system has deviated from quasi–equilibrium. If the system is not in quasi–equilibrium then the fitting equations (Eqns. (19) and (20)) are no longer valid. This peak will be further analyzed in a later section (see page 71).

TABLE II.

FITTING PARAMETERS OBTAINED WITH A FOUR PARAMETER FIT TO THE TSC DATA FROM SPVT ZNSE.

	Trapping Parameters					
Peak No.	T_m(K)	E(eV)	B(s^{-1})	a	s(s^{-1})	S(cm^2)
1	87.5	0.20	6.6×10^{8}	1.3	1.4×10^{10}	3.0×10^{-16}
2	95.5	0.20	3.3×10^{10}	2.8	9.9×10^{8}	1.8×10^{-17}
3	121.3	0.18	1.1×10^{9}	3.6	4.7×10^{5}	5.3×10^{-21}
4	126.5	0.33	2.8×10^{11}	2.0	2.3×10^{11}	2.4×10^{-15}
5	151.0	0.27	2.9×10^{8}	2.7	8.6×10^{6}	6.3×10^{-20}
6	170.8	0.40	4.2×10^{10}	2.4	6.0×10^{9}	3.5×10^{-17}
7	197.9	0.46	9.1×10^{10}	2.5	6.9×10^{9}	3.0×10^{-17}
8	256.7	0.71	2.2×10^{10}	1.3	1.0×10^{12}	2.6×10^{-15}

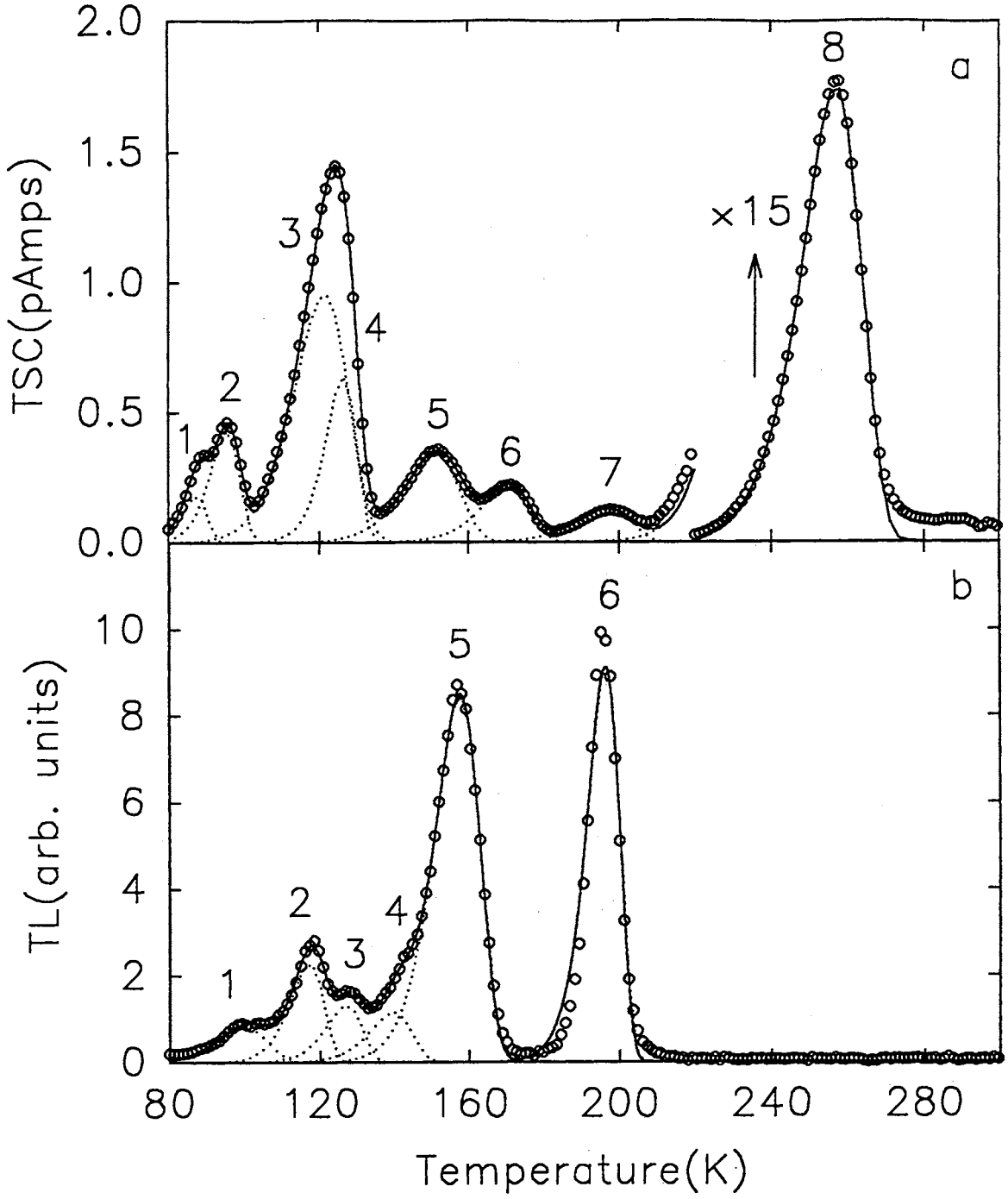

Figure 15. Deconvoluted spectra for (a) SPVT (TSC); (b) MG (TL). The symbols represent the data and the solid line represents the composite of the fitted peaks. The individual fitted peaks are represented by dotted lines (The actual data point density is 6 times greater than that shown). Experimental parameters: (a) Illuminated with 334nm filtered xenon lamp for 20min with +5v bias applied; cooled and heated with -5v bias applied. (b) Illuminated with unfiltered xenon lamp for 10s with no bias applied; cooled and heated with -5v bias applied.

The TSC curves for the MG samples are highly complex. In an attempt to resolve the individual peaks, the method of $T_m - T_{Stop}$ [41] was employed. This method involves heating to a temperature T_{stop} following illumination, returning to the illumination temperature then heating and recording data over the entire temperature range of interest. The initial heating cycle partially empties the trap levels closest to the delocalized bands. When the data is recorded the temperature of the first maximum, T_m, is noted. The experiment is repeated many times, incrementing the value of T_{stop} each time. It is expected that the value of T_m remains constant until the value of T_{stop} is high enough that the initial heating completely empties the corresponding trap level. Subsequent cycles will then have a higher T_m value. By plotting T_m versus T_{stop} a stair step type of plot is normally observed, each step corresponding to a separate peak. Close peak overlap may cause several steps to form a ramp, thus making it impossible to distinguish individual peaks. Despite using this method we were unable to deconvolute the peaks. Thus, no fitting data are provided for TSC from the MG samples.

Until now the possible temperature dependence of the product $\mu\tau$ has been ignored (see Eqn. (19)) since this temperature dependence is weak compared to the $\exp(-E/kT)$ dependence of the TL and TSC curves. In all the results presented we have assumed that $\mu\tau$ is a constant. In order to account for the possible temperature dependence it is necessary to obtain $\mu\tau$ as a function of temperature

TABLE III.

FITTING PARAMETERS OBTAINED WITH A FOUR PARAMETER FIT TO THE TL DATA FROM MG ZNSE.

Trapping Parameters						
Peak No.	T_m	E(eV)	B(s^{-1})	a	s(s^{-1})	S(cm^2)
1	100.0	0.14	1.1×10^{8}	3.6	8.1×10^{4}	1.5×10^{-20}
2	117.1	0.26	4.4×10^{9}	2.1	3.2×10^{9}	4.2×10^{-16}
3	127.0	0.29	6.9×10^{9}	2.1	3.7×10^{9}	4.1×10^{-16}
4	139.6	0.30	3.9×10^{9}	2.3	7.2×10^{8}	6.7×10^{-17}
5	157.6	0.35	5.5×10^{9}	2.2	2.0×10^{9}	1.4×10^{-16}
6	196.4	0.73	2.5×10^{12}	0	9.6×10^{16}	4.5×10^{-9}

(to within a scaling constant), divide the TSC data by this function and then fit the resulting 'corrected' spectra to the standard first–order equation. In order to obtain the temperature dependence of $\mu\tau$ one may measure the photocurrent[42] which is given by

$$I_{pc} = e\phi\mu\tau\frac{V}{L^2} \tag{77}$$

where e is the electron charge, ϕ is the photon flux per unit time, V is the applied bias and L is the sample thickness. Since all of these parameters are constants they may be ignored so that $I_{pc} \propto \mu\tau$. By measuring I_{pc} as a function of temperature we obtain the temperature dependence of the product $\mu\tau$ which may be used to correct TSC. Since the temperature dependence of $\mu\tau$ was small, applying this technique to our samples made little or no difference in the fitting parameters.

Dependence of TSC and TL Upon Excitation Bias

An attempt to determine the sign of the charge carriers released during TSC was made using the method of Scharager *et al.*[43]. To apply this technique one monitors the growth of TSC peaks as a function of illumination time for both positive and negative excitation biases. The excitation source must be monochromatic using energies greater than the band gap in order to ensure absorption of photons at the sample surface. A xenon lamp and a 334nm interference filter were used for this purpose. According to the discussion of Scharager *et al.*[43], by applying a negative excitation bias, one expects the free electrons generated at the surface to be pushed into the sample whereas holes will be quickly removed through the front face electrode. Thus, peaks due to the thermal release of electrons from bulk states would be expected to grow more rapidly than peaks due to the release of holes. Similarly, when applying a positive excitation bias, peaks due to hole release should grow more rapidly than those due to electron release. Peaks due to surface states, however, may not be affected by changing the excitation bias. In the application of this technique one must bear in mind that peak overlap and

space charge effects may influence the behavior of each peak and definite carrier assignments may be difficult. The experiments should be performed using several different combinations of positive or negative biases applied during illumination, heating and cooling. These measurements should all yield consistent results before definitive conclusions can be made.

In the case of the MG samples the results for peaks 1 through 6 were generally inconsistent and gave different results depending upon the particular combination of polarities used. As Fig. 16 shows, TSC peaks 1 through 6 initially grow more rapidly under the influence of a positive excitation bias, whereas peaks 7 and 8 grow more rapidly under the influence of a negative excitation bias. For longer illumination times, however, TSC peaks 1 through 6 grow to much greater magnitude with a negative excitation bias applied. The latter results for peaks 1-6 appears to contradict the results for shorter illumination times. This may indicate that the TSC spectrum below about 180K is a complex overlap of both hole related and electron related peaks. Analysis of peaks 7 and 8, however, consistently indicate association with electron traps. The inset in Fig. 16 shows the detailed growth of peak 1 for short illumination times. Fig. 17 shows the TSC spectrum resulting from a 20 volt excitation bias (both positive and negative). Once again the entire TSC spectrum appears to be dominated by the thermal release of electrons. These carrier assignments must be regarded as somewhat indefinite since the TSC structure changes significantly when various biasing combinations are used and the results for peaks 1-6 are quite inconsistent.

Analysis of the SPVT samples, however, consistently indicated that all the TSC peaks from this material were due to the release of holes. The growth of TSC curves for both positive and negative excitation biases is shown in Fig. 18 and, as before, the inset indicates the growth of a particular TSC peak (peak 1) with illumination time.

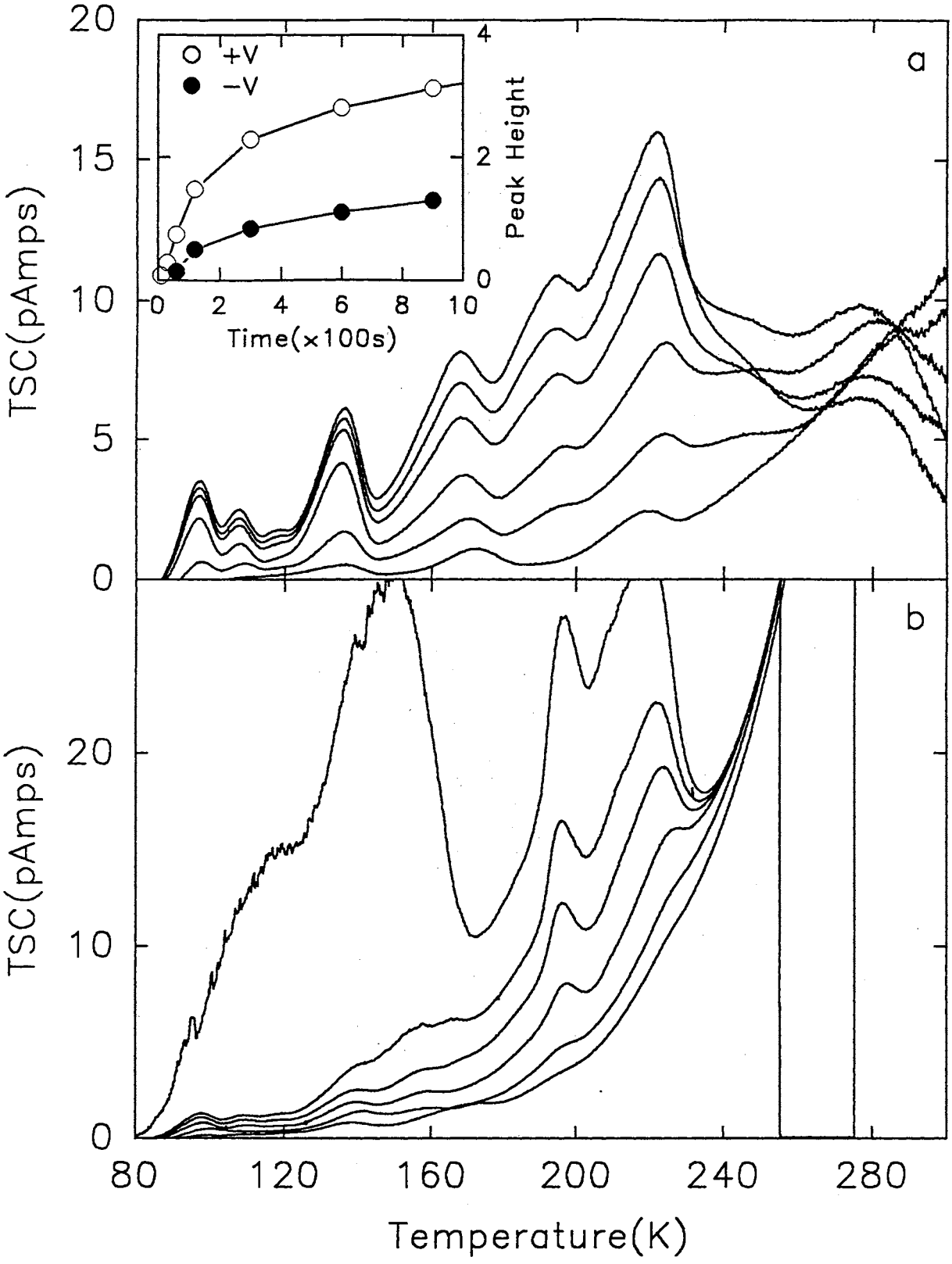

Figure 16. Growth of TSC peaks for a MG sample as a function of illumination time for both (a) positive and (b) negative bias applied during illumination. Inset shows detailed growth of peak 1.

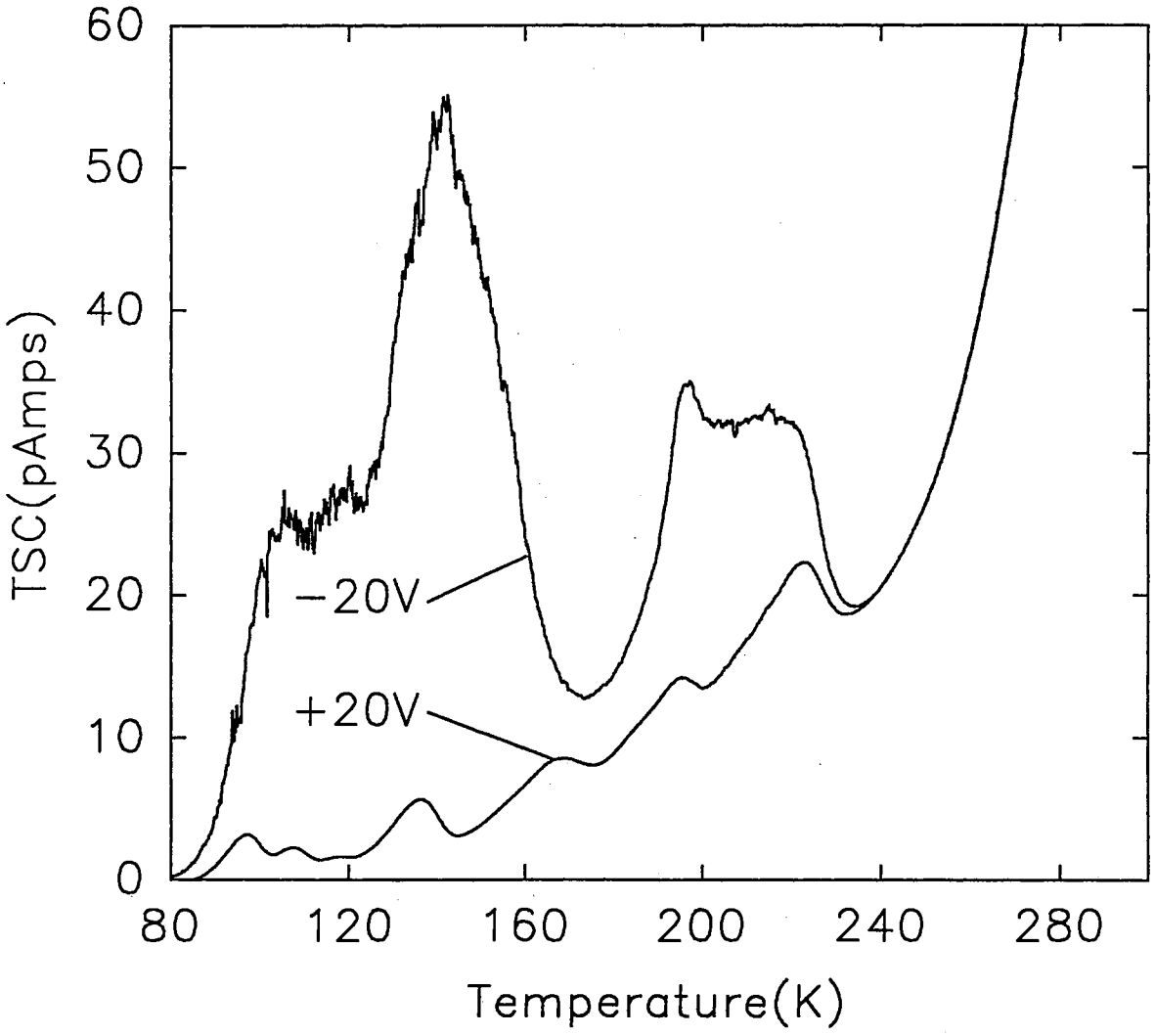

Figure 17. TSC from MG sample for both positive and negative 20v excitation bias.

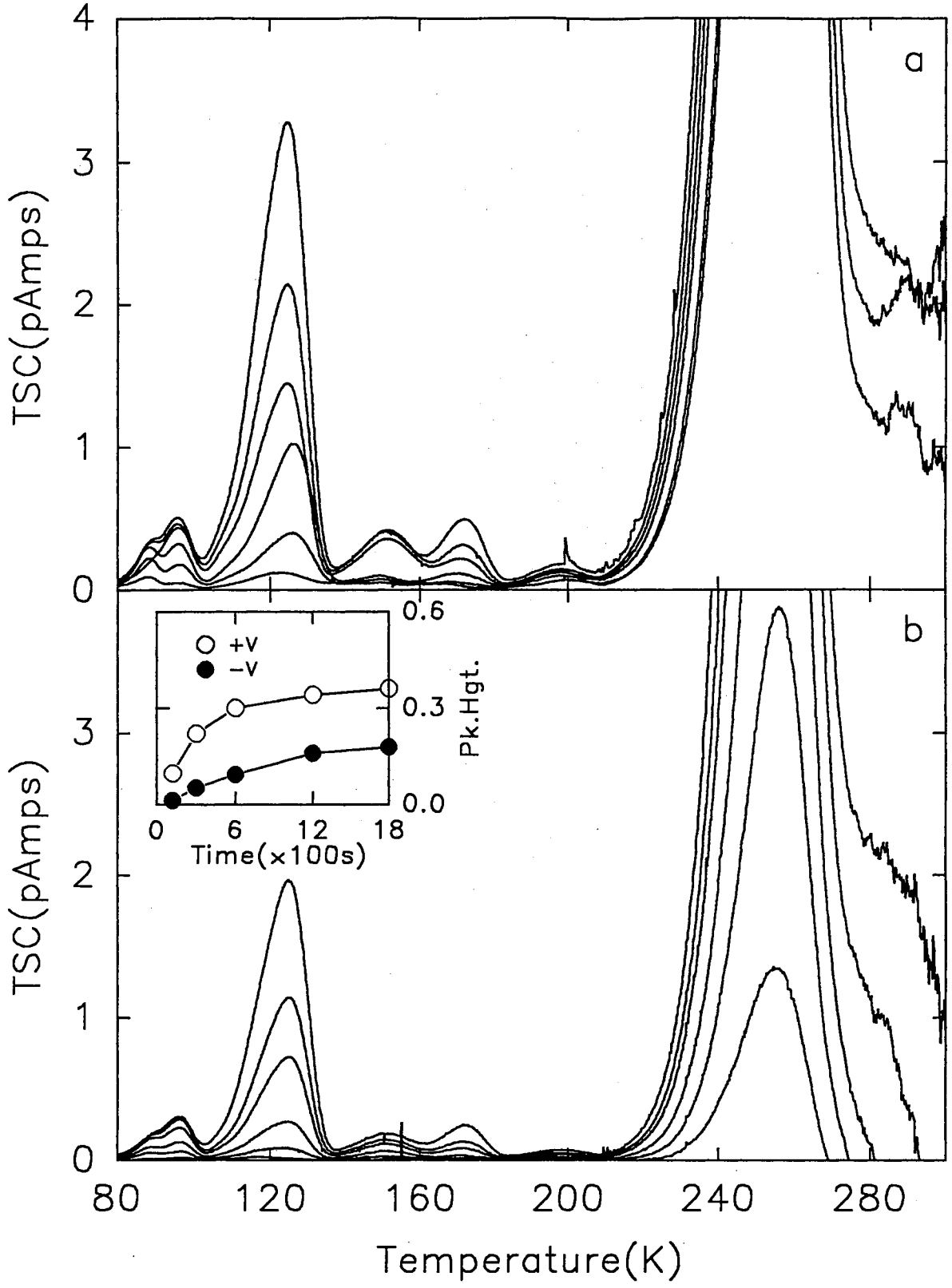

Figure 18. Growth of TSC peaks for a SPVT sample as a function of illumination time for both (a) positive and (b) negative bias applied during illumination. Inset shows detailed growth of peak 1.

TL and TSC Correlations

If the mechanism giving rise to TL involves transitions to delocalized bands, there should, in principle, be a corresponding TSC peak at, or near, the same temperature. The exact relationship between the peak positions will depend on the temperature dependence of μ and τ_r as discussed in Chap. II In contrast, a given TSC peak will not necessarily have a corresponding TL peak. For example, if the recombination processes are non–radiative, no TL peak will be observed.

In the present samples, the relative sizes of both the TSC and TL peaks are dependent upon illumination time and the biases applied during illumination and heating. The relative peak heights were also found to vary from sample to sample. This latter property was found to be especially true for the MG samples. However, it is important to note that the number and positions of the peaks were independent of all the above conditions; only the relative peak heights changed. The values determined for the trapping parameters were unaffected by the illumination time and the polarity and value of the applied biases.

In Fig. 19 simultaneously measured TSC and TL for a MG sample are compared. It is observed that all of the TL peaks have corresponding TSC peaks. From the peak near 200K we see that the TL peak appears at a slightly lower temperature than the corresponding TSC peak, in agreement with theory (see discussion on page 18).

TL and PL Emission Analysis

Of the previous studies of PL and TL emission analysis on ZnSe samples, grown by a variety of methods, most have observed two important broad emission bands. These bands occur at $\approx$ 1.97eV (red) and $\approx$2.35eV (green) and are believed to be associated with copper substitutionals (Cu_{Zn}). Copper gives rise to one of two energy levels in the band–gap, either $\approx$ 0.72eV or $\approx$ 0.35eV above the valence band, which act as recombination centers for red and green emission. With this in mind, the center at 0.72eV is referred to as the Cu_{red} center and the level at 0.35eV

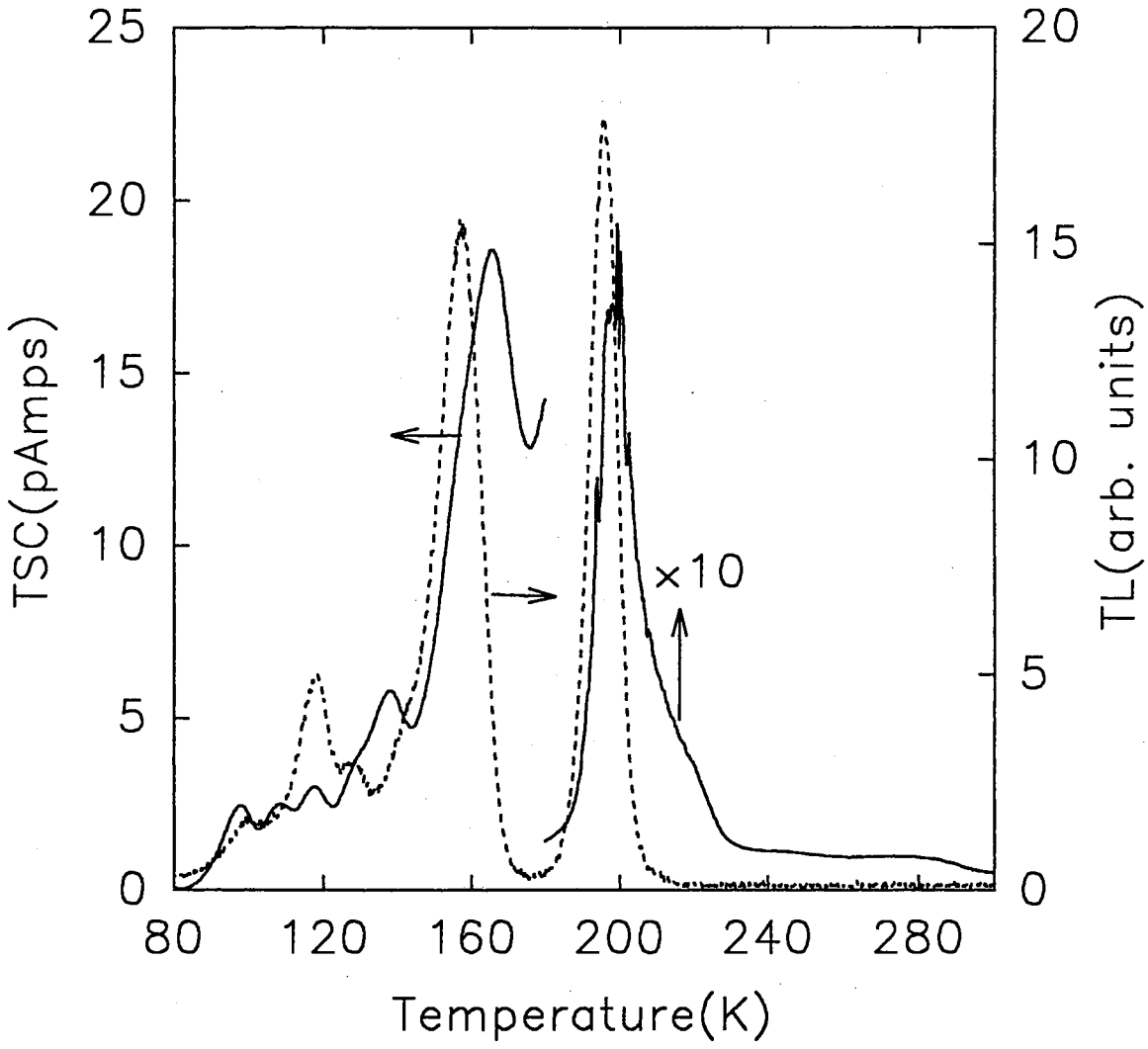

Figure 19. Overlay of TSC and TL spectra for MG sample. Note that each TL peak has a corresponding TSC peak. The TSC peak near 200K has been scaled down by a factor of 10. The sample was illuminated, with no bias applied, for 10s using an unfiltered xenon lamp. Cooling and heating were performed with -5v bias applied.

is the Cu_{green} center. The level at 0.72eV is often attributed to zinc vacancies and is referred to as the self–activated or SA center. From the measurements made in this study it is not possible to distinguish the Cu_{red} center from the SA center. For the purpose of discussion the center will be referred to as the Cu_{red} center.

The sample used for these measurements is not the same sample which was used to measure the TL curves shown in Figs. 14(c) and 19. Sample–to–sample variations in the relative peak heights have already been noted (see page 60) and this explains the difference in the relative peak heights between the two data sets. The sample used for the emission analysis was a larger sample with no electrodes so that a larger luminescent area might be observed thus resulting in a signal which was strong enough to be observed with the microchannel plate PMT. Although the relative peak heights are different, the overall TL structure is the same as that shown in Figs. 14c and 19.

The data obtained from measurements of TL versus temperature and wavelength for the MG material are shown in Fig. 20(a) and (b) where plot (b) is simply a magnification of plot (a) and viewed from a different perspective. The magnified plot shows that the low temperature peaks are present in this sample but are weaker than seen previously(see Fig. 14(c)). Study of these plots reveals that the TL signal is entirely due to red emission at $\lambda_{max} \approx$ 630nm, 1.97eV (Stringfellow and Bube [44] report this emission as well as emission at 1.95eV). We also note that the main peak near 200K does not appear to be a composite but rather a single TL peak with a broad emission band. We do not observe any green emission which has been previously reported in ZnSe [44,45]. Possible causes for the lack of green emission will be discussed in Chap. VI

From the TSC data, and from the correlation between the TSC and TL peak positions (in particular: TL peak 6 and TSC peak 7; see Fig. 19), we may argue that since the TSC peak near 200K is due to the thermal release of electrons, then the TL peak near 200K is also due to the release of electrons. Since, in Fig. 20, all the TL peaks occur at the same wavelength, they all apparently involve the same recombination process thus, one infers that these are also due to the thermal

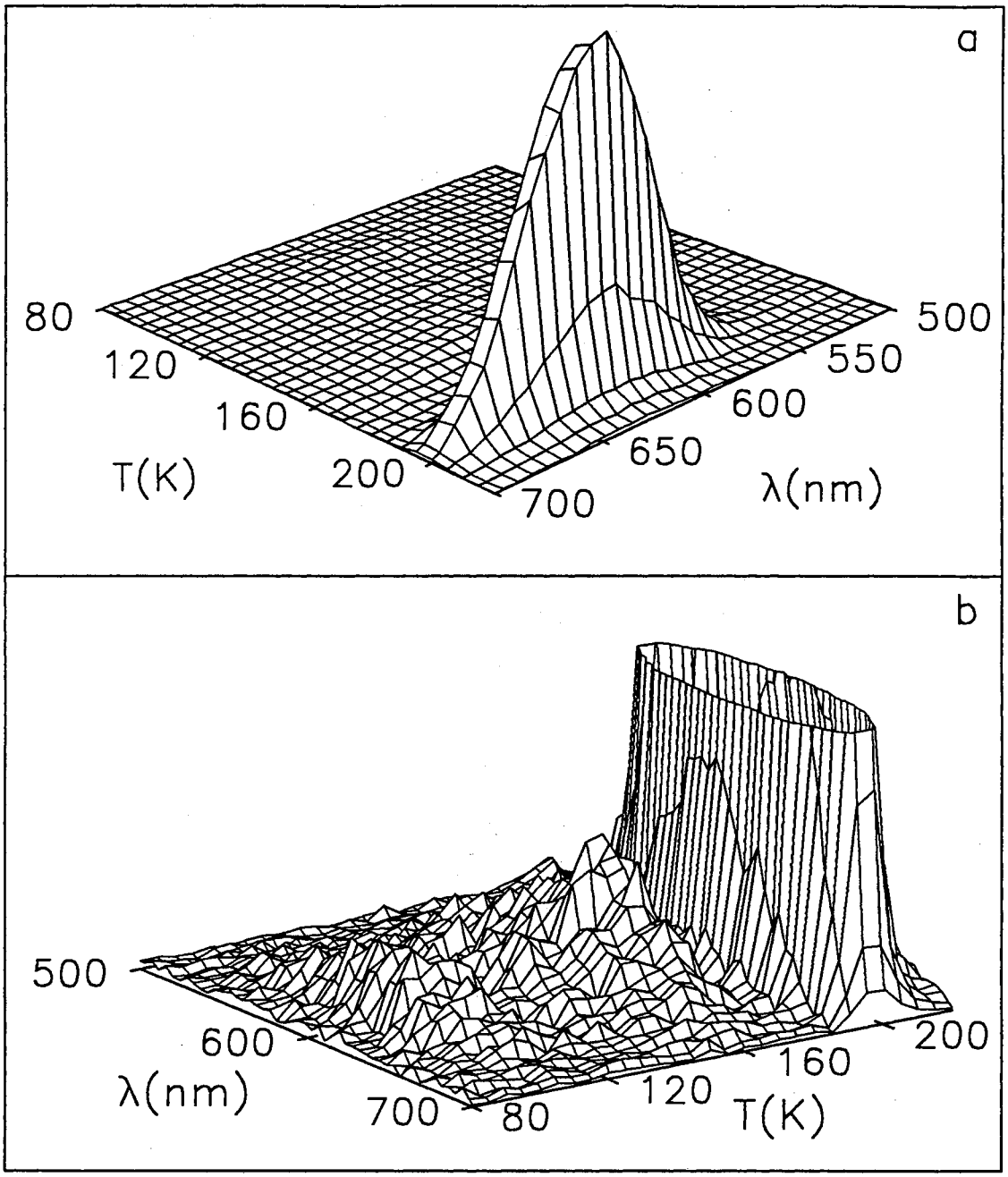

Figure 20. Wavelength dependence of TL emission from MG sample; only red emission is present. The same data is plotted in (a) and (b). (b) is a magnified view of (a) in order to show that the low temperature TL peaks, although weak, are indeed present. The sample was illuminated with light from an Argon ion laser (4.8mW) for 2min and heated at 5K/min with no bias applied: the sample was not fitted with electrodes.

release of electrons which subsequently recombine with holes trapped at the Cu_{red} centers. One may further infer from the conclusions of Fig. 19 that most, if not all, of the observed TSC peaks in the MG samples are also due to electron release.

We examined the PL spectra from both types of samples as a function of temperature and wavelength (i.e. thermal quenching). In order to reproduce, as closely as possible, the conditions present during TSC and TL, measurements were taken while the samples were being heated at a rate of 5K/min with a -5v bias applied. The resulting spectra are shown in Fig. 21. The insets to these figures show the details of the DAP* (donor acceptor pair) and exciton emission structure at 12K while the main figures show the overall PL structure as a function of temperature from 80K to 220K. The insets show that the PL spectrum of the MG sample is dominated by DAP emission and its phonon replicas, whereas the spectrum for the SPVT sample is dominated by exciton emission. The larger graph, for the SPVT sample, indicates the presence of both Cu_{red} ($\lambda \approx 647$nm; 1.92eV) and Cu_{green} ($\lambda \approx 535$nm; 2.32eV) emission. Identification of the exact wavelength for green emission was complicated by overlap with the large peak near 505nm (2.46eV).

Since the intensity of luminescence emission decreases exponentially with increasing temperature, one constructs a plot of $\ln(I_{PL})$ versus $1/T$ and extracts the activation energy from the slope (slope $= -E/k$). Fig. 22a shows the quenching of the luminescence for both red and green emission from an SPVT sample. At low temperatures we see that each luminescence peak appears to be associated with the same shallow level (15.7meV). It is believed that this is a shallow donor and that free electrons are momentarily captured by the shallow donor before recombining with holes at copper centers. This type of model has also been proposed by Stringfellow and Bube[44] and by Oczkowski[46] in which they found the shallow donor energy to be 12~15meV.

*Donor Acceptor Pair emission: Luminescence transition involves an electron on a donor site recombining with a hole on an acceptor site.

As the temperature increases to about 95K, however, the luminescence at 505nm begins to quench rapidly. It is difficult to determine the corresponding energy since the quenching occurs very quickly; by the time the temperature rises to 125K the slope again corresponds to an energy of 15.7meV. Apparently we are now seeing the tail of the emission peaks at 535nm and 647nm. A similar rapid quenching process is seen for the 535nm luminescence over the temperature range from 165K to 220K. It is likely that this process involves thermal excitation from the Cu_{green} center.

A thermal quenching plot for the MG sample is shown in Fig. 22b. In order to determine if more than one component is involved in the red emission (e.g. free to bound and a process involving the intermediate donor state) the quenching at the peak of the emission (625nm; 1.98eV) and 25nm to either side of the peak was analyzed. As the plot shows, each of these wavelengths quenches at the same rate and with a slope corresponding to a donor energy of 14.7meV. It is likely that this is the same donor species which is observed at 15.7meV in the SPVT samples. For temperatures greater than 175K all three of the components begin to quench more rapidly with a corresponding energy of 45.7meV. This energy may correspond to another donor level which acts as an intermediate level once the 14.7meV level has fully quenched. This process has not been previously reported for ZnSe.

An important observation, concerning the production of TL, is that the luminescence is quenched over the same temperature range for which TL is observed, indicating the likelihood that holes are being removed from the Cu–centers in sufficient numbers to result in a non–constant luminescence efficiency (τ/τ_r).

Photoconductivity and Wavelength Dependence of TSC and TL

The wavelength dependence of the photoconductivity (PC) was measured and TSC and TL measurements were performed following illumination at several different wavelengths. If the wavelength is varied so that the photon energy is less than the band-gap, the observed photoconductivity or TSC and TL must be a result of impurity absorption. Thus, a measurement of this type provides

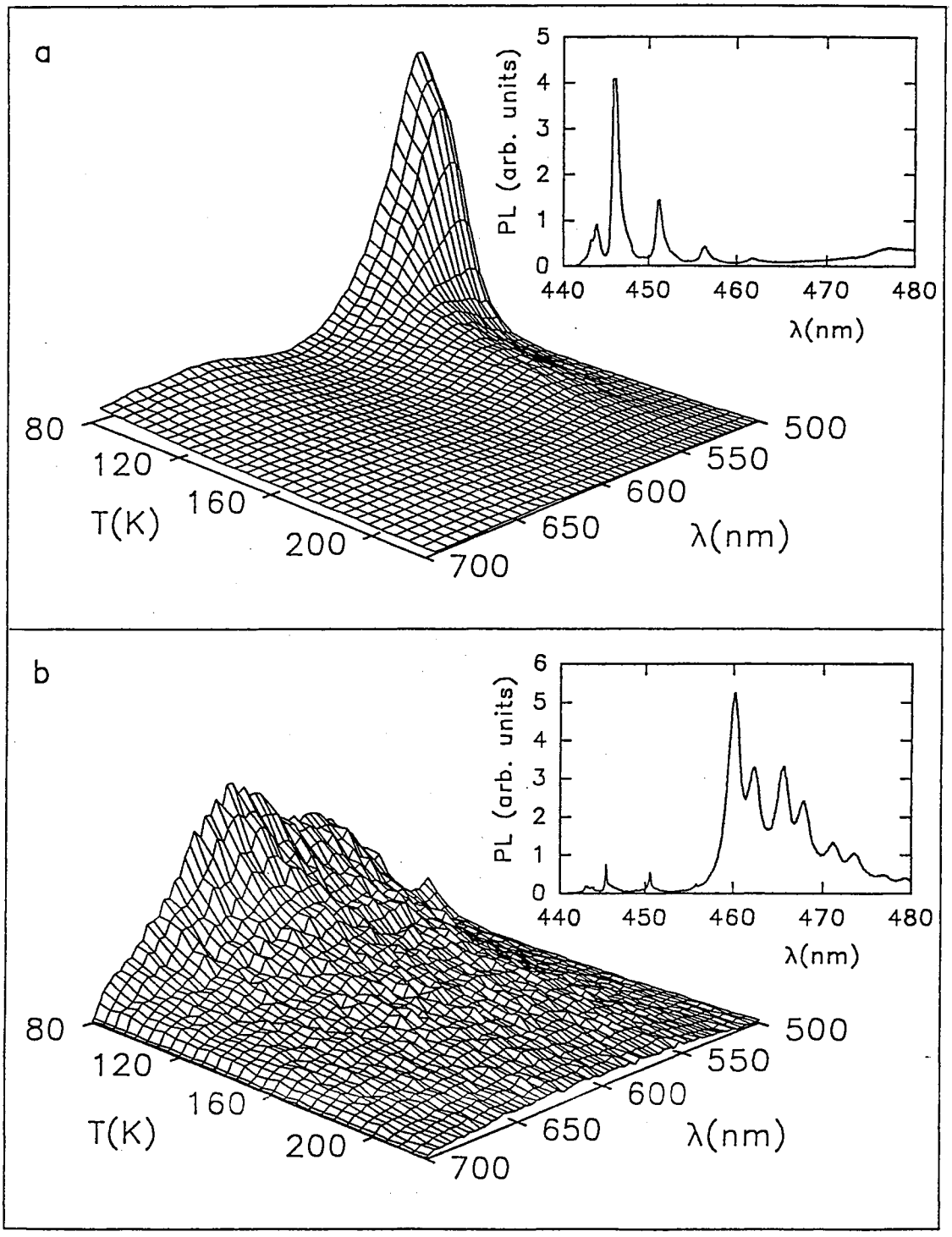

Figure 21. Emission spectrum of photoluminescence for (a) SPVT and (b) MG samples. Emission due to both Cu_{red} and Cu_{green} is observed. The sample was illuminated with light from an Argon ion laser (4.8mW) during heating, and was cooled and heated with a -5v bias applied. Insets show the PL spectra taken for the same samples at 12K.

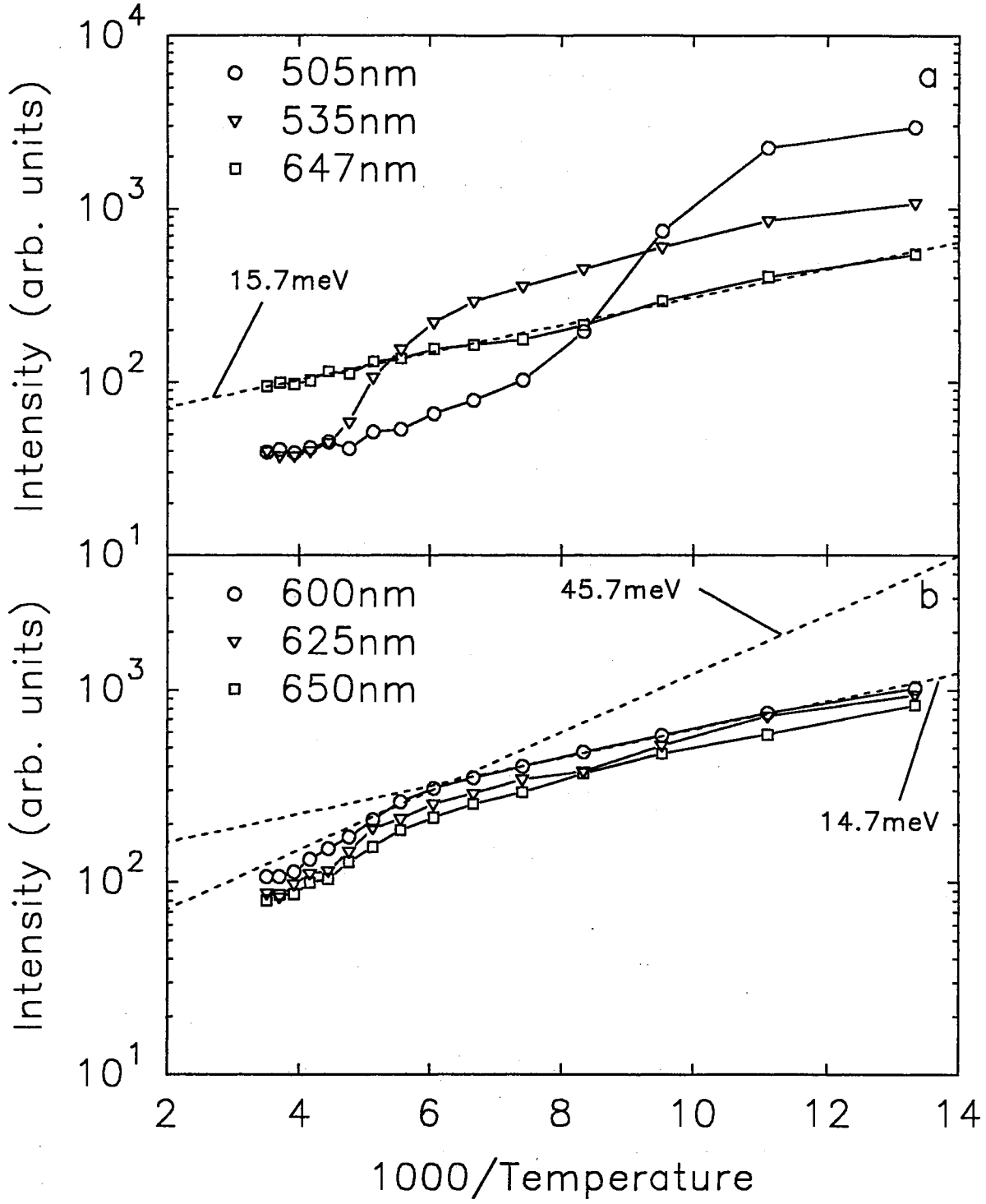

Figure 22. Thermal quenching plots for (a) SPVT and (b) MG ZnSe. The plot shows quenching of both red and green emission. Notice that red emission quenches with an activation energy of approximately 15meV for both SPVT and MG.

significantly more information about the deep levels than does standard 'white light illumination' measurements.

When measuring photoconductivity due to absorption by deep levels, while scanning from long to short wavelengths, one normally expects a stepwise increase in the conductivity when the energy is sufficient to excite electrons from the deep level to the delocalized band[20,47]. The reason for a stepwise increase is the fact that deep levels, unlike shallow levels, are delocalized in **k** space (momentum space). When the energy increases above the energy required for transitions to the bottom of the conduction band, electrons are excited into higher energy states within the band, thus the optical trap depth is taken as the rising edge of the photoconductivity step. For the case of shallow levels transitions occur at **k=0** only, thus the absorption lines are very sharp.

We see from the data in Fig. 23a and b that our PC spectra contain broad peaks. Milnes[47] claims that dips in a PC spectrum, such as those seen here, may be an indication of wavelength dependence of the optical cross section of the absorbing center. The PC spectrum for a MG ZnSe sample at 80K (Fig. 23a) shows PC increases at 920nm(1.35eV), 850nm(1.46eV), 630nm(1.97eV), 540nm(2.3eV) and a sharp increase toward the band edge between 475 and 440nm(2.61 and 2.82eV). Increases at 920 and 850 are attributed to absorption by deep, empty hole traps (i.e. they contain electrons). Since these two trap levels are close to mid-gap they are not observed during TSC and TL; they are too deep. Although the wavelength of 630nm is the same as the emission wavelength due to recombination on the Cu_{red} center, the increase in PC at 630nm is not due to absorption at the Cu_{red} center. Stringfellow and Bube[44] report the absorption threshold for the Cu_{red} center as 539nm(2.3eV). Thus the increase in PC observed at 540nm is due to absorption at the Cu_{red} center. Stringfellow and Bube also report an absorption threshold of 477nm(2.6eV) for the Cu_{green} center. It is difficult to isolate the absorption at the Cu_{green} center in the results presented here, but it is believed that the increase in PC from 475 to 440nm includes the Cu_{green} center as well as the band edge.

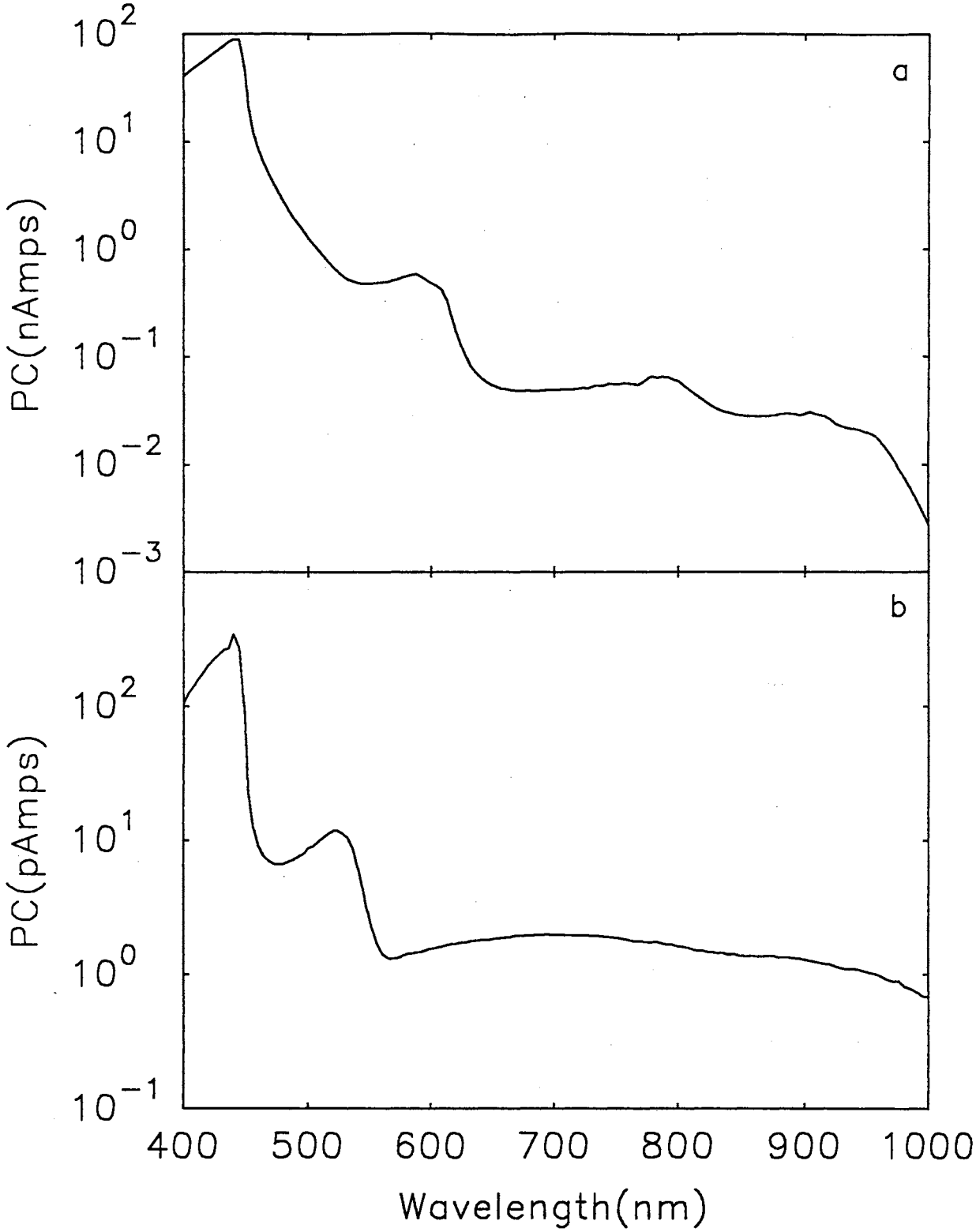

Figure 23. Wavelength dependence of photoconductivity for (a) MG and (b) SPVT grown ZnSe.

The PC spectrum for an SPVT sample at 80K is shown in Fig. 23b. The main features of this spectrum are the broad PC peak centered near 700nm(1.77eV) and a narrower peak near 520nm(2.38eV). The latter has a rising edge near 560nm(2.21eV) and is believed to be associated with the Cu_{red} center, although the threshold wavelength is longer than that seen for the MG sample (540nm). The broad peak at 700nm may be associated with a series of mid–gap states such as those reported by Ohki *et al.*[48] for nitrogen doped metalorganic vapor phase epitaxy ZnSe films. Comparison of PC data for MG and SPVT grown samples indicates a considerably more complex deep level structure for MG samples.

In order to properly compare TSC and TL obtained at different illumination wavelengths, it is necessary to make sure the sample is being illuminated with approximately the same number of photons at each wavelength. To do this, the spectral output of the tungsten lamp (in combination with the SPEX 1681 spectrograph) was measured using an Oriel thermopile.

Once it was determined that the approximate number of photons at each wavelength was the same, TSC and TL was measured following illumination at several wavelengths. It was found that the results for the MG sample varied considerably as the wavelength was varied between 450nm and 600nm.

Figure 24 shows the TSC spectrum obtained for a MG sample illuminated at 500nm. The variation in peak heights versus illumination wavelength is shown in Fig. 25a and b. As the graphs reveal, most of the TSCpeaks decrease with increasing wavelength. This may indicate the dominance of surface states in the TSC spectrum. As the wavelength increases there is less absorption at the surface, thus, the concentration of free carriers which may be captured by surface states is reduced. Peak 9 is seen to grow as the wavelength increases from 450 to 510nm. As the wavelength increased beyond 510nm, peak 9 decreases. Since there is less surface absorption at longer wavelengths, one expects bulk states to become more involved in the absorption process, thus, an increase in peak height with longer wavelength implies the association with bulk states rather than surface states. As the wavelength increases above 510nm there is no longer sufficient photon energy

for the absorption by these bulk states. For peak 5, a decrease in peak height is seen as the wavelength increases from 450 to 530nm. As the wavelength is further increased, however, peak 5 begins to grow. This behavior indicates that at the temperature corresponding to peak 5 there may actually be two very closely overlapping peaks; one due to surface states and one due to bulk states.

Growth of TL peaks versus wavelength for a MG sample is shown in Fig. 26. Since TL is dependent on the populations of both electron and hole traps, interpretation of these results is not as straightforward as the interpretation of TSC results. The behavior of TL peaks 5 and 6 is similar to the behavior of TSC peak 9. TL peaks 1 and 2 also show similar behavior but the TL peak maximum occurs for an illumination wavelength of 480nm. Recall from the discussion of PC that absorption at the Cu_{green} center occurs near 477nm. Thus, TL peaks 1 and 2 may be associated with absorption at the Cu_{green} center although the TL process involves recombination with the Cu_{red} center. Perhaps absorption at the Cu_{green} center simply provides electrons which fill the electron traps involved in the TL process.

When TSC was measured for an SPVT sample as a function of illumination wavelength (from 450 to 900nm), it was found that the TSC peak heights were independent of wavelength. The conclusion reached from this important result is that excitation of electrons into mid-gap states creates free holes in the valence band which subsequently become trapped. These trapped holes then give rise to the observed TSC.

A significant point to note here is that both types of sample contain mid-gap states. These states may be instrumental in preventing both n- and p-type doping by providing a large concentration of compensating centers.

Hard-to-Fit TL Peak

In this section special consideration is given to TL peak 6 in the melt grown sample. This particular peak has proven quite difficult to analyze. As mentioned

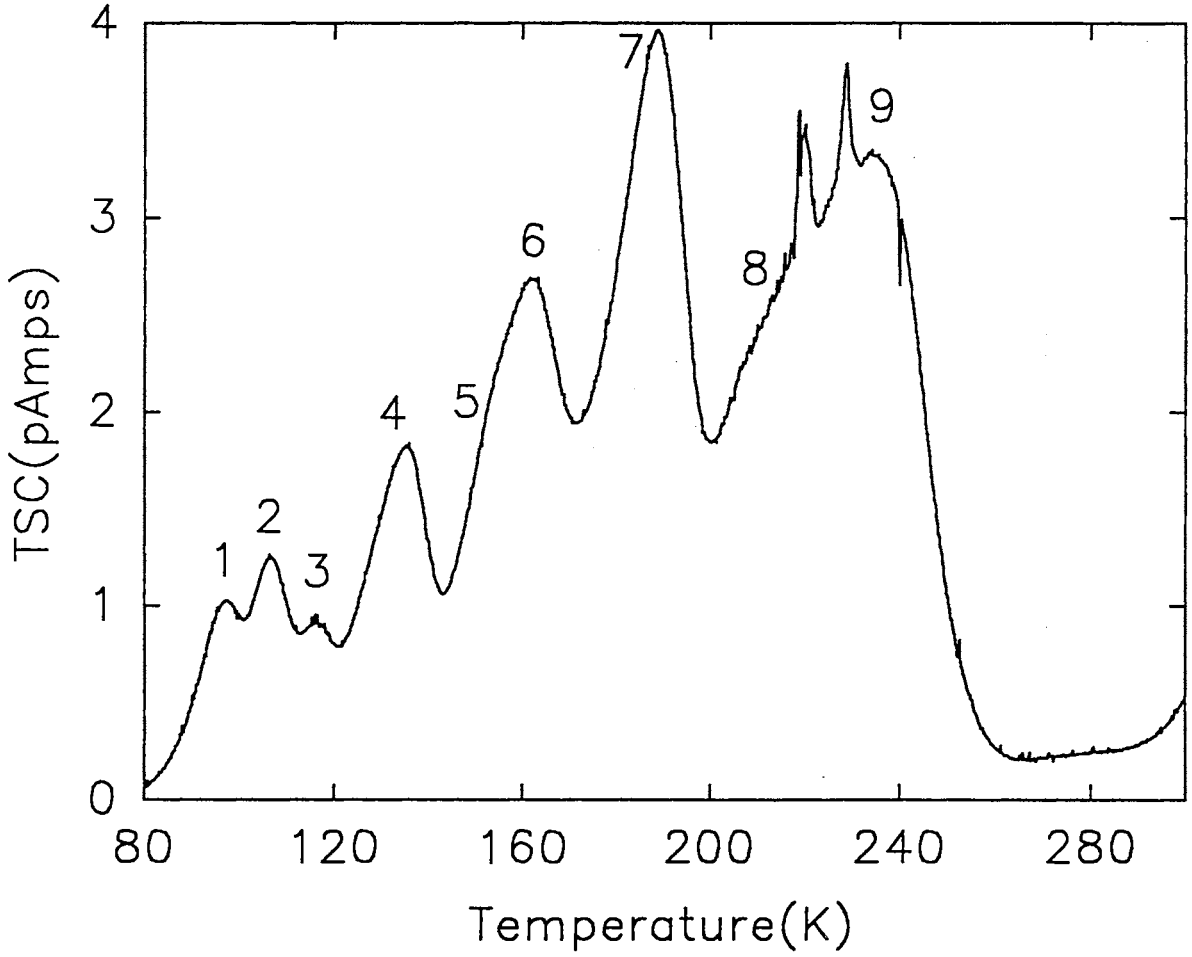

Figure 24. TSC from MG ZnSe illuminated at 500nm. Sample was cooled with a -5v bias applied and heated at 5K/min with the same applied bias.

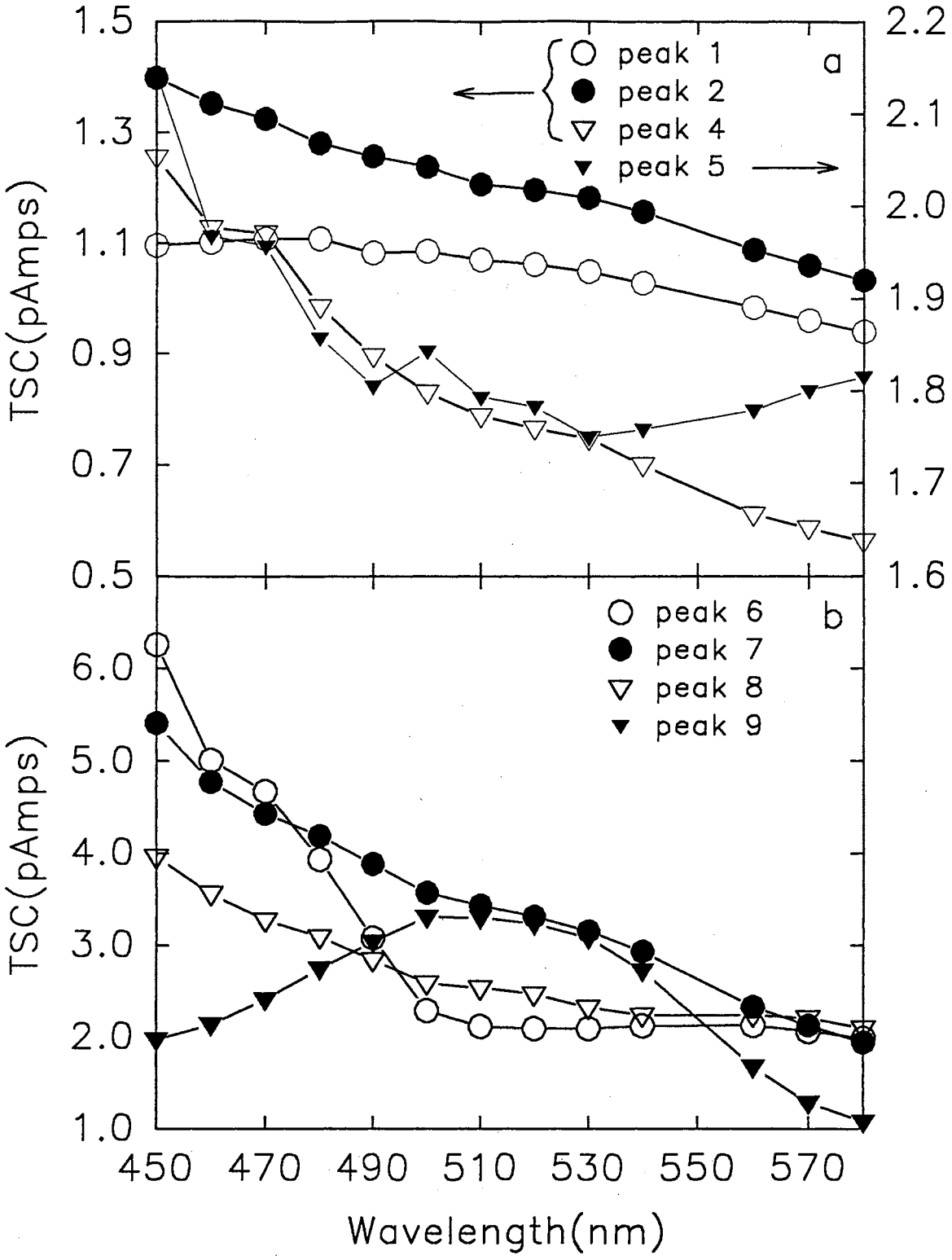

Figure 25. Height of major TSC peaks as a function of illumination wavelength for a MG sample. Growth of peaks (a) 1, 2, 3, 5 (b) 6, 7, 8, and 9 are shown. See Fig. 24 for identification of peaks.

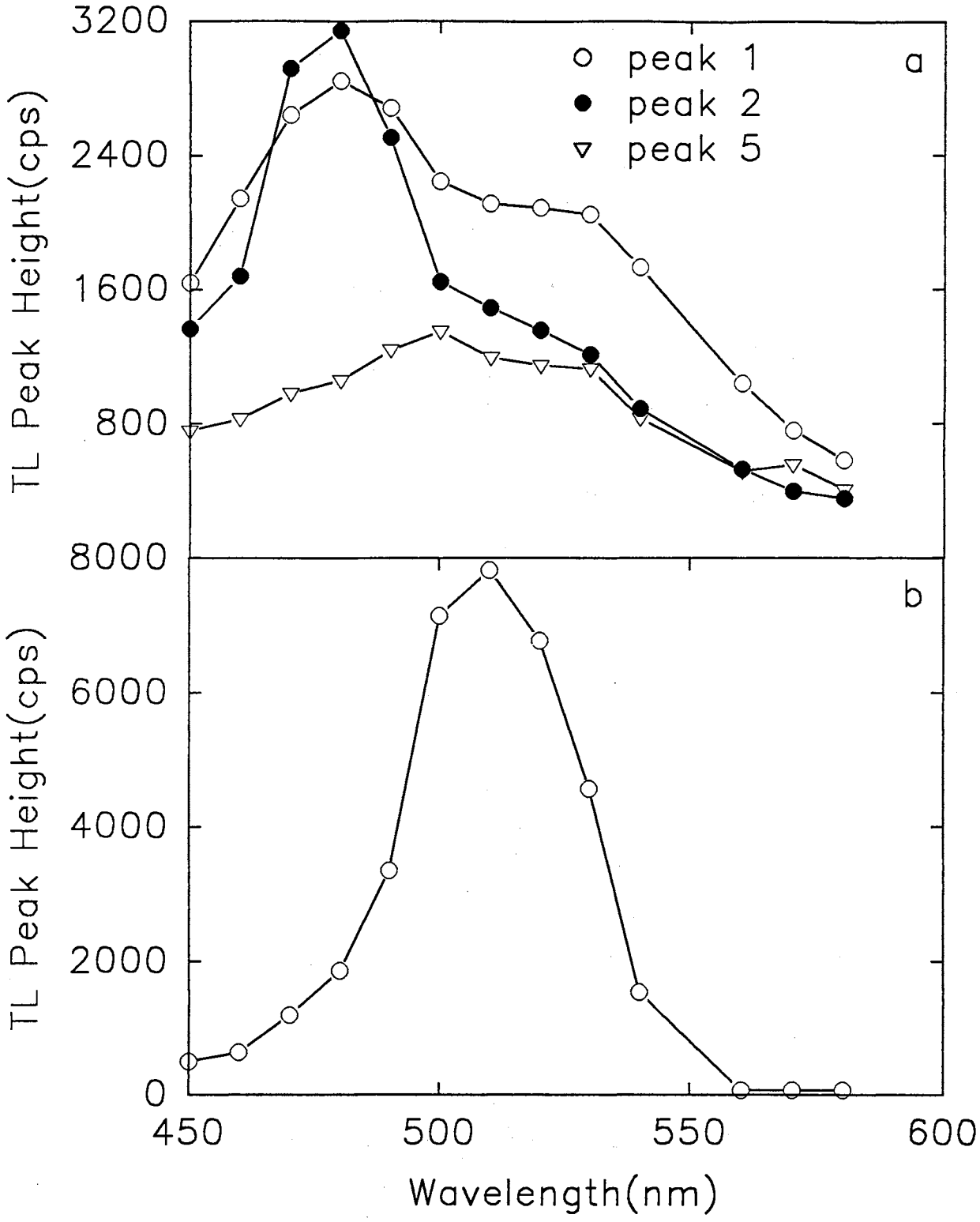

Figure 26. Height of major TL peaks as a function of illumination wavelength for a MG sample. Growth of peaks (a) 1, 2, 5 (b) and 6 are shown. See Fig. 15b for identification of peaks.

earlier, attempts at fitting to first–order and second–order peaks as well as a gaussian distribution of trap levels have all failed. In this section other methods of analysis will be considered in order to determine the activation energy of the trap level associated with this TL peak.

Heating Rate Analysis

If TSC or TL data are recorded using several heating rates, it is observed that as the heating rate increases, the peaks both increase in magnitude and shift toward higher temperature. This behavior was first observed by Booth[49] in 1954. Booth equated the derivative of equation (16) to zero to obtain the following condition for the TL peak maximum:

$$\frac{\beta E}{kT_m^2} = s \exp\left(-\frac{E}{kT_m}\right) \tag{78}$$

where equation (14) has been substituted for n_c and it was assumed that $\tau = tau_\tau$. T_m is the temperature corresponding to the peak maximum. By evaluating equation (78) at two different heating rates, Booth obtained the following expression for the activation energy E

$$E = \frac{kT_{m1}T_{m2}}{T_{m1} - T_{m2}} \ln\left[\frac{\beta_1}{\beta_2}\left(\frac{T_{m2}}{T_{m1}}\right)^2\right] \tag{79}$$

Hoogenstraaten[50] took this analysis one step further, suggesting the use of several linear heating rates and plotting $\ln(T_m^2)/\beta$ versus $1/T_m$. According to equation (78), this plot should be linear with a slope of E/k and an intercept of $\ln(sk/E)$. This analysis, of course, assumes that the frequency factor is a constant. This assumption may be justified if the range of T_m is sufficiently small.

The main weakness of this method is the inability to accurately determine s. Since s is determined from the value of the intercept, one must extrapolate over a wide temperature range to obtain its value. By performing this extrapolation, however, one can no longer justify ignoring the temperature dependence of s.

Chen and Winer[51] accounted for the temperature dependence of the frequency factor by parameterizing it as in equation (68). If this parameterization is substituted into equation (16) before equating the derivative to zero, then equation (78) becomes

$$\frac{T_m^2}{\beta} = \frac{E + (2-b)kT_m}{BkT^{2-b}} \exp\left(-\frac{E}{kT_m}\right) \tag{80}$$

or

$$\ln\left(\frac{T_m^2}{\beta}\right) = \ln\left(\frac{E + (2-b)kT_m}{BkT_m^{2-b}}\right) + \frac{E}{kT_m} \tag{81}$$

where Chen and Winer argue that the denominator of the preexponential factor is weakly temperature dependent and thus treated as a constant since $E \gg (2-b)kT_m$. Unfortunately, b must be determined by some other means before determining E from the above equation.

If, however, equation (80) is used as a three parameter fitting equation, the values of E, B and b may be determined simultaneously. It was found, however, that the values obtained for B and b are still not in very good agreement with other methods when tested on computer generated data. The most likely cause for this basic weakness is the insensitivity of equation (80) (and Eqn. (81)) to changes in B and b. Since B and b appear in linear (logarithmic) terms, whereas E appears in an exponential (linear) term, small changes in E will cause large errors thus demanding a better fitted value for E than for B or b. In cases where peak overlap is significant, the values of E are called into question as well.

Variable heating rate data was obtained for a MG sample at heating rates from 3K/min to 6K/min in increments of 0.5K/min. The resulting TL curves are shown in Fig. 27(a) and the plot of $\ln(T_m^2/\beta$ versus $1/T$ is shown in Fig. 27(b). From the slope and intercept of this plot, an activation energy of 0.571eV and a frequency factor of $4.46 \times 10^{14}(s^{-1})$ were obtained. If, rather than performing linear regression, the plot in (b) is fitted to equation (81) an activation energy of 0.539eV and a frequency factor of $1.35 \times 10^{11} \times T^{0.06}$ is obtained. Evaluating the latter expression at 195K gives a frequency factor of $4.33 \times 10^{13}(s^{-1})$ which is in

reasonably good agreement with the result obtained from linear regression. Note that these frequency factor values are considerably higher than the values for the other TL peaks given in table III.

Initial Rise

The observation that the initial rise portion of a TSC or TL curve may be described by a simple exponential was first made by Garlick and Gibson [34]. They applied the approximation that $n \approx n_0$ for $T \approx T_0$ where T_0 is a low enough temperature that the trap is not very active. As a general rule, the value of T_0 should correspond to a temperature for which the magnitude of the TSC or TL does not exceed 15 percent of the peak maximum. By describing TSC or TL by the relation

$$I = const \times \exp\left(-\frac{E}{kT}\right), \tag{82}$$

where I represents TSC or TL, the activation energy is obtained from a line of slope $-E/k$ on a plot of $\ln(I)$ versus $1/T$.

In order to apply the initial rise technique, there must be no overlap in the initial rise portion of the peak under study. For the data presented here, the hard–to–fit TL peak appears sufficiently free of overlap. Fig. 28 shows the plot of $\ln(TL)$ versus $1/T$ for the initial rise portion of the TL curve from Fig. 27(a) which was obtained at 5K/min. From this initial rise plot the activation energy was found to be 0.876eV. This result, as expected, is not in good agreement with the results of fitting (see Table III). Better agreement was expected, however, with the heating rate analysis of the previous section.

Comments

It is becoming obvious that TL peak 6 cannot be described by standard first–order kinetics. It has been shown that it was not possible to fit the peak to any of the standard TL equations and each other method of analysis used yielded a

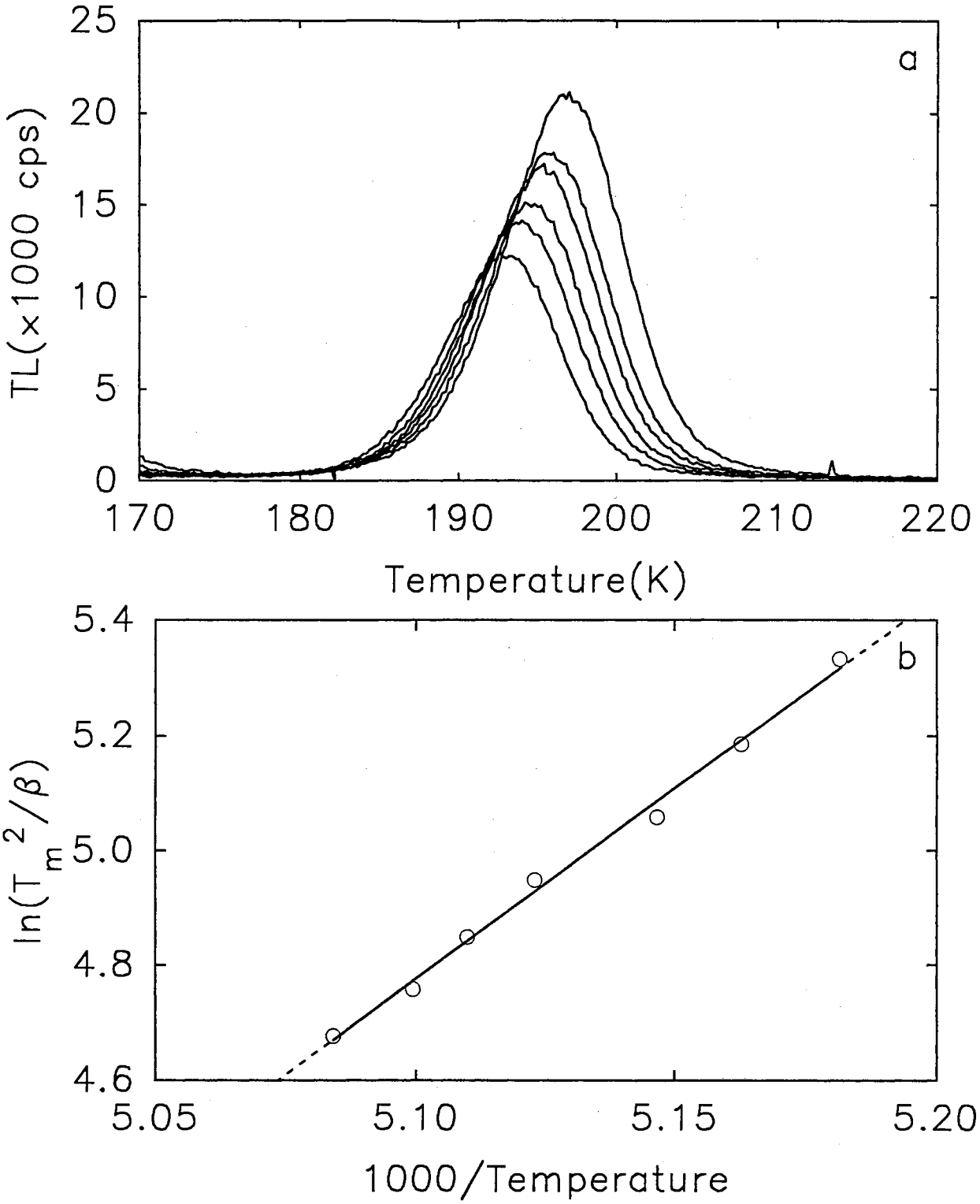

Figure 27. Heating rate analysis of hard-to-fit TL peak 6. (a) data obtained at heating rates of 3.0, 3.5, 4.0, 4.5, 5.0, 5.5 and 6.0K/min; (b) heating rate analysis plot: open circles represent data, dotted line represents linear regression (E=0.571eV) and solid line represents least squares fit to equation (81) (E=0.539eV).

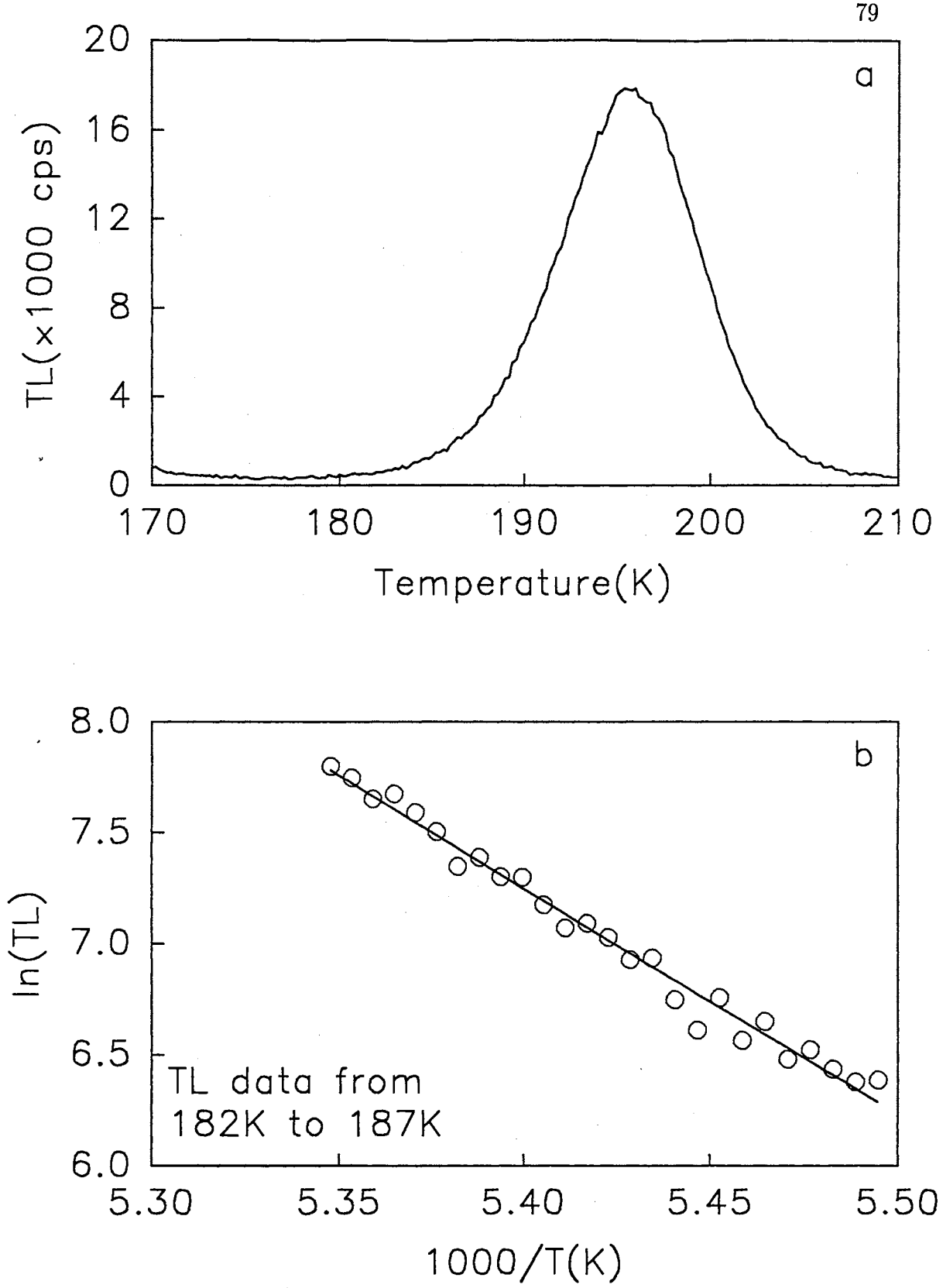

Figure 28. Initial rise analysis of hard-to-fit TL peak 6. This plot shows the initial rise portion of the 5K/min curve from figure 27(a). Open circles represent data and solid line represents linear regression. From the slope of the solid line an activation energy of 0.876eV is obtained.

different result. From PL emission analysis (page III) we conclude that over the temperature range of the TL peak in question, we may be observing the effects of simultaneous release of electrons and holes. The kinetics which describe the simultaneous release of electrons and holes have been investigated by Schön [52,53] and by Klasens [54] and the effects on TL analysis have been discussed by Chen *et al.* [55] and by McKeever *et al.* [56]. Their findings indicate that one may obtain a 'good' fit to equation (20) but the physical interpretation of the parameter values obtained is not straightforward. In particular, the E values obtained from the TL curves may not simply be interpreted as 'trap depths' but rather as a weighted average of the trap depth and the depth (from the valence band) of the recombination center[55,56].

CHAPTER IV

DLTS THEORY

Deep level transient spectroscopy (DLTS) is a spectroscopic technique for characterizing deep level defects and impurities in p–n junction and Schottky diodes. The method, which exploits the characteristics of junction capacitance, was first introduced by Lang[57,58] in 1974 in a study of oxygen donors and ZnO complexes in GaP p–n junctions. Lang claimed that earlier capacitance methods[59–62] were limited to detecting traps deeper than 0.3eV from the delocalized band. Overcoming these limitations was the motivation for developing DLTS.

The basic principle of DLTS is to monitor transient changes in the capacitance of a junction following a sudden change in the applied bias. By observing the evolution of this transient over a wide temperature range it is possible to obtain a great deal of information about the defects present in the region of the junction.

Schottky Barriers

Before proceeding with a discussion of DLTS it is necessary to briefly discuss the physics of Schottky barriers. Since this development is available in many texts[63,64], it will not be covered in detail here. Also, p–n junctions will be mentioned only briefly for two reasons: first, a Schottky diode is equivalent, from a mathematical standpoint, to a p–n junction in which one side of the junction is very heavily doped[63] (i.e. one sided junction). Second, in the following chapter experimental results are presented for a DLTS study of a ZnSe/platinum Schottky diode.

Consider the metal/semiconductor interface shown in Fig. 29. Since the band structure of the two materials is quite different, the bands in the semiconductor

will bend to accommodate the metal and ensure that the Fermi level is constant throughout the junction. For the specific case shown, the metal is in contact with an n–type semiconductor and the metal work function ϕ_m is greater than the semiconductor work function ϕ_s. It is this difference in the work functions which gives rise to the Schottky effect[63].

Band bending near the junction interface causes electrons in the conduction band of the semiconductor to be forced deeper into the semiconductor thus leaving the junction depleted of free charge. This 'depletion' region, however, contains bound charge since some of the donor states are now above the Fermi level and thus have become ionized. The junction may be characterized as a parallel plate capacitor of plate separation x_n and capacitance C where

$$C = \epsilon \frac{A}{x_n} \tag{83}$$

and ϵ is the dielectric constant. The quantity x_n is usually referred to as the depletion width or depletion length.

If N_d' represents the net concentration of ionized donors then the charge density in the depletion region is $N_d'q$ where q is the charge of the ionized donor. By solving Poisson's equation in the depletion region it is found that

$$x_n = \sqrt{\frac{2\epsilon(V_d - V_a)}{N_d'q}} \tag{84}$$

where V_d is the built in potential of the barrier and V_a is the externally applied forward bias voltage.

By combining equations (83) and (84) one obtains the junction capacitance as a function of dopant concentration N_d and applied voltage V_a

$$C = A\sqrt{\frac{N_d'q\epsilon}{2(V_d - V_a)}} \tag{85}$$

Notice that as the reverse bias is increased (i.e. V_a is made more negative) the capacitance C is decreased. Thus the bias voltage gives direct control of the junction capacitance.

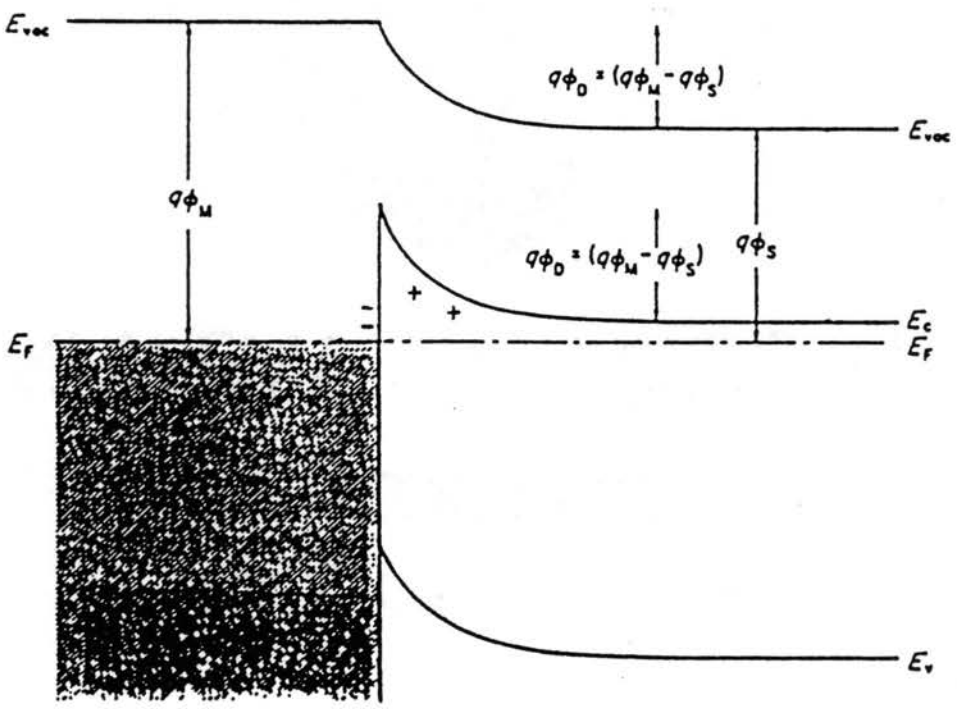

Figure 29. Schottky barrier on an n–type semiconductor. The quantity $q\phi_d$ is the built in potential V_d.[63]

If we invert and square both sides of equation (85) the following expression is obtained

$$\frac{1}{C^2} = \frac{2V_d}{A^2\epsilon N'_d q} - \frac{2V_a}{A^2\epsilon N'_d q} \tag{86}$$

From this equation it is apparent that if the capacitance is measured at several reverse bias voltages V_a, a plot of $\frac{1}{C^2}$ versus V_a will have a slope proportional to $1/N'_d$. Once N'_d has been determined from the slope, the barrier potential V_d may be determined from the intercept. The value obtained for N'_d, as mentioned earlier, is the net ionized donor concentration. That is, N'_d actually represents the concentration of ionized donors minus the concentration of trapped charge (i.e. electrons in deep traps). If the temperature is sufficiently high then all donors are ionized and the concentration of trapped charge is negligible. In this case, the value of N'_d obtained from equation (86) is the total donor concentration N_d.

DLTS Experiments

As mentioned earlier, DLTS exploits the transient capacitance response under the influence of a sudden change in the applied bias. Consider a Schottky contact which is subjected to a reverse bias, the Fermi level is lowered and, according to equation (84), the depletion width increases. The equilibrium capacitance under this reverse bias condition is referred to as the quiescent capacitance C_q.

Continuing the above discussion, it is helpful to treat majority and minority traps separately.

Majority Carrier Traps

In an n–type semiconductor, majority traps are electron traps. When the reverse bias is applied and the Fermi level shifts down, some electron traps may now exist above the Fermi level. These traps will quickly give up their electrons as shown in Fig. 30a.

If the magnitude of the reverse bias is suddenly decreased (or if the junction is forward biased), then the Fermi level is shifted up and the traps are once again

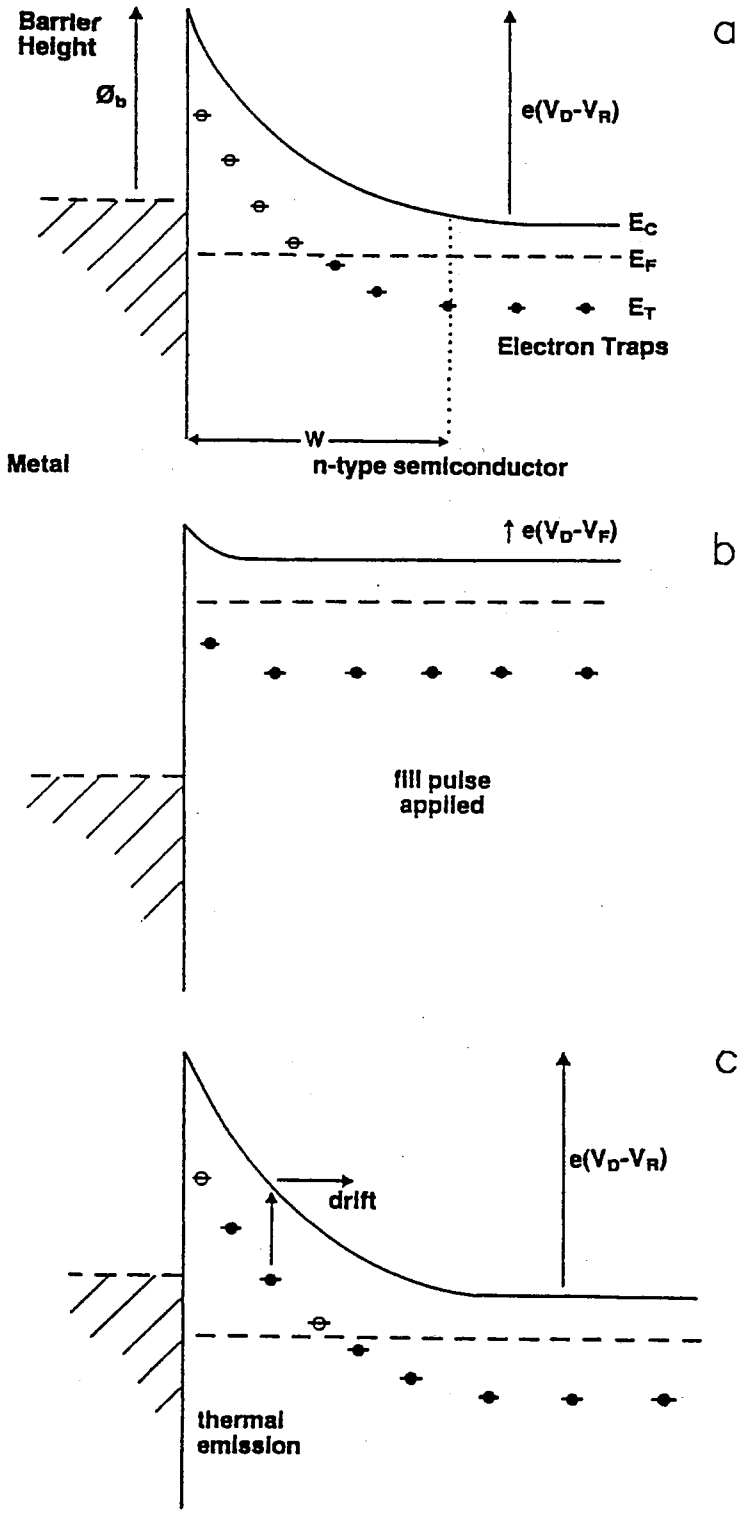

Figure 30. Schottky contact on an n–type semiconductor showing (a) junction under reverse bias with empty traps above Fermi level (E_F), (b) Filled traps during fill pulse and (c) thermal emission from traps following fill pulse. Open circles represent empty traps and solid circles represent filled traps.

filled as shown in Fig. 30b. This reduction of reverse bias is usually in the form of a short pulse and is referred to as a 'fill' pulse. At the end of the fill pulse the reverse bias is restored and the depletion width returns to its original value. The quiescent capacitance, however, is not immediately restored. Since some electrons still remain within the depletion region the amount of trapped charge has been reduced, thus, the capacitance has been reduced as well. The electrons in these traps will eventually be thermally excited back into the conduction band (see Fig. 30c) and the capacitance will return to C_q. The transient response of the junction capacitance is shown in Fig. 31a.

Minority Carrier Traps

The situation for minority traps is very similar to that already described for majority traps. Once again an n–type semiconductor is assumed, thus, minority carriers are holes.

In order to provide holes for trapping, the fill pulse must be sufficient to forward bias the junction and cause minority carrier injection. This may only be done for p–n junctions. In the case of Schottky diodes, optical excitation is used to generate free holes (optical DLTS). As the free holes become trapped the amount of bound charge increases, thus the capacitance increases. As these holes are thermally detrapped following the end of the fill pulse, the capacitance decreases back to the quiescent level C_q as shown in Fig. 31b.

For both minority and majority traps, the rate at which the capacitance returns to the quiescent level depends on the thermal excitation rate (also called emission rate). The rate of excitation is strongly temperature dependent as indicated by equation (48).

The DLTS spectrum is obtained by measuring the value of the capacitance at two times, t_1 and t_2, following the end of the fill pulse. These measurements are made many times while the temperature is being changed so that the measurements

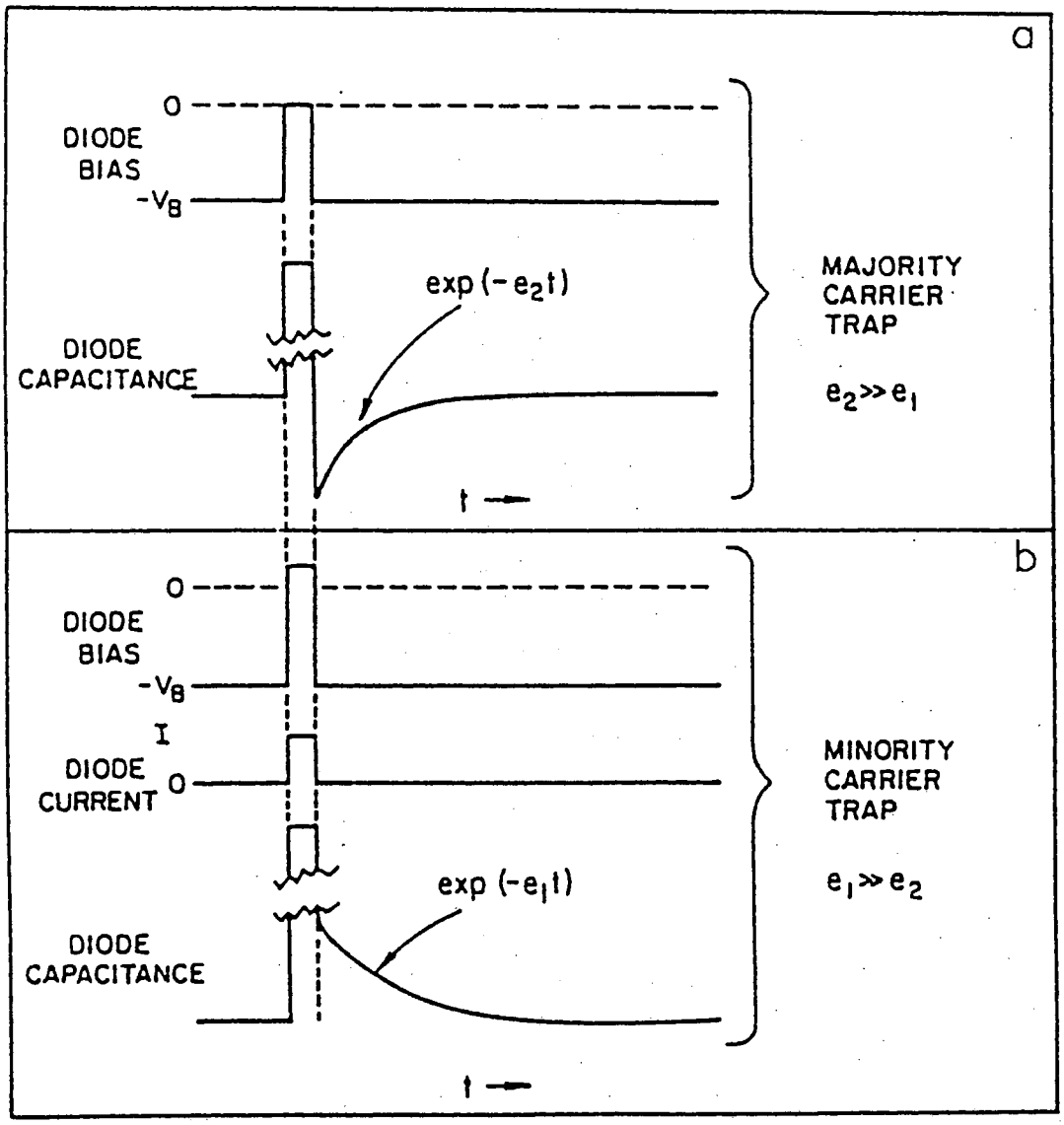

Figure 31. Bias pulse and capacitance transients for trap filling and emptying cycle for (a) majority traps and (b) minority traps.

cover a wide range of emission rates. The sampling times t_1 and t_2 are made quickly enough that the temperature does not change during the measurement.

If a plot is constructed of $\Delta C(T)(= C(t_2) - C(t_1))$ versus temperature, a curve such as that shown in Fig. 32 is obtained. As the figure indicates, at high temperatures the emission rate is high and the transient decays before a measurement is made at time t_1. For low temperatures the emission rate may be so slow that there is no measurable decay between times t_1 and t_2. Thus ΔC is small for both high and low temperatures. For intermediate temperatures, however, a significant change may occur between t_1 and t_2. The temperature at which the maximum of ΔC occurs depends on the choices of t_1 and t_2. For the example in Fig. 32, the DLTS spectrum of a majority carrier trap is shown; note that the peak is positive. By examining Fig. 31a and b, it is easily realized that a minority carrier trap will result in a negative peak. Thus DLTS provides for easy identification of minority and majority traps.

Theory and Data Analysis

In order to analyze the kinetics involved during a DLTS measurement, consider a single electron trapping level of concentration N in which there is a concentration n of trapped electrons. The rate equation describing the transfer of charge between the trapping level and the conduction band is given by equations (7) and (8). For the purposes of DLTS analysis (in the absence of recombination) we write

$$\frac{dn_c}{dt} = e_n n - c_n n_c (N - n) = -\frac{dn}{dt} \tag{87}$$

where e_n is the electron emission rate (s^{-1}) and c_n is the electron capture coefficient (cm^3/s). Comparison to equations (7) and (8) indicates that the emission rate and capture coefficient are defined as

$$e_n = N_c S v_e \exp\left(-\frac{E}{kT}\right) \tag{88}$$

and

$$c_n = S v_e \tag{89}$$

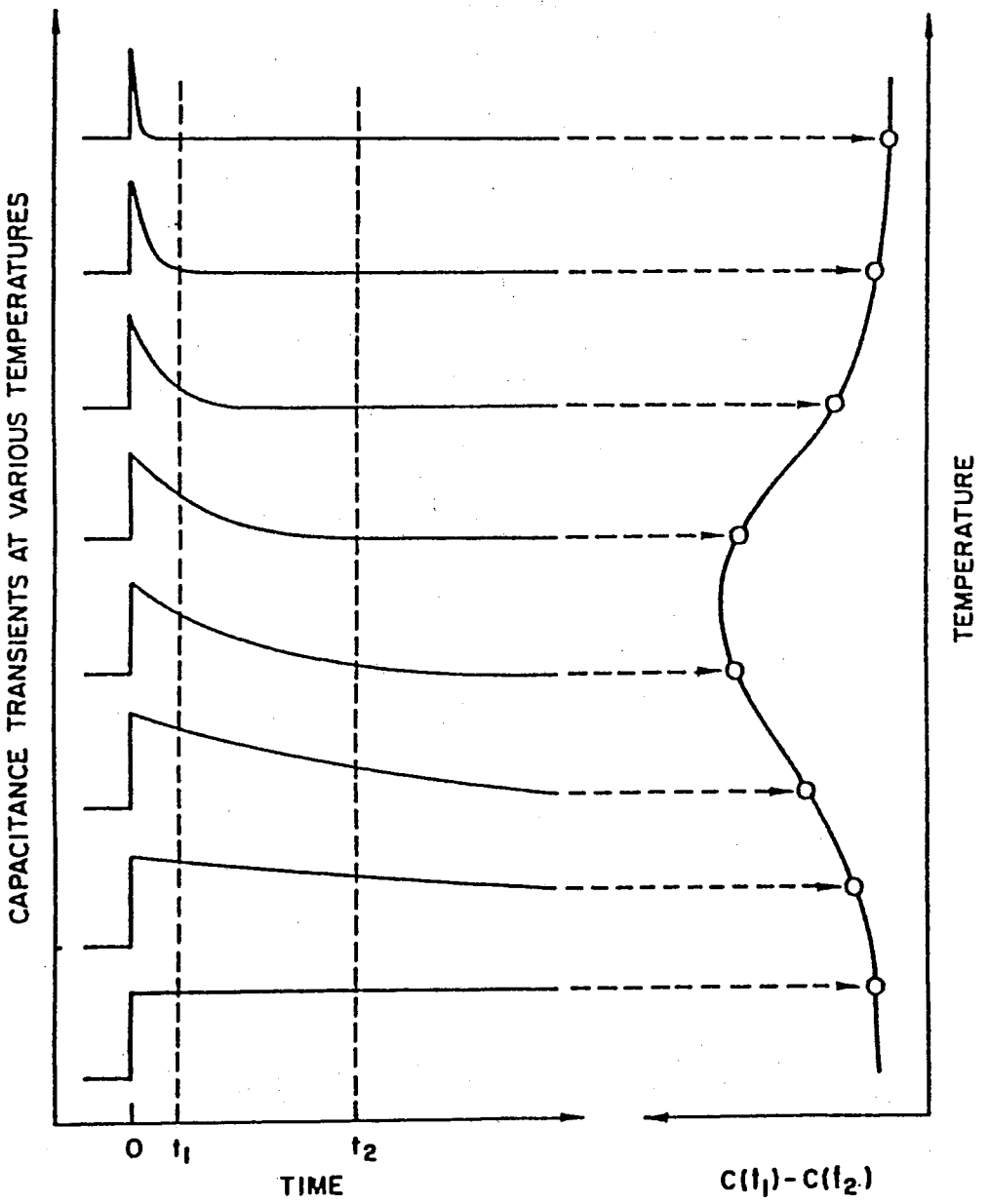

Figure 32. Illustration of how a DLTS peak is obtained from the capacitance transients.

respectively. From the capture coefficient, the capture rate is easily obtained by multiplying by the concentration of carriers available for capture (n). Thus,

$$\frac{1}{\tau_{c_n}} = Sv_e n_c \tag{90}$$

where the capture rate has been written as the inverse of the capture lifetime for electrons τ_{c_n}.

At the end of a fill pulse the depletion region is depleted of free carriers, thus the capture term in equation (87) is assumed to be zero. This assumption leads to the simple, first–order relationship

$$n(t) = n_0 \exp(-te) \tag{91}$$

where n_0 is the trapped charge concentration at the end of the fill pulse ($t = 0$).

An equation analogous to equation (87) may be written for a trap interacting with the valence band, namely

$$\frac{dp}{dt} = e_p(N - n) - c_p pn \tag{92}$$

where e_p is the hole emission rate, c_p is the hole capture coefficient and p is the concentration of free holes. Since equation (92) leads to equations analogous to (88), (89) and (90); we may drop the subscripts and write

$$e = N_D S v_{th} \exp\left(-\frac{E}{kT}\right), \tag{93}$$

$$c = Sv_{th} \tag{94}$$

and

$$\frac{1}{\tau_c} = Sv_{th} n_D \tag{95}$$

where N_D, v_{th} and n_D are the density of states, thermal velocity and carrier concentration for the corresponding delocalized band.

Activation Energy and Trap Concentration

For interaction with a single trap level the transients shown in Fig. 31 may be described by

$$C(t) = A\sqrt{\frac{(N_d - n(t))q\epsilon}{2(V_d - V_a)}} \tag{96}$$

where we have replaced the net ionized donor concentration N_d' in equation (85) with $(N_d - n(t))$ where N_d is the donor concentration and $n(t)$ is the concentration of carriers in deep traps. Equation (96) may be written as

$$C(t) = A\sqrt{\frac{q\epsilon N_d}{2(V_d - V_a)}}\sqrt{1 - \frac{n(t)}{N_d}}. \tag{97}$$

If it is assumed that the donor concentration is much greater than the concentration N of the deep traps under study[65] (i.e. $N_d \gg N$), then we may approximate the second square root term in equation (97) by the zeroth and first order terms in a binomial expansion. Thus, we approximate $C(t)$ as

$$C(t) \approx A\sqrt{\frac{q\epsilon N_d}{2(V_d - V_a)}}\left(1 - \frac{n(t)}{2N_d}\right) \tag{98}$$

Substitution of equation (91) into equation (98) leads to the simple exponential decay relationship

$$C(t) = A\sqrt{\frac{q\epsilon N_d}{2(V_d - V_a)}}\left[1 - \frac{n_0}{2N_d}\exp(-te)\right]. \tag{99}$$

With C defined by the above equation we may now write the expression for the value of $\Delta C(T)$ for two arbitrary times t_1 and t_2 as

$$\Delta C(t_1, t_2) = \frac{An_0}{2N_d}\sqrt{\frac{q\epsilon N_d}{2(V_d - V_a)}}\left[\exp(-t_1 e) - \exp(-t_2 e)\right] \tag{100}$$

Let e_{max} represent the emission rate at the peak of the DLTS curve. Therefore, by definition of e_{max}, the derivative of $\Delta C(T)$ with respect to e, at the peak maximum, is zero. Thus,

$$\frac{d\Delta C(T)}{de}\Big|_{e=e_{max}} = -t_2\exp(-t_2 e_{max}) + t_1\exp(-t_1 e_{max}) = 0 \tag{101}$$

Solving the above equation for e_{max} yields

$$e_{max} = \frac{\ln(t_2/t_1)}{t_2 - t_1} \tag{102}$$

From the above relationship, the emission rate at the peak maximum is obtained as a function of the gate times t_1 and t_2. If the temperature of the peak maximum, T_m, is noted for several sets of gate times t_1 and t_2, then equation (93) may be used to determine the activation energy. If the pre–exponential factor in equation (93) is assumed to have a temperature dependence of T^2 (i.e. constant S), then a plot of $\ln(e/T^2)$ versus $1/T$ is expected to be a straight line of slope $-E/k$.

It is possible to obtain the trapped electron concentration n_0 by substituting equation (102) for e in equation (100) and solving for n_0. Thus we have

$$n_0 = \frac{2N_d\Delta C_{max}}{A}\sqrt{\frac{2(V_d - V_a)}{q\epsilon N_d}}\frac{r^{r/(r-1)}}{r-1} \tag{103}$$

where ΔC_{max} is simply the value of ΔC at the peak maximum and $r = t_2/t_1$. In the case of a saturating fill pulse, $n_0 = N$ so that equation (103) gives us the total trap concentration N.

Capture Cross Section

During a fill pulse, a charge carrier spends an average time of τ_c in the depletion region before being captured. Thus it is implied that the traps fill according to the relation

$$n(t) = N\left(1 - \exp\left(\frac{-t}{\tau_c}\right)\right) \tag{104}$$

where τ_c is the capture lifetime.

Consider a fill pulse of width t_f which fills some fraction of the trap levels according to equation (104). Since the intensity of the DLTS signal depends on the concentration of trapped electrons which are released following a fill pulse, we may substitute $\Delta C(t_p)$ and $\Delta C(\infty)$ for $n(t)$ and N in equation (104). $\Delta C(\infty)$ is

the value obtained for ΔC under the influence of a saturating fill pulse. Making these substitutions, and solving equation (104) for τ_c, leads to

$$\tau_c = \frac{\tau_p}{\ln\left(\frac{\Delta C(\infty)}{\Delta C(\infty)-\Delta C(t_p)}\right)}. \tag{105}$$

Plotting the numerator versus denominator of equation (105) results in a straight line of slope τ_c. When evaluating τ_c this way, caution should be used to ensure that the fill pulse width τ_p is small compared to a saturating fill pulse. If τ_p is too large then a significant fraction of the traps become filled which results in an increase in τ_c, thus τ_c becomes time dependent and the plot no longer yields a straight line. Once τ_c has been determined, the capture cross section is evaluated using equation (95).

The evaluation of the capture cross section, unfortunately, requires knowledge of the free carrier concentration n. In the case of a majority carrier trap it is generally assumed that all of the donors (or acceptors) are ionized, thus $n \approx N_d$ (or N_a). Recall that the ionized donor concentration may be determined from a plot of $1/C^2$ versus voltage (Eqn. (86)).

In the case of minority traps in a p–n junction, the minority carrier concentration is given by Lang[57] as

$$n = \frac{\gamma L}{qAD} I \tag{106}$$

where γ is the minority carrier injection efficiency, L is the diffusion length, q is the electronic charge, A is the junction area, D is the diffusion coefficient and I is the injection current measured during the fill pulse. Thus, for minority traps, a great deal of knowledge of the electrical characteristics is required.

A frequently used method for calculating the capture cross section for a minority trap is to employ equation (93) after determining the emission rates and activation energy.

CHAPTER V

DLTS EXPERIMENTS

Sample Preparation

The sample used in this DLTS study was an SPVT Schottky diode. Since p–type ZnSe is not readily available it was not possible to obtain a p–n junction for study. The Schottky diode was not fabricated from an as grown sample. The as grown sample was treated in molten zinc to reduce the resistivity and promote n–type conductivity. This zinc treatment process is usually referred to as zinc extraction. It is believed that the treatment causes zinc diffusion into the sample which displaces substitutional impurities on zinc sites and also fills zinc vacancies. Following this treatment, the sample was fitted with two electrodes; a gold ohmic contact and a platinum Schottky contact. Both of these electrodes are on the same side of the sample.

The Schottky diode has a low enough resistivity that characterization using DLTS is possible. For high resistivity samples, DLTS is impractical since the carrier concentration is too low to give rise to large changes in the junction capacitance.

Experimental Apparatus

All measurements were made using a Bio–Rad model DL–4600 DLTS system. A block diagram for this system is shown in Fig. 33. The following discussion describes the overall operation of the system.

When performing DLTS measurements, the sample is mounted on a cold finger in a vacuum insulated cryostat. The sample is cooled with liquid nitrogen which is pumped from a storage dewar, circulated through the base of the cold

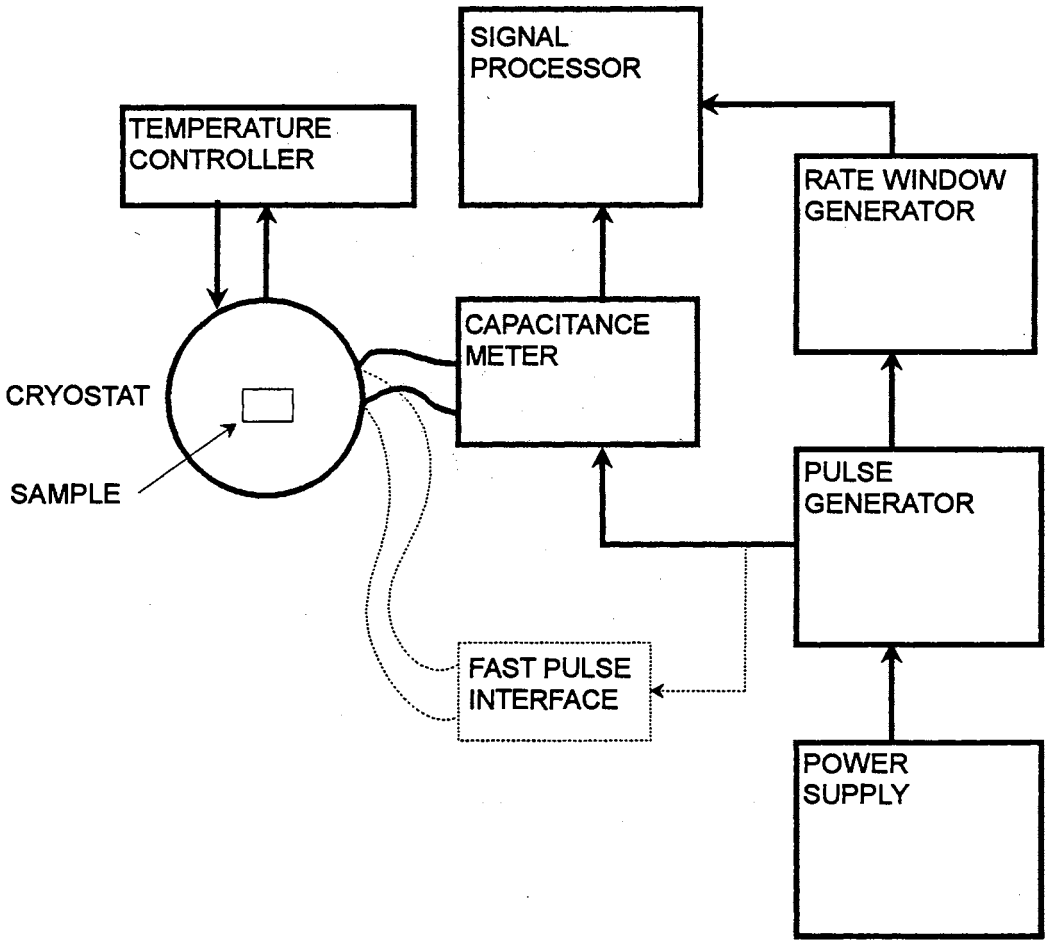

Figure 33. Block diagram of Bio–Rad DLTS system

finger and returned to the storage dewar. Electrical contacts to the sample are made by positioning needle shaped probes over both electrodes. Positioning of the probes is facilitated by mounting them on x–y–z translation stages.

External connections to the cryostat probes are connected to a Boonton capacitance meter which has been modified (by Bio–Rad) to improve response time. The capacitance meter measures the impedance (Z) of the junction when subjected to a low voltage, 1MHz signal. The junction capacitance is calculated as $C = 1/\omega Z$ where ω is the angular frequency (2πMHz). Output from the capacitance meter is analyzed by a signal processor which performs sampling and signal averaging.

The power supply and pulse generator together maintain a reverse bias and provide fill pulses. Following a fill pulse, the rate window generator provides a series of three timing pulses which instruct the signal processor to begin a measurement. The three timing pulses (at times t_1, t_2 and t_3) cause the signal processor to take a measurement at three points along the capacitance transient. The signal processor then outputs the two DLTS signals $\Delta C_A = C(t_2) - C(t_1)$ and $\Delta C_B = C(t_3) - C(t_2)$. Thus, this system generates two DLTS curves in a single temperature sweep. The 'rate window' of each DLTS curve is simply the value of the emission rate at the peak maximum as defined by equation (102). The rate windows which are generated simultaneously are summarized in Table IV. Note that the ratio of timing pulses for each rate window is a constant, that is $r = t_2/t_1 = t_3/t_2 = 0.4016$ for each rate window pair.

Since the capacitance meter operates at 1MHz, the interconnections between the power supply/pulse generator and the capacitance meter are filtered to reject the 1MHz signal. This creates a problem when DLTS is to be measured using fill pulses on the order of 1μs since the filter circuit prevents these pulses from reaching the sample. The fast pulse interface shown in Fig. 33 corrects this problem by removing the capacitance meter (and filter) from the circuit for the duration of the fill pulse.

Control of the DLTS system is accomplished by an HP–9000 computer connected via an IEEE–488 interface bus.

Results

Capacitance–Voltage Analysis

After mounting the sample, the quiescent capacitance was measured as a function of the reverse bias voltage from 0 to 9v. As shown in Fig. 34a, the quiescent capacitance ranges from about ~13.5pF at zero reverse bias down to ~6.5pF at 9v. In part b of this figure we see that the plot of $1/C^2$ versus reverse bias gives rise to a straight line, indicating that the trap concentration in the depletion region is uniform. From the slope of the $1/C^2$ versus V plot and from equation (86) a donor concentration of $N_d \approx 6.3 \times 10^{14}\text{cm}^{-3}$ is obtained (there is a small dependence upon V, but it will be ignored). Substitution of N_d into equation (84) indicates that the depletion width may be varied from 2μm at 0v to 4μm at 9v.

DLTS Analysis

A typical DLTS spectra for the ZnSe Schottky diode is shown in Fig. 35a. The data were obtained with a reverse bias of 2v and a 0v, 2ms fill pulse. The spectra appears to contain a single electron trap. From a plot of $\ln(e/T^2)$ verses $1/T$ (Fig. 35b) the trap depth was estimated to be 0.329eV. As is seen in the figure, there is significant variation in peak height with varying rate window; in

TABLE IV.

RATE WINDOWS USED IN BIO-RAD DLTS SYSTEM

Rate windows	Timing signals		
A/B (s^{-1})	t_1(ms)	t_2(ms)	t_3(ms)
1000/400	0.614	1.53	3.81
200/80	3.06	7.62	18.97
50/20	12.2	30.4	75.6
10/4	61	152	378
2/0.8	306	762	1897

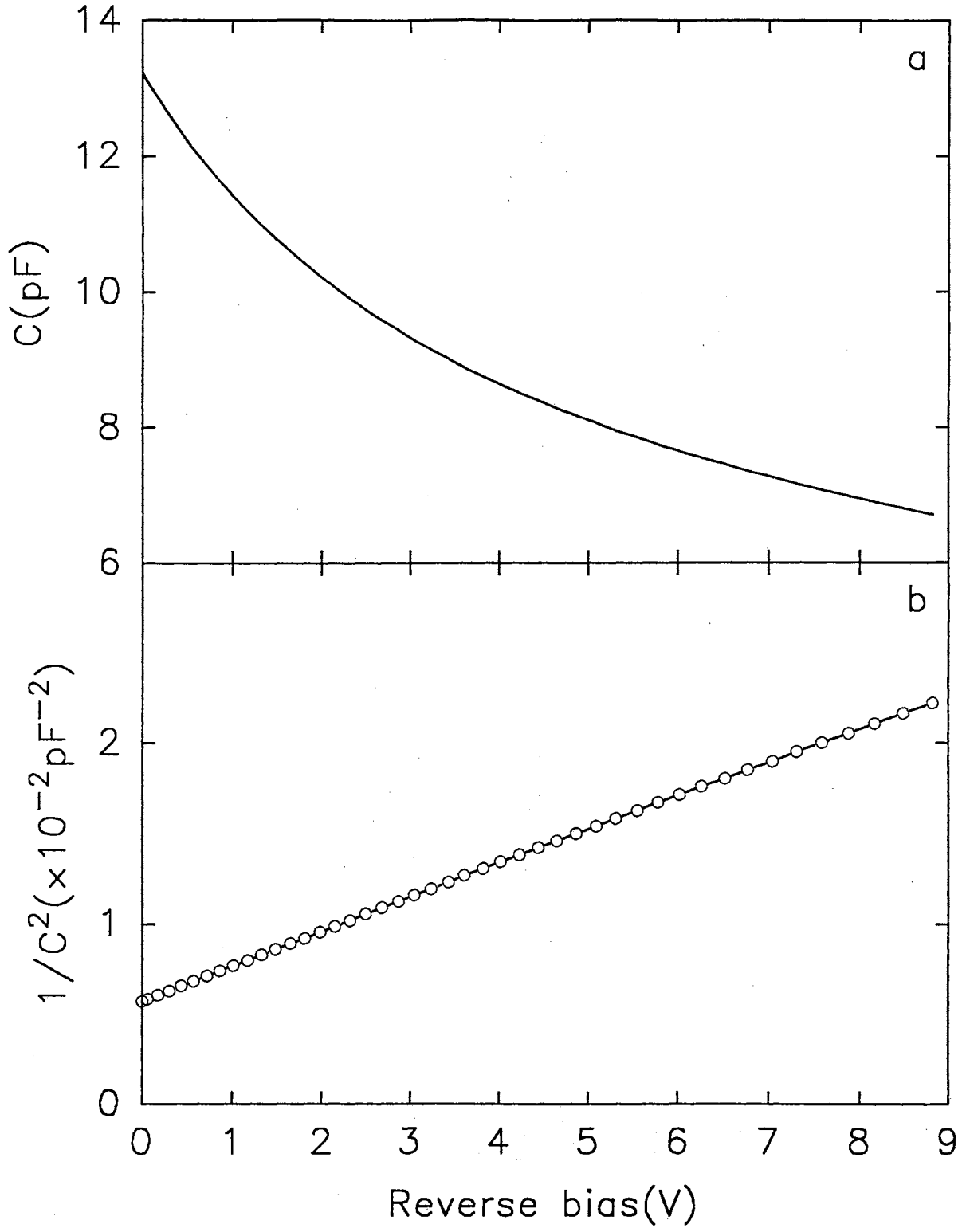

Figure 34. Capacitance as a function of reverse bias voltage (a); and (b) plot of $1/C^2$ versus reverse bias (slope of plot gives donor concentration). Data were taken at 300K.

general, this type of behavior is not expected. It has been shown[66] that strong electric fields in the depletion region may enhance the thermal emission rate(Poole-Frenkel effect). Zhao *et al.*[67] observe that such effects may cause variations in the DLTS peak heights as seen in Fig. 35. Zhao *et al.* point out that if large peak height variations are seen for both large and small reverse bias voltages then field enhanced emission is not significant. With this idea in mind, DLTS measurements were repeated with a reverse bias of 8v. The repeated DLTS measurement resulted in nearly identical variations in peak height and an activation energy of 0.329eV; exactly the same value obtained for a reverse bias of 2v. Thus, the effects of field enhanced emission are negligible.

By applying equation (103) at the peak of the 1000/s rate window, trap concentrations (N) of $8.5 \times 10^{12}\text{cm}^{-3}$ and $1.8 \times 10^{12}\text{cm}^{-3}$ are obtained for the 2v and 8v spectra, respectively. Recall that the derivation of the capacitance transient equations in the previous chapter depend on the approximation $N \ll N_d$. In the data presented here this inequality is well satisfied.

When preparing to analyze the capture cross section for the observed peak, DLTS was performed with short fill pulses (1μs). As shown in Fig. 36a the DLTS peak height is reduced by approximately a factor of 10. We also notice that the DLTS spectrum is not composed of a single peak but rather several overlapping peaks. These additional peaks were found to saturate for short fill pulses whereas the larger peak does not saturate until the fill pulse width is on the order of a few milliseconds. Activation energy plots for the two major peaks (labeled A and B) are shown in Fig. 36b. Notice that the value of the activation energy for peak A (the larger peak) is 0.342eV. This is higher than previously calculated and the difference is attributed to peak overlap. Note, however, that the difference is only about 3%. The energy calculated for peak B is 0.225eV.

As outlined in chapter IV, the capture cross section of a trap is calculated by varying the fill pulse width and observing the changes in the DLTS peak height (see Eqn. (105)). Unfortunately, the smaller peaks which appear in Fig. 36a saturated for fill pulses of $\sim 0.1\mu$s. Since these pulse widths represent the lower limit of

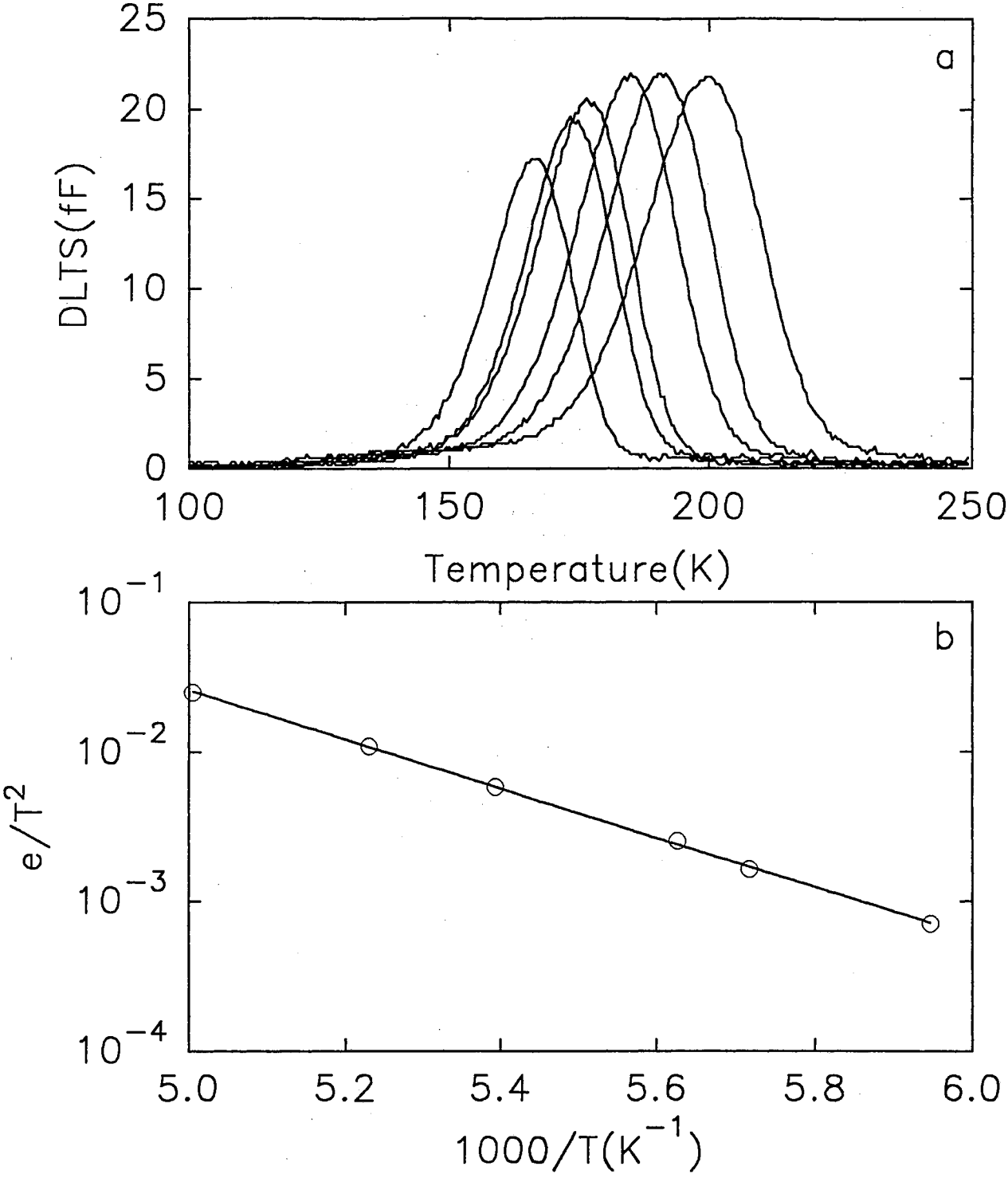

Figure 35. DLTS taken at 2v reverse bias with a 2ms ,0v fill pulse. Quiescent capacitance level is 10pF. Figure shown (a) DLTS curves obtained for rate windows of 1000, 400, 200, 80, 50 and 20/s; (b) activation energy plot yields trap depth of 0.329eV.

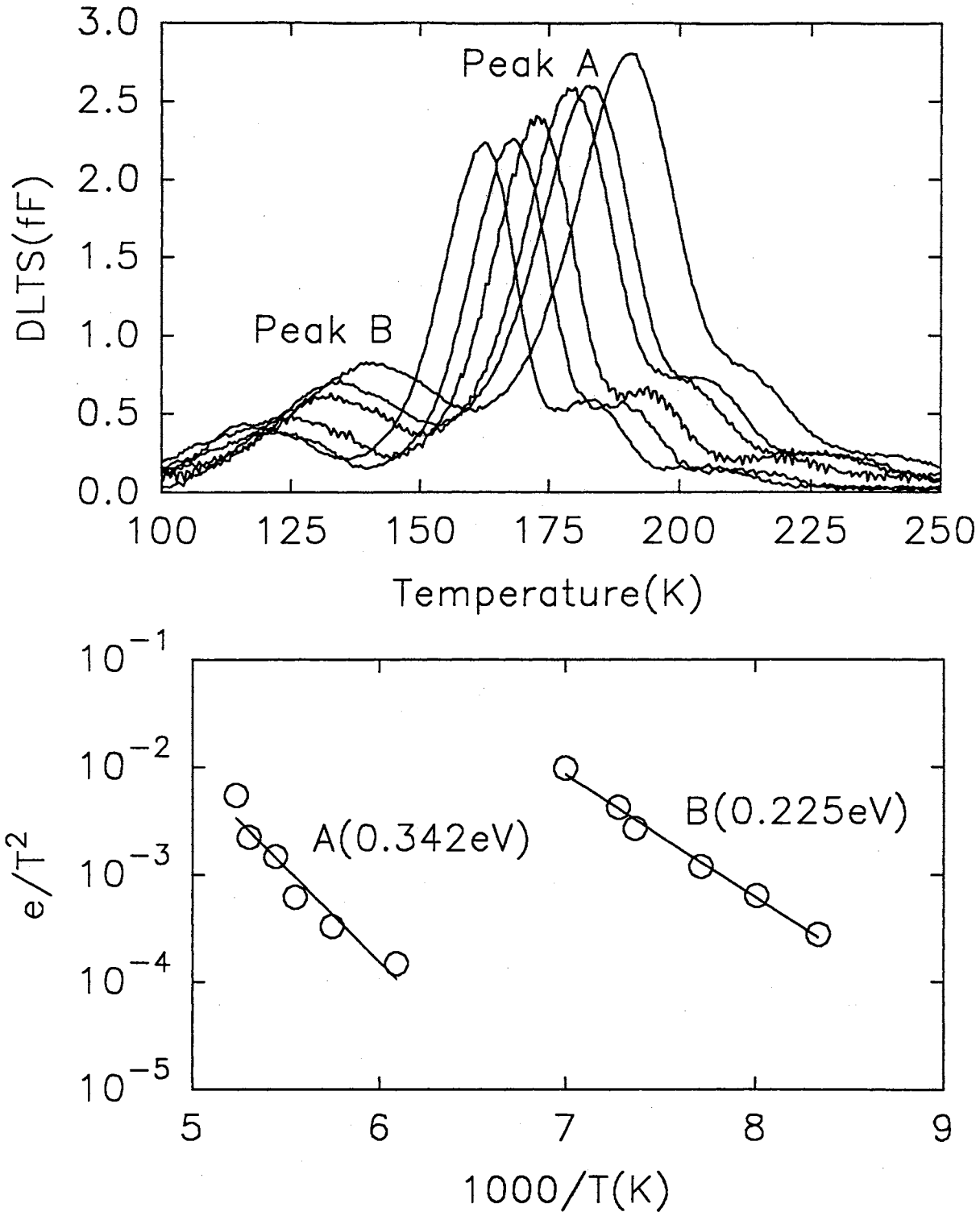

Figure 36. DLTS spectra for ZnSe Schottky diode for 1μs fill pulse. The figure shows (a) DLTS spectra obtained for rate windows of 200, 80, 50, 20, 10 and 4/s. The graph reveals the presence of several overlapping peaks; (b) activation energy analysis of the two major peaks A and B.

the system used, capture cross section analysis could not be performed on these peaks. The larger peak, however, did not present this problem and was analyzed as follows. DLTS data were taken for fill pulses of 2, 4 ,6 8 and 10μs. Each of these data sets contains 3 rate window pairs giving a total of 6 rate windows in the range from 200/s down to 4/s. By analyzing the peak height variations versus fill pulse width for a particular rate window, we may evaluate the capture cross section at the temperature of the peak maximum for that rate window. Since the peak maximum occurs at a different temperature for each rate window, the capture cross section is evaluated at 6 different temperatures. These calculations were complicated by a significant amount of baseline drift as a function of fill pulse width. This shift was corrected by zeroing the baseline on each data set. It is believed that the drifting baseline is due to the less than ideal characteristics of the Schottky contact.

Figure 37a shows the results obtained by plotting the data for the individual rate windows according to equation (105). The resulting capture cross sections are shown in Fig. 37b. Due to the short pulses used in this analysis, it was necessary to use the fast pulse interface, thus, the 1000/400 rate window pair was not used.

An attempt was made to fit the capture cross section curve shown in Fig. 37b to a power law temperature dependence (see Eqn. (66)). This attempt yielded a capture cross section of $6 \times 10^{-21} \mathrm{T}^2 \mathrm{cm}^2$. The quality of the fit was quite poor and we also notice that the fitted value for the temperature dependence parameter, b, is at the lower limit of its allowed range (i.e. $b = 0$). Thus, the capture cross section is not well described by a power law temperature dependence. Another commonly used parameterization of the capture cross section is

$$S(T) = C \exp\left(\frac{-E_b}{kT}\right) \tag{107}$$

where E_b is the height of a barrier which electrons must overcome in order to be captured. This type of capture cross section often arises in the case of trapping

centers which undergo a large lattice relaxation following electron capture or emission. The resulting fit is shown as the solid line in Fig. 37b and the resulting parameters are $E_b = 0.087\text{eV}$ and $C = 5.45 \times 10^{-14}$.

Curve Fitting

Most published analysis using the method of DLTS uses the traditional methods discussed above. Curve fitting has not been used for DLTS possibly due to concerns about the difficulty involved in writing software to perform fitting as well as concerns about computation time. However, with faster computers and more advanced software these concerns seem unnecessary.

In order to fit a DLTS curve, equation (100) must be fully parameterized. Begin by defining a constant A_1 such that equation (100) becomes

$$\Delta C(T; t_1, t_2) = A_1 \left[\exp(-t_1 e(T)) - \exp(-t_2 e(T))\right] \tag{108}$$

where the temperature dependence has been explicitly indicated. The thermal emission rate $e(T)$ is evaluated according to equation (93). Fitting was performed using both the power law (Eqn. (66)) and the exponential (Eqn. (107)) temperature dependence for the capture cross section. In the following discussion power law and exponential cross sections will be referred to as S_A and S_B, respectively. When using equation (107) for $S(T)$, the emission rate becomes

$$e = N_D v_{th} C \exp\left(\frac{-E_b}{kT}\right) \exp\left(-\frac{E}{kT}\right) \tag{109}$$

$$= N_D v_{th} C \exp\left(\frac{-E'}{kT}\right) \tag{110}$$

where E' represents the sum of the trap depth E and the barrier height E_b. Thus, from fitting we cannot separate the values of E and E_b. If, however, we combine fitting results (E') with the results from the previous section (E_b), it is possible to obtain the actual trap depth E.

Fitting the DLTS spectra shown in Fig. 36 to a composite of six overlapping peaks defined by equation (108) resulted in the deconvolution of peaks shown in

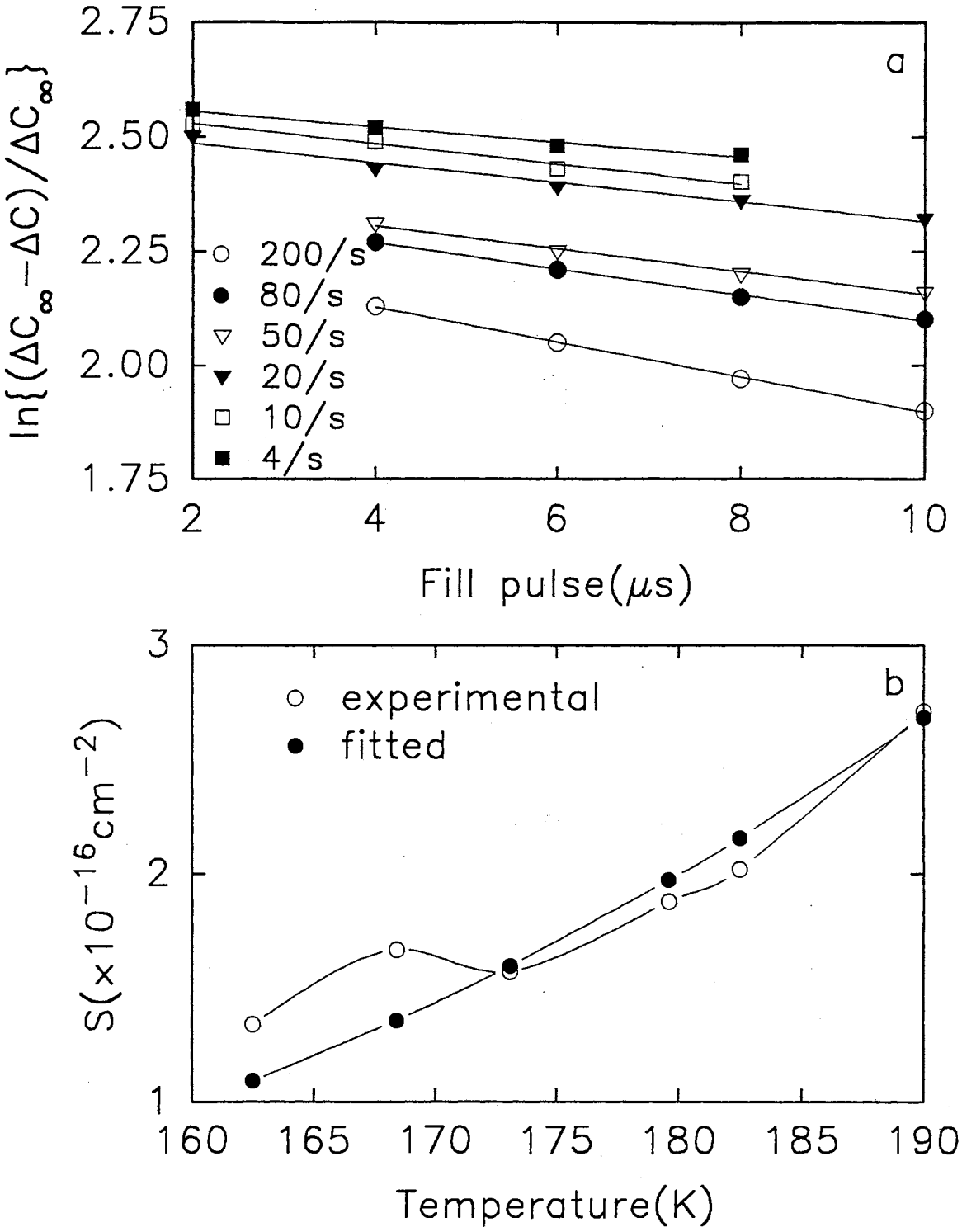

Figure 37. Capture cross section analysis for several rate windows. The figure shows (a) normalized DLTS versus fill pulse width for 200, 80, 50, 20, 10 and 4/s rate windows; (b) Open circles represent values calculated from slopes in (a) and solid circles represent best fit to equation (107).

Fig. 38). Fits using both $S_A(T)$ and $S_B(T)$ resulted in nearly identical values for χ^2; 0.02040 and 0.0242, respectively. The peak shapes and positions for these fits are also nearly identical, thus, only the fit for which $S(T) = S_A(T)$ is shown. The fitting results are shown in table V. Two activation energies are given for peak 4; the first value is E' and the value in parenthesis is $E = E' - E_b$. Also included in the table are the trap concentrations calculated from equation (103). Since peaks 1, 2, 3, 5 and 6 are saturated, the values given in the table are the actual concentrations. For peak 4, however, the value given is smaller than the actual concentration since trap is not saturated under these conditions.

Capacitance Transient Capture

By attaching a LeCroy model 9400A oscilloscope to the output of the capacitance meter it was possible to observe the capacitance transients. The oscilloscope was interfaced to an IBM–PC for the purpose of downloading the capacitance transients at even temperature intervals. The transients were zeroed at $t = 0$ and fitted to the simple exponential relationship of equation (99) in order to obtain

TABLE V.

PARAMETERS OBTAINED FROM FITTING DLTS DATA

		Trapping Parameters			
Peak No.	$S(A$ or $B)$	E(eV)	C	b	$N(\mathrm{cm}^{-3})$
1	A	0.087	4.52×10^{-17}	1.06	8.92×10^{10}
	B	0.096	9.20×10^{-15}	*	9.03×10^{10}
2	A	0.127	1.89×10^{-15}	1.61	3.04×10^{11}
	B	0.132	1.97×10^{-14}	*	3.04×10^{11}
3	A	0.229	6.70×10^{-13}	1.70	7.61×10^{10}
	B	0.231	3.49×10^{-12}	*	7.82×10^{10}
4	A	0.334	1.99×10^{-12}	1.06	1.01×10^{12}
	B	0.350(0.263)	7.16×10^{-10}	*	1.01×10^{12}
5	A	0.360	3.99×10^{-13}	0.88	2.63×10^{11}
	B	0.383	5.54×10^{-10}	*	2.61×10^{11}
6	A	0.325	1.00×10^{-8}	3.46	9.38×10^{10}
	B	0.293	6.76×10^{-13}	*	9.39×10^{10}

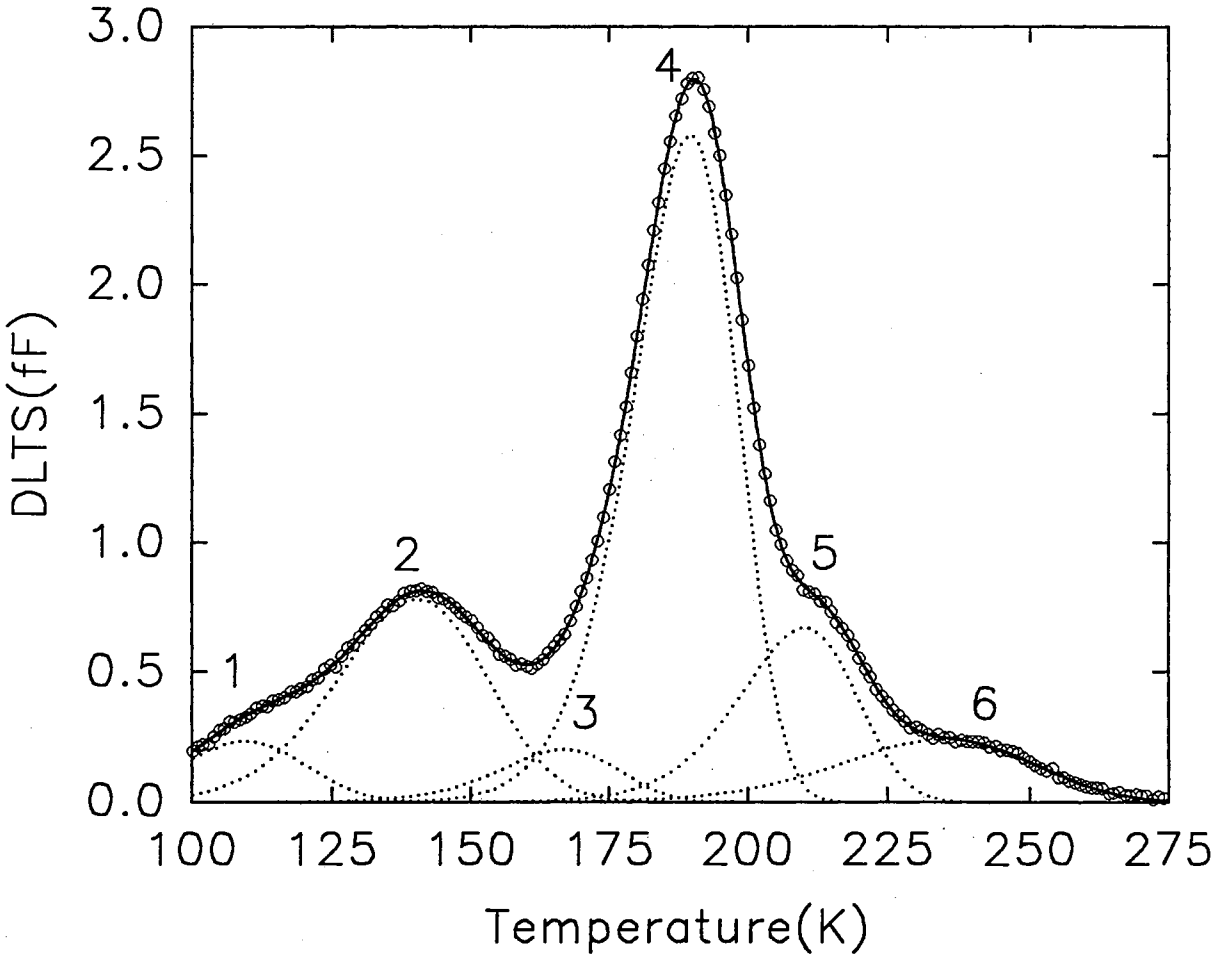

Figure 38. Deconvolution of DLTS spectra by fitting to 6 overlapping peaks as defined by equation (108). The resulting parameters are given in table V

the emission rate. Thus, by capturing transients at several temperatures one may calculate the activation energy from a plot of $\ln(e/T^2)$ versus $1/T$. By capturing transients at intervals of 2K between 178K and 210K, this process yielded an activation energy of 0.331eV. The capacitance transients were well described by the simple exponential decay relationship. Fig. 39a shows the evolution of the capacitance transient from low to high temperatures. The resulting activation energy plot is shown in Fig. 39b.

Obvious drawbacks to this method are the large amount of data generated (approximately 1000 points per transient) and the time and effort required to perform the fitting. A definite advantage, however, is the fact that capturing transients allows for the characterization of a trap in a single temperature sweep (i.e. multiple measurements with different rate windows are not required). If adequate hardware and software modifications are implemented, a great deal of the process may be automated.

Optical DLTS

As already mentioned, it is not possible to observe minority carrier peaks in the spectrum of a standard DLTS experiment using a Schottky diode. In order to observe minority carrier traps we must obviously generate minority carriers. In a p–n junction this is done by forward biasing the junction to cause minority carrier injection. In a Schottky diode, however, minority carriers are generated via optical excitation with light of energy greater than the band–gap. This excitation will also generate majority carriers, most of which will be swept out of the depletion region and some of which will be trapped. Thus when measuring the 'optical' DLTS (ODLTS) spectra, both electron and hole traps will be observed.

The experimental setup for ODLTS, shown in Fig. 40, is the same as that described for DLTS except for two additional pieces of equipment; (1) a Spectra Physics argon ion laser and (2) a Newport model N35085-05 acousto–optic modulator (AOM). The AOM was used to modulate the laser beam which was focused

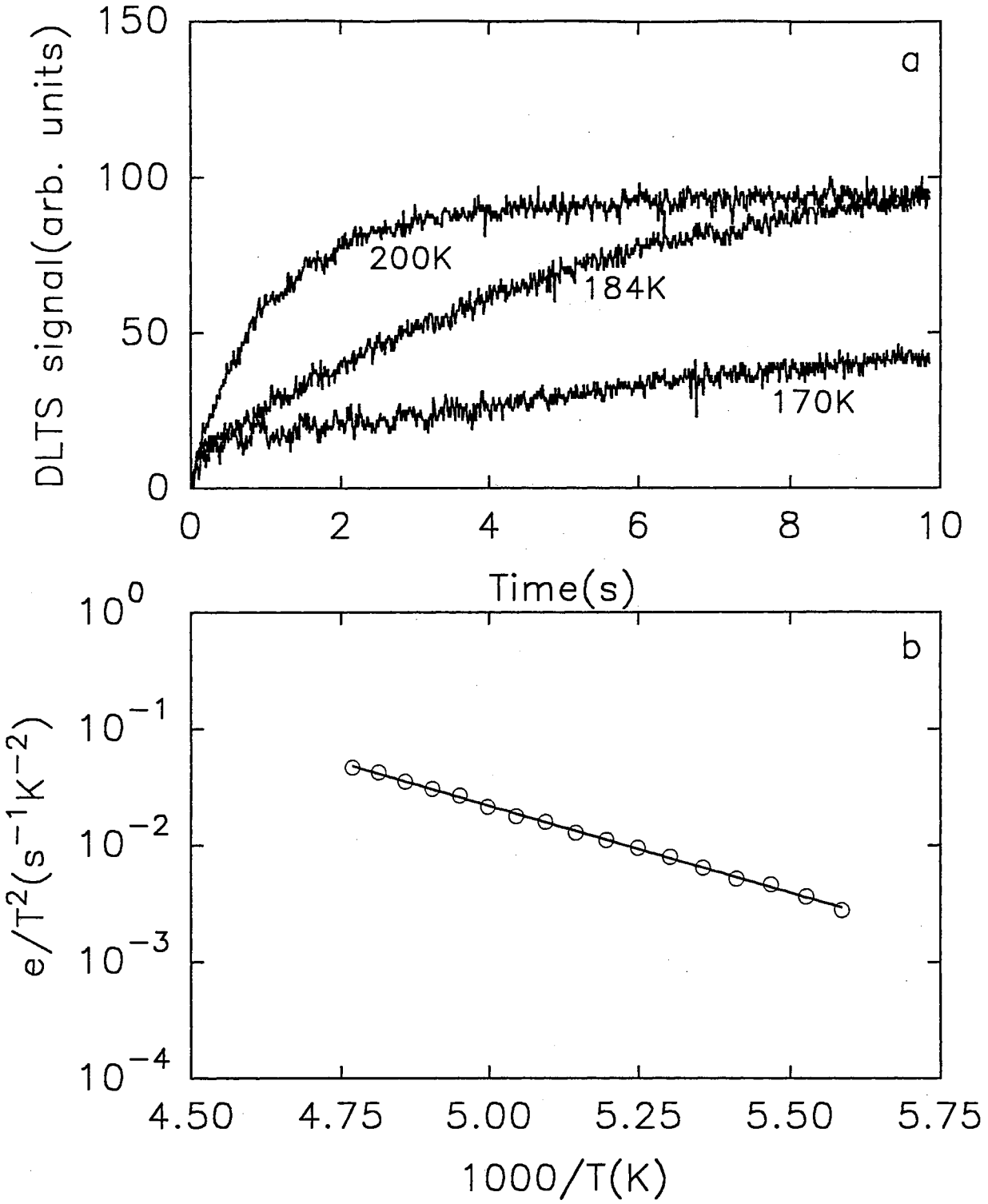

Figure 39. Data from DLTS capacitance transient capture. (a) capacitance transients for low, intermediate and high temperatures; (b) activation energy plot resulting from fitting each transient to Eqn. (99) to obtain the emission rate e. The resulting activation energy is 0.331eV.

on the Schottky junction. The electrical fill pulse was replaced with an optical fill pulse by using the fill pulse output of the pulse generator to trigger the AOM.

Results for ODLTS were found to be inconsistent and difficult to analyze due to a large offset in the DLTS baseline. Since a DLTS measurement reports only the relative change in capacitance rather than the magnitude of the capacitance, baseline correction is very difficult. The ODLTS spectrum shown in Fig. 41 is somewhat typical of the spectra obtained. One of the major problems is the position of the baseline. If the baseline is placed at BL–1 then point A is a valley and points B and D are majority carrier trap peaks. If the baseline is, instead, placed at BL–2, then point A is a minority carrier trap peak, C is a valley and points B and D are again majority trap peaks. Thus one can choose a number of baselines and analyze the data accordingly. There does seem to be a correlation between some of the peaks observed here and the overlapping peaks observed in standard DLTS for short fill pulses, this may be an indication that there are no minority traps to be observed. The latter case, while being somewhat uninteresting from the viewpoint of an experimentalist, does have a positive implication; the zinc extraction process was effective in removing deep hole traps.

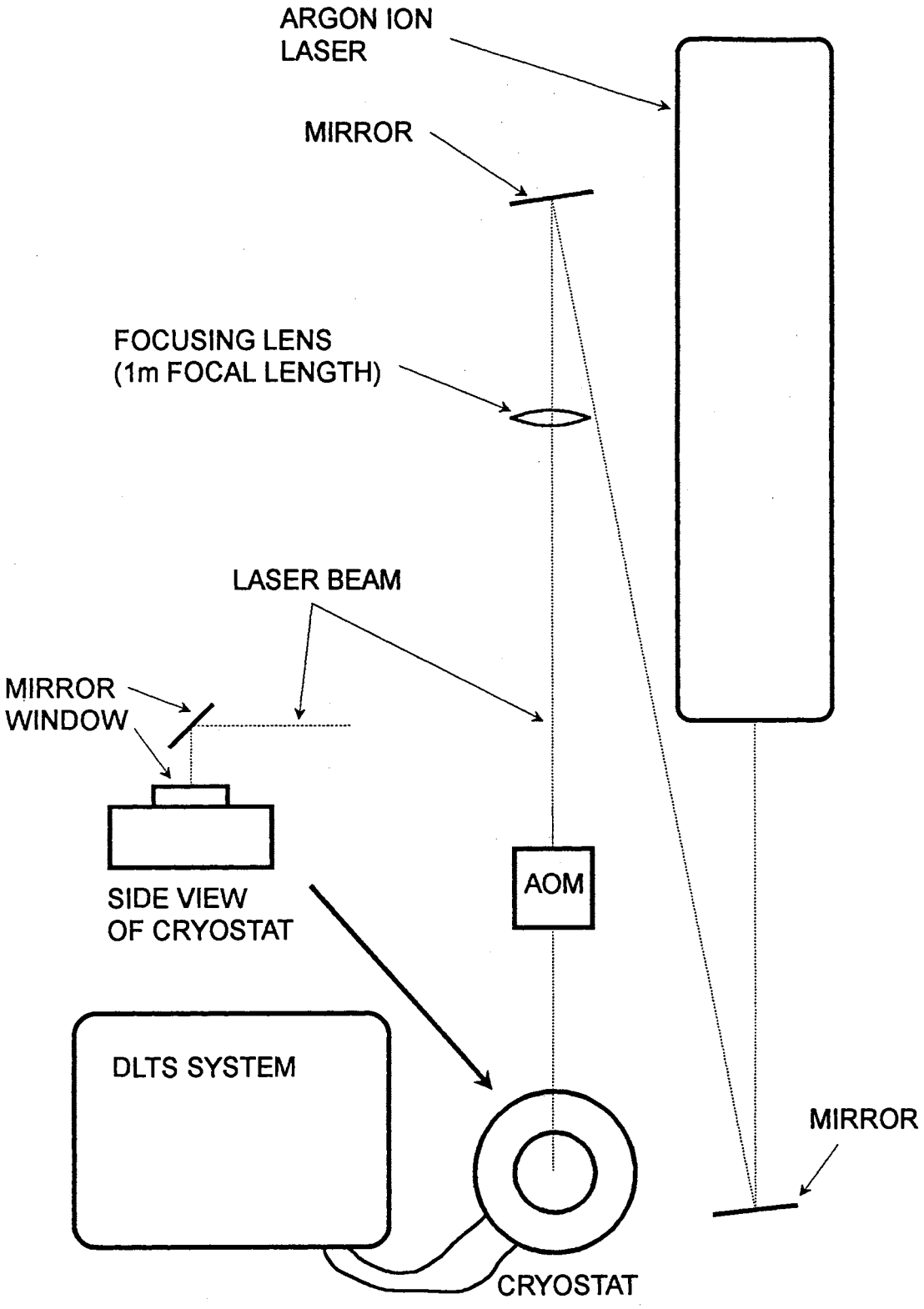

Figure 40. Block diagram of optical DLTS experimental setup.

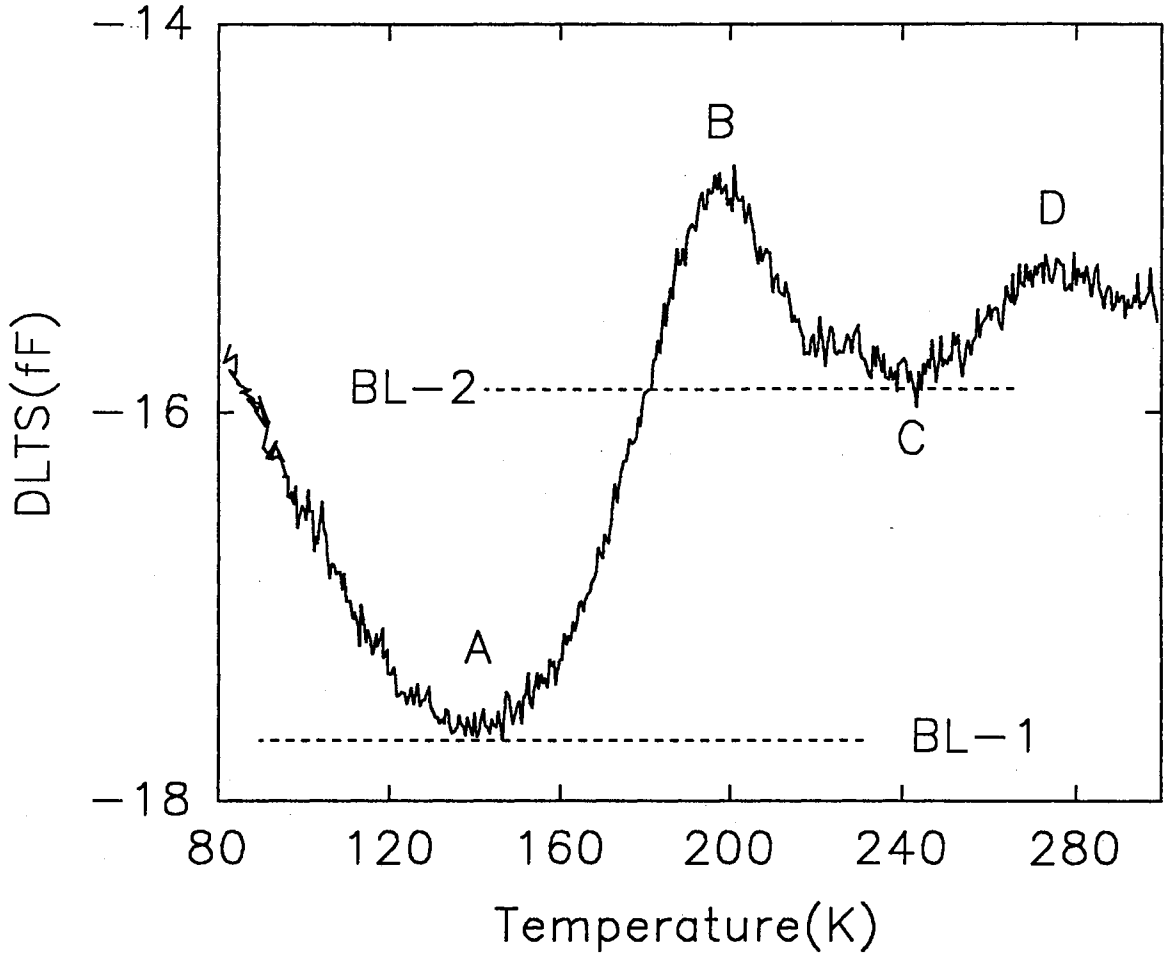

Figure 41. Optical DLTS spectra for Schottky diode. Date were taken with 100μs laser pulses at 25mW (CW power) and a reverse bias of 2v. Rate window used was 1000/s.

CHAPTER VI

SUMMARY AND CONCLUSIONS

Discussion and Conclusions

The two trap levels in the as grown SPVT samples which are of particular interest are the hole traps at 0.71eV and 0.33eV above the valence band (see Table II). Stringfellow and Bube [44] and Wang and Fan [68] report that the hole state responsible for red emission at 1.97eV is 0.7 to 0.72eV above the valence band. Wang and Fan also report a hole trap at 0.3eV above the valence band which is believed to be the recombination center associated with the green emission at 2.25eV. It is generally accepted that these hole traps are related to Cu_{Zn} (i.e. copper substituting for zinc). The hole centers near 0.7eV and 0.3eV are thus referred to as the Cu_{red} and Cu_{green} centers respectively. The above results also agree with the findings of other authors reporting on MG samples [69,46,70]. From the data presented here it is inferred that the 0.33 and 0.71eV TSC peaks are caused by hole release from the Cu_{green} and Cu_{red} centers, respectively.

Spark source mass spectrograph analysis of the SPVT and MG samples indicates that they contain equal concentrations of copper (0.2ppm) which raises the question of why no TL is observed from the SPVT samples. Furthermore, since we observe TSC from the release of holes from the copper centers in the SPVT samples one might ask why we do not observe TSC with the same activation energy, and corresponding peak position, from the MG samples?

Based on TSC and TL results a model is developed for the TSC and TL processes in both SPVT and MG samples. This model describes the role of the Cu_{red} and Cu_{green} centers as well as providing explanations for the lack of TL from the SPVT samples.

It was shown, for the MG samples, that TSC due to the release of electrons is seen over the entire temperature range of interest (see page 55). TL is also seen in this temperature range and it is believed that the TL is also due to the release of electrons, from states between approximately 0.2 and 0.7eV below the conduction band, which recombine with holes in recombination centers (e.g. Cu_{red}). These levels have been reported by several authors in MG ZnSe [46,71,45,72]. Emission spectra reported by Hitier et. al. [45] show that the TL emission from MG ZnSe arises from electrons recombining with holes trapped at the Cu_{Zn} centers. It is know from impurity analysis [16], PL analysis (see Fig. 21) and TSC analysis that the Cu_{Zn} centers are also present in the SPVT samples; lack of TL, therefore, must be due to the lack of localized states from which electrons could be thermally released in the temperature range of these experiments.

TSC due to hole release from the Cu_{red} center is not observed in the MG samples since the holes act as recombination sites for detrapped electrons, producing TL. We saw, from the TL emission spectra, that the Cu_{green} center does not act as a recombination center during TL (i.e. no green emission). Hole release from these centers may in fact give rise to TSC in the MG samples but remain hidden in the complex structure of overlapping peaks.

From photoconductivity and illumination wavelength dependent TSC and TL measurements it is seen that both sample types contain a variety of very deep to mid–gap levels. The compensation effect of these levels has been observed by Ohki *et al.*[48].

It has also been found that the red luminescence mechanism in both sample types involves a shallow donor at ~15meV (15.7meV for MG and 14.7meV for SPVT). This is in agreement with other reports[44,46]. The melt grown samples have also been found to contain a donor level at 45.7meV which is involved in the red luminescence mechanism after the 15.7meV donor quenches.

Fig. 42a shows a suggested energy level model for TSC and TL in the MG samples. Transitions (1) followed by transitions (2) and transitions (3) will give rise to simultaneous TL and TSC. If, as in the SPVT samples, the corresponding

electron traps are absent then the holes trapped by the copper centers will not undergo recombination. In this case one observes TSC from the release of holes from these centers, and the measured activation energies of 0.33eV and 0.71eV (peaks 4 and 8 from in Table II). Fig. 42b shows the proposed energy level model for the SPVT samples. Notice that the SPVT sample does not contain an array of active electron centers but does contain deep centers as well as a shallow donor level.

DLTS analysis of a Schottky diode made from zinc extracted SPVT material has shown that there exists an electron trap between 0.3 and 0.35eV below the conduction band. This level has been reported to be a selenium vacancy[73] or a complex of a selenium vacancy and a residual impurity[74]. Miyajima *et al.*[75] agree with the idea of a vacancy/impurity complex and claim that the impurity is a gallium interstitial. This vacancy appears to be absent in the as grown material, thus appearing as a result of zinc extraction. There is a possibility that the zinc extraction process has introduced a gallium impurity but this possibility has not yet been investigated. Deep hole traps appear to have been effectively removed by the zinc extraction process.

The above model provides a consistent explanation for the primary features which have been observed in this research. The model provides a clear justification for the differences in TSC between SPVT and MG samples as well as the lack of TL in SPVT samples. There appears to be a significantly smaller concentration of deep states from which electrons could be thermally released in the SPVT material compared to the MG material. This may be beneficial to the use of the SPVT material as a superior quality zinc selenide for use as epitaxial substrates. Mid-gap defect states, however, still provide an effective compensation mechanism. It has also been observed that zinc extraction effectively removes many of the deep compensating centers such as Cu_{Zn}. With the removal of many deep centers, the resistivity of zinc extracted samples varied from 3 to 30Ωcm with corresponding free carrier concentrations on the order of $10^{14}cm^{-3}$. In general, for high quality n- or p-type semiconductors, one expects resistivities less than 1Ωcm and carrier

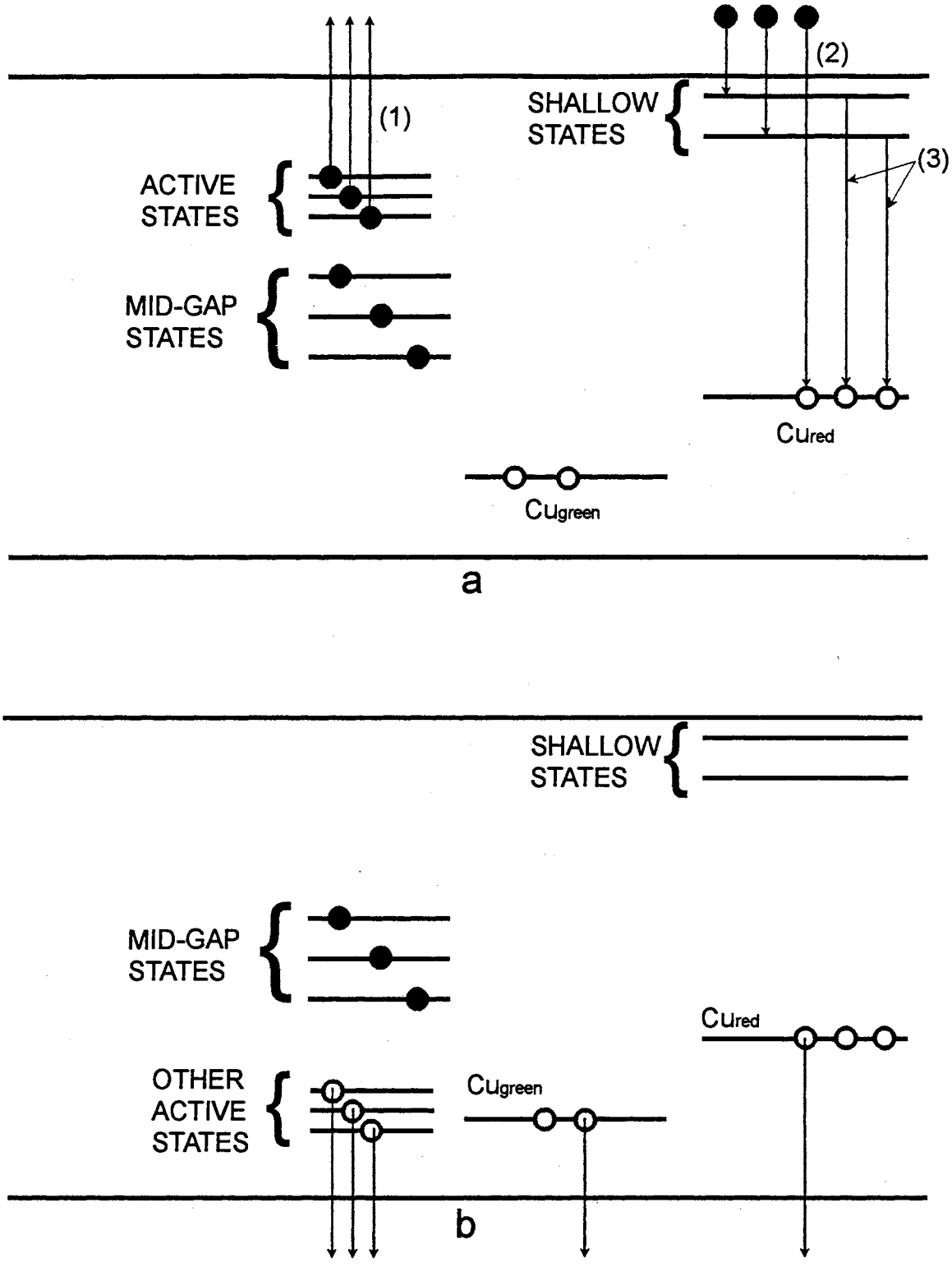

Figure 42. Proposed energy level diagram for (a) melt grown and (b) SPVT grown ZnSe. Deep active electron states appear to be absent in SPVT samples. Shallow and mid-gap levels, however, appear to be present in both MG and SPVT.

concentrations greater than $10^{18}cm^{-3}$. Thus, mid–gap defects may be an important cause for the inability to obtain high conductivity n– or p–type ZnSe.

Future Work

Although a great deal of effort has been made to better understand both the theoretical and experimental aspects of the work described in this thesis, there is still a great deal of work to be done.

The derivation of a new description of TSC and TL phenomena was presented along with results of computer modeling and comparison to older theoretical approaches. This modeling and testing may be expanded to cover a wider range of parameters. In this work variations in the temperature dependencies of the capture and recombination cross sections were not fully investigated. The generalized solution was also developed under the assumption of a single trap level. There are few real systems in which well isolated single TSC or TL peaks occur, thus it is usually assumed that overlapping peaks are merely a superposition of isolated peaks (i.e. they don not interact with oneanother). The generalized solution needs to be analyzed for its effectiveness in the case of multiple overlapping peaks. In this case a reexamination of the conditions for first–, second– and general–order kinetics would also be warranted.

We have also seen here that significant progress has been made in the development of bulk ZnSe. Further investigation is required to more fully understand the nature and origins of mid–gap levels. Since these levels form an effective compensation mechanism, it is necessary to identify methods for their removal. Further work is also necessary to understand the formation of the apparent selenium vacancy during zinc extraction. An attempt should be made to correlate the concentration of vacancies to the length of time the sample was treated in molten zinc. As each of these basic materials problems is overcome, the realization of efficient blue emitters, based on homoepitaxial growth of ZnSe, is one step closer to reality.

BIBLIOGRAPHY

1. H. Lozykowski, Czech. J. Phys. **B13**, 164 (1963).
2. M. Aven and D. A. Cusano, J. Appl. Phys. **35**, 606 (1964).
3. Y. S. Park, C. R. Geesner and B. K. Shin, Appl. Phys. Lett. **21**, 567 (1972).
4. T. N. Chin and L. A. Boyer, Solid State Electronics **16**, 143 (1973).
5. A. W. Livingstone, K. Turvey and J. W. Allen, Solid State Electronics **16**, 351 (1973).
6. H. Watanabe, T. Chikamura and M. Wada, Jap. J. Appl. Phys. **13**, 357 (1974).
7. M. Yamaguchi, A. Yamamoto and M. Kondo, J. Appl. Phys. **48**, 196 (1977).
8. J. Nishizawa, K. Itoh, Y. Okuno and F. Sakurai, J. Appl. Phys. **57**, 2210 (1985).
9. M. A. Haase, H. Cheng, J. M. DePuydt and J. E. Potts, J. Appl. Phys. **67**, 448 (1990).
10. J. Ren, K. A. Bowers, B. Sneed, D. L. Dreifus, J. W. Cook, Jr., J. F. Schetzina and R. M. Kolbas, Appl. Phys. Lett. **27**, 1901 (1990).
11. G. E. Thomas, Phillips Tech. Rev. **44**, 51 (1988).
12. R. N. Bhargava, J. Crystal Growth **117**, 894 (1992).
13. G. F. Neumark, J. Appl. Phys. **51**, 3383 (1980).
14. H. Cheng, J. M. DePuydt, M. Haase and J. E. Potts, Appl. Phys. Lett **56**, 848 (1990).
15. A. V. Nurmikko, R. L. Gunshor and M. Kobayashi, in *II–VI Compounds 1991: Proceedings of the Fifth International Conference on II–VI Compounds, Okayama, Japan, September 1991*, edited by S. Fujita, T. Nishino and T. Taguchi, page 433, Amsterdam, Netherlands, 1992, Elsevier Science Publishers B.V., also published in J. Cryst. Growth **117**, 432 (1992).
16. Gene Cantwell, W. C. Harsch, H. L. Cotal, B. G. Markey, S. W. S. McKeever and J. E. Thomas, J. Appl. Phys. **71**, 2931 (1991).
17. K. Ohkawa, A. Ueno and T. Mitsuyu, Jap. J. Appl. Phys. **30**, 3873 (1991).
18. M. L. Cohen and J. R. Chelikowski, *Electronic Structure and Optical Properties of Semiconductors*, volume 75 of *Springer Series in Solid State Sciences*, Springer–Verlag, second edition, 1989.

19. Charles Kittel, *Introduction to Solid State Physics*, John Wiley & Sons, Inc., New York, sixth edition, 1986.

20. K. W. Böer, *Survey of Semiconductor Physics*, Van Nostrand Reinhold, New York, 1990.

21. A. C. Lewandowski and S. W. S. McKeever, Phys. Rev. B **43**, 8163 (1991).

22. S. W. S. McKeever, B. G. Markey and A. C. Lewandowski, LUMDETR'91, Riga, Latvia, 1991, proceeding published in Nucl. Tracks Rad. Meas. (in press).

23. S. W. S. McKeever, A. C. Lewandowski and B. G. Markey , 10th International Conference on Solid State Dosimetry, Washington D.C., 1992, proceedings published in Rad. Prot. Dosim. (in press).

24. P. D. Townsend and J. C. Kelly, *Colour Centers and Imperfections in Insulators and Semiconductors*, Crane, Russak & Company, Inc, New York, 1973.

25. A. Halperin and A. A. Braner, Phys. Rev. **117**, 408 (1960).

26. J. T. Randall and M. H. F. Wilkins, Proc. Roy. Soc. (London) **A184**, 366 (1945).

27. P. N. Keating, Proc. Phys. Soc. (London) **78**, 1408 (1961).

28. Reuven Chen, J. Appl. Phys. **42**, 5899 (1971).

29. R. Chen and R. J. Flemming, J. Appl. Phys. **44**, 1393 (1973).

30. G. A. Dussel and R. H. Bube, Phys. Rev. **155**, 764 (1967).

31. Peter Bräunlich and Paul Kelly, Phys. Rev. B **1**, 1596 (1970).

32. M. Böhm and A. Scharmann, phys. stat. sol. (a) **4**, 99 (1971).

33. S. W. S. McKeever, *Thermoluminescence of Solids*, Cambridge University Press, Cambridge, 1985.

34. G. F. J. Garlick and A. F. Gibson, Proc. Phys. Soc. (London) **A60**, 574 (1948).

35. J. A. Partridge and C. E. May, J. Chem. Phys. **42**, 797 (1965).

36. Reuven Chen, J. Comp. Phys. **4**, 415 (1969).

37. A. C. Lewandowski, unpublished.

38. W. Chaney and D. Kincaid, *Numerical Methods and Computing*, Brooks/Cole Publishing Co, California, second edition, 1985.

39. S. W. S. McKeever and D. M. Hughes, J. Phys. D: Appl. Phys. **8**, 1520 (1975).

40. R. Chen , J. Appl. Phys. **40**, 570 (1969).

41. S. W. S. McKeever, phys. stat. sol. (a) **62**, 331 (1980).

42. S. G. Elkomoss, M. Samimi, S. Unamuno, M. Hage–Ali and P. Siffert, J. Appl. Phys. **61**, 2230 (1987).

43. C. Scharager, J. C. Muller, R. Stuck and P. Siffert, phys. stat. sol. (a) **31**, 247 (1975).

44. G. B. Stringfellow and R. H. Bube, Phys. Rev. **171**, 903 (1968).

45. J. Hitier, D. Curie and R. Vosicekas, J. Physique **42**, 479 (1981).

46. H. L. Oczkowski, phys. stat. sol. (a) **68**, 199 (1981).

47. A. G. Milnes, *Deep Impurities in Semiconductors*, John Wiley & Sons, New York, 1973.

48. A. Ohki, Y. Kawaguchi, K. Ando and A. Katsui, Appl. Phys. Lett. **59**, 671 (1991).

49. A. H. Booth, Can. J. Chem. **32**, 214 (1954).

50. W. Hoogenstraaten, Phillips Res. Reports **13**, 515 (1958).

51. R. Chen and S. A. A. Winer, J. Appl. Phys. **41**, 5227 (1970).

52. M. Schön, Z. Phys. **119**, 463 (1942).

53. M. Schön, J. Phys. Radium **17**, 689 (1956).

54. H. A. Klasens, Nature (London) **158**, 306 (1946).

55. R. Chen, V. K. Mathur, Joanne F. Rhodes, M. D. Brown, S. W. McKeever and R. K. Bull, phys. stat. sol. (a) **126**, 361 (1984).

56. S. W. S. McKeever, Joanne F. Rhodes, V. K. Mathur, R. Chen, M. D. Brown and R. K. Bull, Phys. Rev. B **32**, 3835 (1985).

57. D. V. Lang, J. Appl. Pys. **45**, 3014 (1974).

58. D. V. Lang, J. Appl. Phys. **45**, 3023 (1974).

59. Richard Williams, J. Appl. Phys. **37**, 3411 (1966).

60. C. T. Sah, W. W. Chan, H. S. Fu and J. W. Walker, Appl. Phys. Lett. **20**, 193 (1972).

61. C. T. Sah and J. W. Walker, Appl. Phys. Lett. **22**, 384 (1973).

62. C. H. Henry, H. Kukimoto, G. L. Miller and F. R. Merritt, Phys. Rev. B **7**, 2499 (1973).

63. R. H. Bube, *Electrons in Solids*, Academic Press, Inc., San Diego, 1988.

64. L. Solywar and D. Walsh, *Lectures on the electrical Properties of Materials*, Oxford University Press, New York, 1988.

65. D. K. Schroder, *Semiconductor Material and Device Characterization*, John Wiley & Sons, Inc., New York, 1990.

66. G. Vincent, A. Chantre and D. Bois, J. Appl. Phys. **50**, 5484 (1979).

67. J. H. Zhao, T. E. Schlesinger and A. G. Milnes, J. Appl. Phys. **62**, 2865 (1987).

68. S. Wang and X. W. Fan, J. Lumin. **40,41**, 802 (1988).

69. J. P. Fillard and J. P. Jasiot, phys. stat. sol. (a) **32**, K85 (1975).

70. S. Satoh and K. Igaki, Jap. J. Appl. Phys. **19**, 485 (1980).

71. J. Hitier, J. Physique **41**, 981 (1980).

72. F. Firszt and H. L. Oczkowski, phys. stat. sol. (a) **111**, K113 (1989).

73. Y. Shirakawa and H. Kukimoto, Solid State Comm. **34**, 359 (1980).

74. D. Verity, F. J. Bryant, C. G. Scott and D. Shaw, J. Cryst. Growth **59**, 234 (1982).

75. T. Miyajima, K. Akimoto and Y. Mori, J. Appl. Phys. **67**, 1389 (1990).

APPENDICES

APPENDIX A

METHOD OF RUNGE-KUTTA-FEHLBERG

In order to solve the initial value problem

$$x' = f(t, x) \tag{111}$$
$$x(a) = s,$$

one often expands x in a Taylor series. This method, of course, requires differentiating $f(t, x)$ in order to determine the higher order derivatives of x. In many instances this approach becomes extremely complicated and tedious.

Carl Runge and Wilhelm Kutta designed the famous Runge–Kutta method to imitate the Taylor series method with one important distinction; evaluation of higher order derivatives is not necessary. This method provides a powerful technique for solving systems of non-linear coupled differential equations such as those presented in chapter II (see equations (74) and (75)).

The Runge–Kutta method of order 4 is presented here without derivation. A complete development for the second order Runge–Kutta method is presented by Chaney and Kincaid[38]. For higher than second order, they present equations without derivation. The fourth order Runge–Kutta solution to the initial value problem is given as follows

$$x(t + h) = x(t) + \frac{1}{6}(F_1 + 2F_2 + 2F_3 + F_4) \tag{112}$$

where

$$F_1 = h\, f(t, x)$$

$$F_2 = h\,f\left(t + \frac{h}{2}, x + \frac{1}{2}F_1\right)$$
$$F_3 = h\,f\left(t + \frac{h}{2}, x + \frac{1}{2}F_2\right)$$
$$F_4 = h\,f(t + h, x + F_3)$$

and h is the step size for the independent variable x. The above expansion agrees with the Taylor series expansion up to terms of order h^4. Therefore, truncation error is on the order of h^5 but the precise value of this error is unknown.

The fourth order algorithm was improved by E. Fehlberg to include an estimate of the truncation error. Felhberg's fourth order equation is

$$x(t + h) = x(t) + \frac{25}{216}F_1 + \frac{1408}{2565}F_3 + \frac{2197}{4104}F_4 - \frac{1}{5}F_5 \tag{113}$$

where

$$F_1 = h\,f(t, x)$$
$$F_2 = h\,f\left(t + \frac{1}{4}h, x + \frac{1}{4}F_1\right)$$
$$F_3 = h\,f\left(t + \frac{3}{8}h, x + \frac{3}{32}F_1 + \frac{9}{32}F_2\right)$$
$$F_4 = h\,f\left(t + \frac{12}{13}h, x + \frac{1932}{2197}F_1 - \frac{7200}{2197}F_2 + \frac{7296}{2197}F_3\right)$$
$$F_5 = h\,f\left(t + h, x + \frac{439}{216}F_1 - 8F_2 + \frac{3680}{513}F_3 - \frac{845}{4104}F_4\right)$$

By adding the additional function evaluation

$$F_6 = h\,f\left(t + \frac{1}{2}h, x - \frac{8}{27}F_1 + 2F_2 - \frac{3544}{2565}F_3 + \frac{1859}{4104}F_4 - \frac{11}{40}F_5\right) \tag{114}$$

a fifth order Runge–Kutta method is obtained

$$x(t + h) = x(t) + \frac{16}{135}F_1 + \frac{6656}{12825}F_3 + \frac{28561}{56430}F_4 - \frac{9}{50}F_5 + \frac{2}{55}F_6 \tag{115}$$

By evaluating both equations (113) and (115) and calculating the difference, an error estimate is obtained.

These equations are used to form an adaptive Runge–Kutta–Fehlberg algorithm. If the error exceeds a predetermined maximum, then the step size h is

reduced in order to improve accuracy. If, on the other hand, the error is less than some minimum required error, then the value of h may be increased in order to reduce calculation time.

Equations (113) through (115) were used to generate the Runge–Kutta data presented in chapter II. The differential equations (74) and (75) must be written in the form

$$\frac{dn}{dT} = f^n(T, n, n_c)$$
$$\frac{dn_c}{dT} = f^{n_c}(T, n, n_c).$$

where f^n and f^{n_c} denote the right hand side of equations (74) and (75), respectively. By defining the functions F_1^n through F_6^n and $F_1^{n_c}$ through $F_6^{n_c}$ as above, the Runge–Kutta–Fehlberg algorithm is implemented as follows

$$F_1^n = \delta T\, f^n(T, n, n_c)$$
$$F_1^{n_c} = \delta T\, f^{n_c}(T, n, n_c)$$
$$F_2^n = \delta T\, f^n\left(T + \frac{1}{4}\delta T, n + \frac{1}{4}F_1^n, n_c + \frac{1}{4}F_1^{n_c}\right)$$
$$F_2^{n_c} = \delta T\, f^{n_c}\left(T + \frac{1}{4}\delta T, n + \frac{1}{4}F_1^n, n_c + \frac{1}{4}F_1^{n_c}\right)$$
$$\vdots$$
$$n(T + \delta T) = n(T) + \frac{25}{216}F_1^n + \frac{1408}{2565}F_3^n + \frac{2197}{4104}F_4^n - \frac{1}{5}F_5^n$$
$$n_2(T + \delta T) = n_2(T) + \frac{16}{135}F_1^n + \frac{6656}{12825}F_3^n + \frac{28561}{56430}F_4^n - \frac{9}{50}F_5^n + \frac{2}{55}F_6^n$$
$$Error_n = |n_2 - n|$$
$$n_c(T + \delta T) = \cdots$$
$$\vdots$$
$$T = T + \delta T$$

At the end of these evaluations we have the values of n and n_c at $T + \delta T$. By repeating these steps many times it is possible to evaluate n and n_c over a wide temperature range. The variable $Error_n$ has a counterpart $Error_{n_c}$ which is calculated in a similar manner. The larger of these two numbers determines the

maximum error for the current iteration, if this number is too large then all values are reset to their values at the beginning of the iteration, δT is divided by two and the process is repeated. If the largest error is less than some minimum error level, then the value of δT is doubled for the next iteration.

In chapter II, the Runge–Kutta solutions were referred to as *exact* numerical solutions. It may seem that the word *exact* implies a bit too much confidence but since all of the data sets were obtained with a maximum allowed error of $10^{-6}\%$, for all practical purposes they *are* exact.

APPENDIX B

CURVE FITTING

When attempting to describe real data with a mathematical model, it is often convenient to perform curve fitting. Curve fitting involves minimizing the function

$$\chi^2 = \sum_{i=1}^{N} [y_i - f(x_i, \vec{a})]^2 \tag{116}$$

where x_i, y_i describes the data to be fitted, N is the number of data points, f is the mathematical model and $\vec{a}$ is an n dimensional vector in which each component is an adjustable fitting parameter. Thus, the adjustable parameters define an n–dimensional χ^2 space. For the specific case of n=2, χ^2 is simply a surface which contains peaks and valleys. Curve fitting is the systematic process of searching for the deepest valley.

This minimum value obtained for χ^2 may have two very undesirable properties. First, it may simply be a local minimum in which case we have failed to find the best fit. Second, the fitting program may have wandered into a region of parameter space in which some parameters have taken on physically meaningless values such as negative capture cross sections. The latter problem is easily overcome by restricting the parameter space which is accessible to the fitting program. The first problem, however, is not so simple; several local minima may occur in regions of physically reasonable parameter space. We can often locate several local minima by repeating the fit to a particular data set several times, each time using a different set of starting values for the fitting parameters. If the program locates the same minimum each time, then we take this minimum as the best fit. If, however, several local minima are found, one may simply interpret the range of the various parameters as a range of uncertainty.

The curve fitting results for TSC and TL data presented in this thesis were obtained by implementing the Randall Wilkins expression through PeakFit^{TM} (a product of Jandel software).

There are some points of concern when fitting data to the Randall Wilkins equation (Eqn. (15)). First, it was necessary to scale the fitting parameters so that their values were all within a few orders of magnitude of one another. The reason for this requirement is to prevent the equation from becoming over or under sensitive to any one parameter. For example, the activation energy E is normally a number between 0 and 1 and the coefficient for the capture cross section, C, is commonly on the order of 10^{-15}. Obviously, these two numbers cannot be varied by equal amounts. PeakFit^{TM} attempts to account for the orders of magnitude difference but it does not do a good job; it often varies small numbers too quickly. This problem is easily corrected by introducing the fitting parameter α and expressing C either as $C_0 \times 10^{\alpha}$ or as $\alpha \times 10^{-15}$. Both of these expressions have been used and it was found that the best results were obtained with the latter. Another parameter which must be dealt with is the scaling constant n_0. For data such as Runge–Kutta output, peak heights of 10^8 are typical and this results in large values for n_0 (typically on the order of 10^9). We have found that by normalizing the data, prior to fitting, we restrict n_0 to a range from about 50 to a few hundred. Since the fitting parameter b (temperature dependence of S; see Eqns. (6) and (66)) is already restricted to the range of 0 to 4, we need not be concerned with it.

With the above points in mind, the fitting equation used in PeakFit^{TM} was written as

$$
\begin{aligned}
I \;=\; & \#A \cdot A_1 \cdot \#B \cdot X^{2-\#D} \cdot \exp\left(\frac{-\#A2}{k \cdot X}\right) \times \\
& \exp\left\{\frac{-A_1 \cdot \#B \cdot k \cdot X^{4-\#D}}{\beta/60 \cdot \#C} \times \right. \\
& \left. \left(1 + \frac{(\#D-4) \cdot k \cdot X}{\#C}\right) \exp\left(\frac{-\#C}{k \cdot X}\right)\right\}
\end{aligned}
\tag{117}
$$

where the fit parameters $\#A, \#C$ and $\#D$ represent n_0, E and b, respectively. The parameter $\#B$ may be used to represent either B or C depending on the value of the scaling constant A_1. According to equation (6), the parameters B and C are related according to

$$B = 3.256564 \times 10^{25} \frac{m}{m^*} C \tag{118}$$

where the scaling constant has the units $(\text{Kelvin}^2\ \text{m}^2\ \text{sec})^{-1}$.

If we first consider the case of parameterization in B, we proceed as follows. If it is assumed that B is on the order of 10^9, then A_1 should be set equal to 10^9. This will force the parameter $\#B$ to be on the order of 1. In order to calculate B, simply take the product $\#B \times 10^9$. If, on the other hand, we wish to parameterize in C, assuming C is on the order of 10^{-15}, then set $A_1 = 3.256564 \times 10^{10} \frac{m}{m^*}$. This will again force $\#B$ to be on the order of 1 and we calculate C as $\#B \times 10^{-15}$.

VITA

BRIAN G. MARKEY

Candidate for the Degree of

Doctor of Philosophy

Thesis: DEEP LEVEL CHARACTERIZATION OF SEEDED PHYSICAL VAPOR TRANSPORT ZINC SELENIDE

Major Field: Physics

Biographical:

Personal Data: Born in Glen Cove, New York, March 14, 1964, the son of William and Florence Markey.
Married Kim Williams, June 8, 1985. Two children.

Education: Received Bachelor of Science Degree in Physics and Computer Science from Southwest Missouri State University, Springfield, Missouri 1988; completed requirements for the Doctor of Philosophy Degree at Oklahoma State University, Stillwater, Oklahoma in July, 1993.